SAND2017-2498R

FY16 Status Report: SNF Interim Storage Canister Corrosion and Surface Environment Investigations

Spent Fuel and Waste Disposition

Prepared for
U.S. Department of Energy
Spent Fuel and Waste Science and Technology
Charles Bryan and David Enos
Sandia National Laboratories
March 2, 2017
FCRD-UFD-2016-000429
SAND2017-xxxx-xx

Sandia National Laboratories is a multi-mission laboratory managed and operated by Sandia Corporation, a wholly owned subsidiary of Lockheed Martin Corporation, for the U.S. Department of Energy's National Nuclear Security Administration under contract DE-AC04-94AL85000.

SUMMARY

This progress report describes work done in FY15 at Sandia National Laboratories (SNL) to assess the localized corrosion performance of container/cask materials used in the interim storage of spent nuclear fuel (SNF). Of particular concern is stress corrosion cracking (SCC), by which a through-wall crack could potentially form in a canister outer wall over time intervals that are shorter than possible dry storage times. In order for SCC to occur, three criteria must be met. A corrosive environment must be present on the canister surface, the metal must susceptible to SCC, and sufficient tensile stress to support SCC must be present through the entire thickness of the canister wall. SNL is currently evaluating the potential for each of these criteria to be met.

The potential for high residual tensile stresses in interim storage canisters, and canister material properties, including material susceptibility to SCC, are being evaluated by analysis of a full-diameter cylindrical mockup of a SNF storage canister, fabricated by a canister supplier using the same materials and manufacturing procedures as real in-service canisters. Residual stresses due to cold working and welding processes have been measured in welds and adjacent heat-affected zones for longitudinal and circumferential welds, at weld intersections and simulated weld repair regions, and at base metal locations far from any welds. Measurements have shown that base metal stress patterns are dominated by a bending moment introduced during the bending of the plate into a cylinder, with the outer half of the shell dominated by tensile stresses, and the inner half, by compressive stresses. Through-wall tensile stresses capable of supporting the development of canister-penetrating SCC cracks occur through at both the circumferential and longitudinal welds. The highest tensile stresses parallel the weld, being axial stresses near longitudinal welds, and hoop stresses near circumferential welds. However, moderately high tensile stresses also occur perpendicular to the welds. Tensile stresses were especially high near the simulated weld repairs. Material characterization studies of the weld regions have begun, and will include will include 3-dimensional characterization of the degree of sensitization and textural changes near weld zones. Ultimately, this information will be used to identify relevant sample properties and stress states for corrosion testing.

To assess the chemical environment that might form on SNF interim storage canisters by deliquescence of deposited salts, SNL has carried out experimental work evaluating the stability of salts and deliquesced brines on hot canister surfaces. Thermally-driven exchange reactions with the atmosphere may work to make salt assemblages or brines less corrosive, reducing the risk of SCC. Moreover, the work can help define realistic salt assemblages and brine compositions for experimental studies. Studies in FY15 showed that ammonium chloride and ammonium nitrate decompose rapidly in the solid state, and cannot accumulate on a hot package. Brines formed by deliquescence of these salts are also not stable, rapidly degassing ammonia and an acid gas (HCl, HNO_3). However, ammonium sulfate, a common salt in continental aerosols, and sodium chloride which could be deposited on canisters from cooling tower emissions, do not decompose in the solid state, and could accumulate on canister surfaces. New experiments in FY16 evaluated the stability of this mixed salt assemblage, and confirmed that once these salts deliquesce, ammonia and HCl rapidly degas and sodium sulfate precipitates. It is likely that deliquesced brines containing ammonium and either nitrate or chloride cannot persist on canister surfaces at even slightly elevated temperatures; such brines will degas ammonia and an acid gas until one or the other is consumed. Therefore, formation of persistent chloride brines on canister surfaces at inland sites requires that chloride and nitrate be deposited at a greater rate than ammonium, generally the most abundant cation in inland atmospheric aerosols. These data provide arguments for lengthening canister inspection intervals at inland sites, where chloride deposition may be overwhelmed by deposition of ammonium minerals.

SNL has also continued to work with the Electric Power Research Institute and industry in characterizing dust on canisters at Independent Spent Fuel Storage installations, evaluating dust samples from surfaces within a canister storage system at the Maine Yankee site. The canister contained non-heat-generating

Greater-Than-Class-C waste. Samples were taken from the shield plug on top of the canister, from the canister side, and from a shelf at the bottom of the annulus between the canister and the overpack. Sample analysis at Sandia showed that the terrestrially derived mineral fragments, but soluble salts were also present and sulfate-rich on the shield plug, and nitrate-rich at the other two locations; However, significant chloride was also present at all locations. The salts appear to represent a mixture of sea-salts (probably partially converted to nitrates and sulfates by particle-gas conversion reactions) and continental salt aerosols. Ammonium, a common component in continental aerosols, was not observed and may have been lost by degassing from the canister surface or after collection during sample storage and transportation. However, the relevance of the analyses to storage systems at the site that contain SNF may be limited, because a heat-generating canister will result in greater airflow through the overpack, affecting dust deposition rates and possibly salt compositions.

Finally, SNL provided support to the High Burnup Demonstration Project, evaluating corrosion residues that were found in the canister when it was opened for inspection prior to use, and plastic-wrapped wooden cribbing, placed in the cask 11 years earlier, was removed. The residues consisted largely of amorphous aluminum hydroxide, but a brown organic-rich material was also present. The residue at one of the two sites sampled consisted largely of a spongy mass of fungal hyphae, and insect fragments were present at both sites; insect carcasses were also observed by borescope at the bottom of the canister. It is clear that the cribbing contained living insects and fungi when it was placed in the cask. Chemical analyses indicated that the residue contained many trace elements, mostly present in amounts consistent with their abundance in Al-6061, the aluminum comprising the rails. Other elements could be sourced to fungal degradation of the wood. The presence of the organic material, the fungus, and the insect fragments, indicates that the polypropylene wrapping on the cribbing was damaged, allowing fluids from the wood, or the wood itself, to contact the aluminum metal, resulting in corrosion. The corrosion could have been due to a combination of crevice effects, organic acids leached from the wood, or fungal growth. Evidence suggests that fungal growth played an important role both through direct and indirect processes. Fungal activity produces powerful metal complexants that have been shown to promote aluminum corrosion, but also is the dominant mechanism of wood decay, increasing organic acid release. Regardless of the mechanism, it is clear that corrosion of the aluminum metal was due to contact with the wooden cribbing. Areas not contacted by the cribbing or fluids generated by it are unlikely to be corroded, and once the corroded sites and the cask interior have been thoroughly cleaned (the fluid may have dripped deeper into the cask), further corrosion over the course of the high-burnup demonstration test is unlikely.

CONTENTS

FIGURES

TABLES

ACRONYMS

ASME	American Society of Mechanical Engineers
ASTM	ASTM International
BSE	backscattered electron [imaging]
CHD	center-hole drilling
CISCC	chloride induced stress corrosion cracking
DOE	Department of Energy
DHD	deep-hole drilling
EDM	electric discharge machining
EDS	energy dispersive [X-ray] spectroscopy
EPR	electrochemical reactivation
EPRI	Electric Power Research Institute
FCRD	Fuel Cycle Research and Development
FME	foreign material exclusion [cover]
FTIR	Fourier Transform Infrared [Spectroscopy]
FZ	fusion zone
HAZ	heat-affected zone
HBU	high-burnup [demonstration project]
IC	ion chromatography
ICHD	incremental center-hole drilling
ICP-MS	inductively coupled plasma-mass spectrometry
iDHD	incremental deep-hole drilling
ISFSI	independent spent fuel storage installation
GTCC	greater than class C
NDE	non-destructive evaluation
NEUP	Nuclear Energy University Programs
NRC	Nuclear Regulatory Commission
NWTRB	Nuclear Waste Technical Review Board
QA	quality assurance
SAW	submerged arc welding
SCC	stress corrosion cracking
SE	secondary electron [imaging]
SEM	scanning electron microscope
SNF	spent nuclear fuel

SNL	Sandia National Laboratories
SS	stainless steel
WRS	weld residual stress
UFD	Used Fuel Disposition
XRD	X-ray diffraction
XRF	X-ray fluorescence

SPENT FUEL AND WASTE DISPOSITION PROGRAM FY16 STATUS REPORT: SNF INTERIM STORAGE CANISTER CORROSION AND SURFACE ENVIRONMENT INVESTIGATION

1. INTRODUCTION

This progress report describes work being done at Sandia National Laboratories (SNL) to assess the localized corrosion performance of container/cask materials used in the interim storage of spent nuclear fuel (SNF). Of particular concern is stress corrosion cracking (SCC), a mechanism by which a through-wall crack could potentially form in a canister over time intervals that are shorter than possible dry storage times. Developing an understanding of stress corrosion cracking (SCC) of interim storage containers has been indicated as a high priority data gap by the Department of Energy (DOE) (Hanson et al., 2012), the Electric Power Research Institute (EPRI, 2011), the Nuclear Waste Technical Review Board (NWTRB, 2010), and the Nuclear Regulatory Commission (NRC, 2012a; NRC, 2012b).

In order for SCC to occur, three criteria must be met. A corrosive environment must be present on the canister surface, the metal must be susceptible to SCC, and sufficient tensile stress to support SCC initiation and growth must be present (**Figure 1**). Uncertainties exist in terms of the environmental conditions that prevail on the surface of the storage containers, the stress state within the container walls associated both with weldments as well as within the base metal itself, and the electrochemical properties of the storage containers themselves. SNL is currently evaluating each of these criteria.

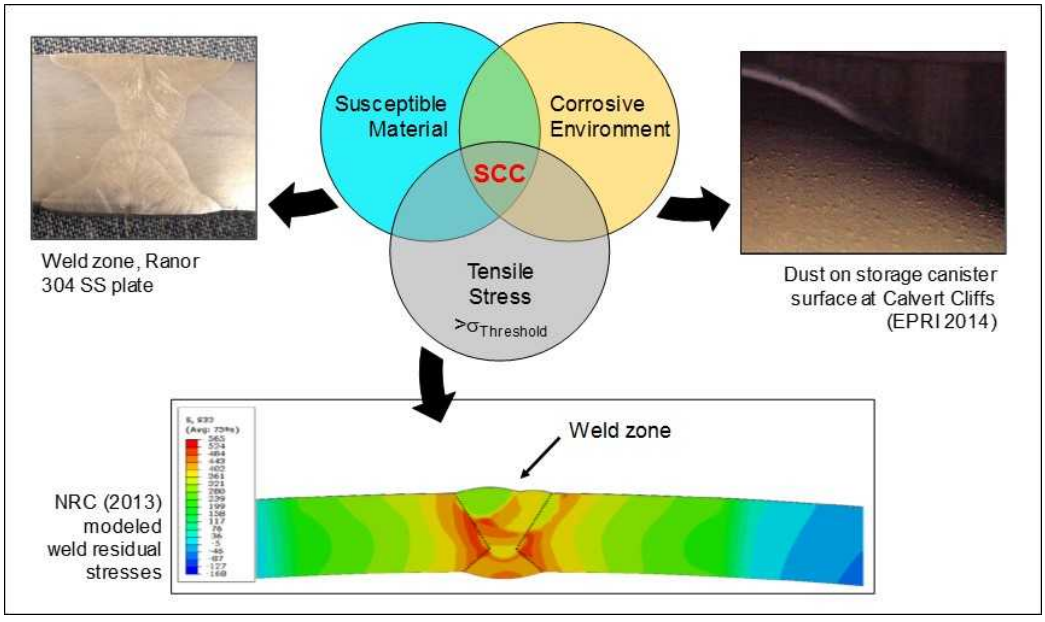

Figure 1: Criteria for the Occurrence of Stress Corrosion Cracking.

The potential for high residual tensile stresses in interim storage canisters, and canister material properties, including material susceptibility to SCC, is being evaluated by analysis of a full-diameter cylindrical mockup of a canister, fabricated by a canister supplier using the same materials and manufacturing procedures as real in-service canisters. Residual stress measurements have been completed and are summarized in a recently completed report, *Final Report: Characterization of*

Canister Mockup Weld Residual Stresses (FCRD-UFD-2016-000064; Enos and Bryan, 2016a). The results of that analysis are summarized here in Section 2.

With respect to the canister environment, studies in FY16 evaluated the stability of ammonium- and chloride-containing mixed salt assemblages on hot canister surfaces, where thermally-driven exchange reactions with the atmosphere may work to make salt assemblages or brines less corrosive. Moreover, the work can help define realistic salt assemblages and brine compositions for experimental studies. These experiments are summarized in Section 3. Also, SNL has continued to work with the Electric Power Research Institute (EPRI) and industry to assess the environment on canister surfaces, characterizing dust collected from surfaces within an in-service interim storage system at the Maine Yankee Independent Spent Fuel Storage Installation (ISFSI) as part of an EPRI-led robotics testing campaign. This work was published in a SNL SAND report, *Analysis of Dust Samples Collected from an In-Service Interim Storage System at the Maine Yankee Nuclear Site* (SAND2016-10266; Bryan and Enos, 2016) and is summarized in Section 4.

Finally, SNL provided support to the High Burnup Demonstration Project, evaluating corrosion residues that were found in the canister when it was opened for inspection and plastic-wrapped wooden cribbing, placed in the cask 11 years earlier, was removed. This evaluation was performed using funding from the High Burnup Demonstration Project, and is presented here because that project has no formal milestone for the year. The results have been published in *Analysis of Corrosion Residues Collected from the Aluminum Basket Rails of the High-Burnup Demonstration Cask* (SAND2017-2306; Bryan, 2017) and are summarized in Section 5.

2. CHARACTERIZATION OF WELD RESIDUAL STRESSES IN AN INTERIM STORAGE CANISTER MOCKUP

David Enos and Charles Bryan, Sandia National Laboratories

Little is known about the stress state within the container walls associated both with weldments and within the base metal, and in the textural, microstructural, and electrochemical properties of interim storage canister weld regions. In order to meet the need for additional data on the canister material properties, the UFD campaign procured a full-diameter cylindrical mockup of a dual certified 304/304L stainless steel (SS) storage canister produced using the same manufacturing procedures as fielded SNF fuel interim storage canisters. The weld and base metal zones on this mockup will be characterized to determine metal properties and susceptibility to SCC. To date, evaluation of weld and base metal residual stresses has been completed, and a final report on that work has been issued, *Final Report: Characterization of Canister Mockup Weld Residual Stresses* (FCRD-UFD-2016-000064; Enos and Bryan, 2016a). The report documents the mockup specifications and manufacturing processes; the initial cutting of the mockup into three cylindrical pieces for testing and the measured strain changes that occurred during the cutting process; and the weld residual stress characterization results. A summary of the results is provided here; for detailed information, the reader is directed to Enos and Bryan (2016a). T

2.1 Mockup design

The material properties in interim storage canister base metal and weld zones are strongly controlled by the materials and manufacturing processes used to make the canister. Therefore, the mockup had to be made using the same materials and fabrication methods as a real canister. To ensure consistency with in-service canisters, the mockup was built by Ranor, Inc, a company that in the past has been contracted to build stainless steel storage canisters for TransNuclear (now Areva-TN). With the permission of Areva-TN, Ranor built the mockup using identical materials and procedures as were used to build the original TransNuclear horizontal storage canisters.

The mockup is based on the TransNuclear NUHOMS 24P design. The mockup, pictured schematically in Figure 2 below, consists of three cylindrical shells of dual-certified 304/304L SS, each 48 inches long and 67.2 inches in diameter, and having a wall thickness of 5/8 inch. Each shell was formed by cold forming a plate into a cylinder, then making a single longitudinal weld to form the cylinder. The three cylinders were then welded together to form a single large cylinder 12 feet in length with two circumferential welds. All of the welds were formed via the submerged-arc welding (SAW) process and were multi-pass. The edge preparation used for each weld was a 30-degree bevel, with a quarter inch land, as illustrated in Figure 3 below. Each inner-diameter weld consisted of three passes, and with one exception, each outer-diameter weld was made with four passes (the exception had 5). The inner diameter was welded first, followed by the outer diameter. Once the inner diameter weld was made, the edge preparation for the outer diameter weld was made by arc-gouging along the parting line between the two plates being welded together. The depth of the gouge was adjusted such that the parting line was no longer visible, ensuring there would be no voids/gaps. Upon completion of the welding, the surface of each weld was smoothed, following the procedures developed by Ranor. This grinding, along with handling marks, etc. will likely have a significant impact on the near-surface stresses in the weld and nearby regions.

The compositions of the 304/304L SS plates and the 308L SS weld filler material, and the parameters for each weld pass, including the current, voltage, travel speed, heat input, and interpass temperatures are documented in Enos and Bryan (2016a).

During fabrication of the mockup, all of the welds were subjected to a full radiographic inspection, and no indications requiring repair were found. However, because of the potentially important effect of weld repairs on weld residual stresses and material properties, one region on each circumferential weld was subjected to a repair procedure representative of what would typically be done for a SAW weld on the

outer diameter. In these locations, an artificial defect corresponding to a 1/8" diameter hole was drilled partially into the outer diameter, simulating a small defect such as porosity or an entrained slag particle (illustrated schematically in Figure 4). The "defect" was then removed by machining out a larger region via a ¼" drill, after which the edges of the drilled out region were ground to a bevel, such that it could be re-welded. The repair was welded using the gas tungsten arc welding technique. Characterization of these sites will allow determination of weld residual stresses and degrees of sensitization typical of weld repair regions.

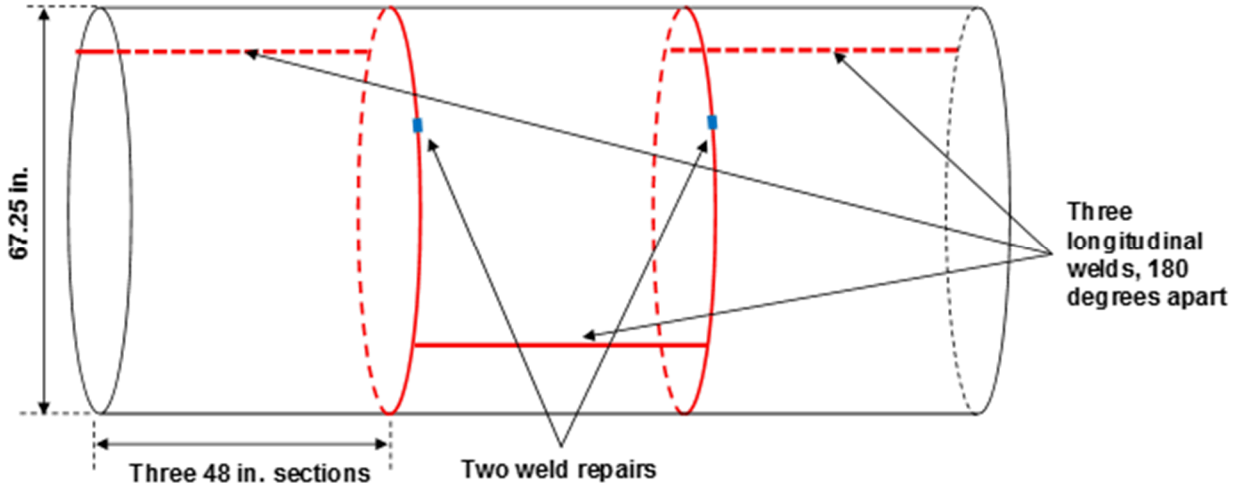

Figure 2: Schematic representation of the full-diameter cylindrical canister mockup.

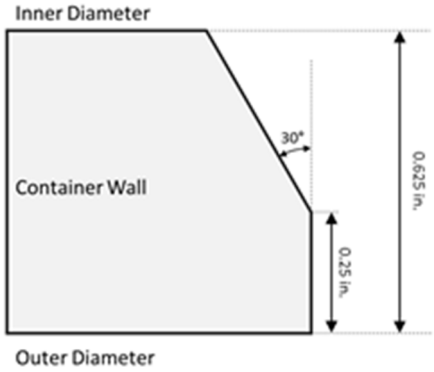

Figure 3: Edge preparation prior to welding used for both circumferential and longitudinal welds.

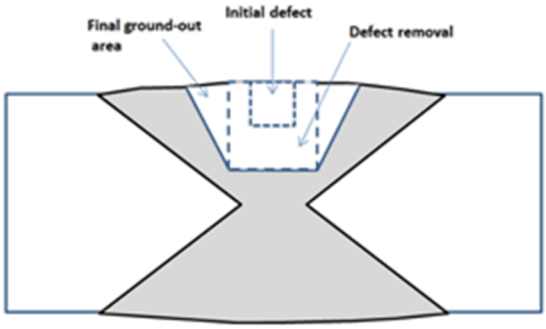

Figure 4: Schematic representation of simulated defect placed in each of the circumferential welds.

2.2 RESIDUAL STRESS CHARACTERIZATION METHODS USED

In addition to a susceptible material and a sufficiently aggressive environment, the nucleation and growth of a stress corrosion crack requires the presence of a sufficiently large stress. In the case of interim storage containers, the stress existing within the structure will predominantly be residual stresses resulting from the forming of the metal plates into a cylinder and the subsequent welding and associated solidification shrinkage of the fusion zone (FZ) upon cooling. The latter are likely to be the largest in magnitude, and are the result of the constraint placed by the structure of the container (and any additional fixtures used during fabrication) on the weld as it solidifies. Several methods are available for residual stress measurement, as summarized in NUREG-2162 (Benson et al., 2014). The techniques vary in terms of their sensitivity and depth of penetration into the substrate metal. The most appropriate technique for assessing the mockup storage container is one capable of measuring the stresses through the thickness of the container wall. Furthermore, to determine the stress state accurately, it must be measured within the intact cylinder, prior to cutting or sectioning of the container into smaller samples, which would release the cylindrical constraints on the sample.

Five techniques were used in this study. These include a combination of deep-hole drilling (DHD) and incremental center-hole drilling (ICHD), the contour method, x-ray diffraction (XRD), and ultrasonic stress measurement. These methods are described in brief here; see Enos and Bryan (2016a) for more details.

2.2.1 Deep-Hole Drilling and Incremental Center-Hole Drilling

The DHD method allows through-thickness stresses to be measured in an intact metal structure, without the need for sectioning or cutting. In this technique, bushings made of a similar material are attached to either side of the sample. Next, a small-diameter hole is precisely drilled via a gun drill through the material, starting at one bushing, passing through the material of interest, and then exiting through the back bushing. An air gauge is then used to precisely characterize the diameter of the hole along its length. Next, electric discharge machining (EDM) is used to cut an overcore around the gun-drilled hole. As the core is cut, the constraint placed on the metal immediately adjacent to the central hole is relaxed, resulting in local lateral displacement of the material. The inner diameter of the hole is then re-characterized and the resulting change in cross-sectional shape due to the loss of constraint around the hole is recorded. From these strains, the original residual stress state within the material as a function of depth can be calculated.

The calculations used for standard DHD are based upon the assumption that the stress relaxation leading to the measured displacements is entirely elastic in nature. When large stresses are present, this is not true, and plastic deformation of the material can result, hindering the ability of the technique to resolve stress. To compensate for this, a modified method called incremental deep-hole-drilling (iDHD) is used (Mahmoudi et al., 2009; Mahmoudi et al., 2011). In the modified technique, the EDM core is cut in steps.

After each step, the inner diameter of the hole is characterized via the air probe. By measuring the deformation of the inner diameter of the hole at the depth of the core cut, the effect of plasticity can be addressed. The resulting residual stress distribution is lower in resolution than the traditional measurement because it is measured in discrete steps as the hole is drilled, but is able to resolve large residual stresses.

As the DHD technique is inaccurate near the outer metal surface, center-hole drilling (CHD) or incremental center-hole drilling (ICHD) was used to measure the stresses in the first 0.5mm of material. In this technique, a strain rosette was placed on the surface to be analyzed, and then a hole is precisely drilled through the center of the pattern. As the hole is drilled, the stress relaxes in the region near the hole, the resulting strains from which are monitored by the strain gauges described above. These strains are then converted to the effective stresses near the surface of the metal.

2.2.2 Contour Method

The contour method analyzes a cross-sectional surface of the metal, which requires cutting a section of the weld from the mockup. While the use of surface strain gauges can help measure the stress relaxation associated with cutting a section from the mockup, the cutting process introduces an additional level of uncertainty to the residual stress measurement.

As with hole drilling techniques, the contour method involves the removal of constraint from the system, and the measurement of the resulting relaxation displacements. The contour method is similar to the deep hole drilling method in that displacements due to elastic stress relaxation are converted to a pre-existing residual stress. It is critical that any stress relaxation that takes place as the sample is prepared are accounted for, so prior to cutting the mockup, surface-mount strain gauges were placed on the surface in the region where the contour measurement will be made. The mockup was then cut, and the segment of the weld to be evaluated was removed from the overall structure. A sacrificial bushing was adhered onto both sides of the region being contoured, to keep the section being cut uniform in thickness. Next, the sample was rigidly held within a wire-EDM (electrical-discharge machining) machine, and cut into two sections in a single pass with a 250μm diameter brass wire on "skim cut" settings. The cut creates two stress-free surfaces and hence relaxes the out-of-plane residual stresses in the region of interest. A coordinate measuring machine was then used to precisely measure the deviations of the cut surface resulting from the stress relaxation associated with making the cut. Mathematically, the deviations (i.e., strains) were then converted into the residual stress state that existed prior to being cut. The calculated stresses represent one stress direction – perpendicular to the cut surface.

The contour method is destructive in nature and requires that the region being measured be extracted from the mockup container. The use of external strain gauges when extracting the sample enables the stress relaxation not captured by the contour measurement itself to be added back in, such that the initial stress state can be accurately estimated. By combining this method with iDHD prior to cutting, changes in stress due to cutting can be even more accurately estimated and corrected for, resulting in a high-resolution map of the stress distribution across the entire cut surface.

2.2.3 X-Ray Diffraction

Diffraction-based measurements allow the stress state to be evaluated with little or no cutting of the material being evaluated. Due to the low penetration depth of x-rays into the metal being evaluated, only the very near surface stresses can be measured (i.e., tens of microns into the sample). An x-ray source is directed towards the surface being analyzed. The x-rays are then diffracted by the atomic structure of the stainless steel. Using Bragg's law, the diffracted x-rays are used to measure the lattice spacing of the stressed sample. Through the use of differential analysis techniques, the need to obtain data from an unstressed control (as required for neutron diffraction) is not needed for x-ray diffraction. Based upon the distortion of the stressed sample (in terms of the change in lattice spacing relative to unstressed material), the strain field within the structure can be determined. These strains are then converted to normal stresses through the use of Hooke's law in two dimensions.

2.2.4 Ultrasonic Measurements

The UT residual stress measurement technique exploits the acousto-elastic property of materials, in which the speed of sound through a material changes with stress. The speed of a longitudinal ultrasound wave through a material has been determined to be sensitive to stress changes in the direction of propagation of the wave. In essence, the speed of the longitudinal wave decreases in regions where a tensile stress exists, and increases in regions where the stress is compressive in nature.

At each measurement point, the sound velocity within the stainless steel wall was evaluated in a volume with a depth of approximately 2.8mm, approximately 16mm long and 6mm wide. The sound velocity was then compared to the velocity in an unstressed sample of the material, and the local stress, average over the volume sampled, was then proportional to the difference in velocity relative to the unstressed material. Only the residual stresses in the hoop direction were measured via the UT system. Performing the test was accomplished by first placing an ultrasonic couplant over the measurement location (to allow coupling of the sound waves from the transducers located within an acrylic test fixture, and the stainless steel). The transit time between ultrasonic transducers positioned at each side of the gauge length was measured via an oscilloscope, the resulting velocities were then calculated and used to determine the average stress state at each measurement location. The measurement fixture was moved across each measurement location, allowing the variation in residual stress to be measured as a function of position.

2.3 RESULTS OF THE RESIDUAL STRESS CHARACTERIZATION STUDY

As noted previously, the mockup is intended to be used in several different studies; only half of the cylinder was used for residual stress characterization. As described in Enos and Bryan (2016a), stress gauges were used to monitor changes in the stresses as the cylinder was cut, and were determined to be negligible.

Measurements were made in five different regions, as illustrated schematically in **Figure 5**. These regions include representative circumferential and longitudinal weld sections and a simulated weld repair region. Finally, the stress state of the base metal was measured. The following measurements were done.

Welds:

a. iDHD measurement in the center of the FZ for both a longitudinal and circumferential weld
b. iDHD measurement in the heat-affected zone (HAZ) (immediately adjacent to FZ) for both a longitudinal and circumferential weld
c. Contour measurement perpendicular to weld centerline for both a longitudinal and circumferential weld
d. Contour measurement through the intersection of a circumferential and longitudinal weld (parallel to the centerline of the longitudinal weld)
e. XRD scan across a circumferential weld
f. XRD scan across the intersection of a longitudinal and circumferential weld
g. Ultrasonic scan across a longitudinal and a circumferential weld
h. Ultrasonic scan across the intersection of a longitudinal and circumferential weld

Weld repair:

i. iDHD measurement in the center of the weld FZ (center of the repair)
j. iDHD measurement in the HAZ on either side of the repair.

Base metal:

k. DHD measurement

l. X-ray diffraction scan at several locations to observe near-surface (tens of microns) stresses

The results of the residual stress measurements are presented in full in Enos and Bryan (2016a). Only a summary is provided here.

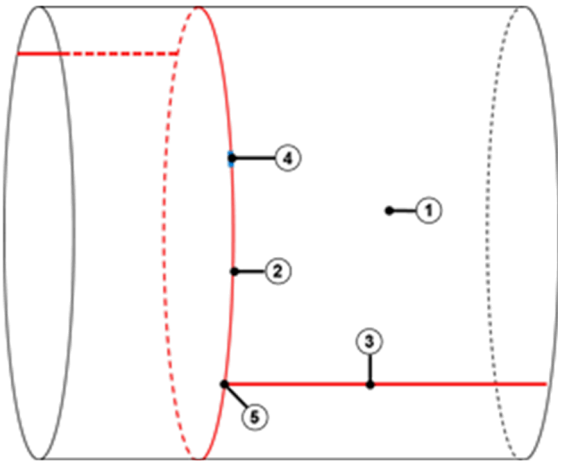

Figure 5: Regions for residual stress measurements. (1) Base metal, (2) Circumferential weld, (3) Longitudinal weld, (4) Weld repair region, and (5) Weld intersection.

2.3.1 Deep-Hole Drilling Measurements

2.3.1.1 Base Metal

DHD measurements (and the associated CHD/iCHD measurements) were performed within the base metal, in the FZ (weld centerline) and HAZ of each weld, and in the FZ and HAZ of the weld repair. Results of the base metal location, far from any weld, are shown in **Figure 6**. As a point of reference, the yield strength of annealed 304L SS is on the order of 170-200 MPa. In the figure, hoop stresses are parallel to the circumference of the container, and axial stresses are parallel to the long axis of the cylinder. Stresses very near the surface were measured using the ICHD technique (**Figure 6**a), and the residual stresses were tensile in nature. However, moving into the material, the axial strain remains small and tensile, but the hoop stress becomes compressive in nature. Due to measurement uncertainties that are not reflected in the error bars shown in the graph (Enos and Bryan, 2016a), the data in the figure is best interpreted in terms of the average magnitude and trends, and indicates low residual stresses in the first 0.5mm from the OD of the container.

The stress distribution through the container wall was determined by the DHD technique (iDHD was not necessary, because of the relatively low residual stresses in regions far from any welds), and results are shown in **Figure 6**b. The stress state at the outer wall is predominantly tensile in both the axial and hoop directions. Moving further into the wall, the hoop stress becomes increasingly tensile, then both the hoop and axial stresses decrease to approximately zero in the center of the wall. At greater distances from the outer surface, both the hoop and axial stresses then become large and compressive, but again become tensile as the inner wall is approached. This stress distribution reflects the forming of the flat plate into a cylinder. As the plate is bent, a bending moment is produced, with the outer diameter in tension and the while the inner diameter in compression. Plastic yielding during the forming process, followed by rebound effects once the forming stress is released, yield the stress distribution pictured in **Figure 6**. The stress profile through the canister shell illustrates why through-thickness SCC cracking is not anticipated at regions away from the weld. While crack initiation may take place at the surface, as the crack grows into the wall, the tensile stresses driving crack propagation will decrease, eventually becoming compressive in nature and arresting crack propagation.

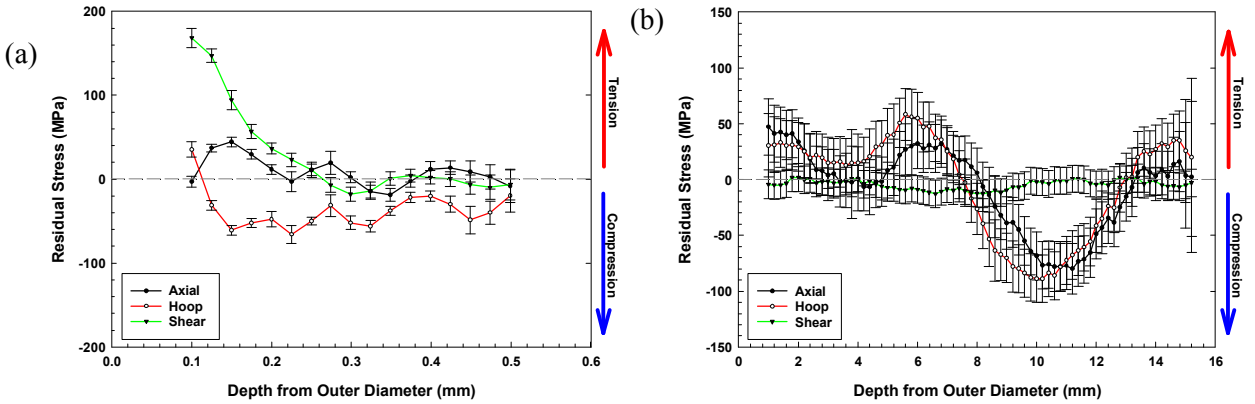

Figure 6: ICHD (a) and iDHD (b) for a base-metal region located far from any longitudinal or circumferential weldments. Note that stresses are tensile near the surfaces, then become compressive in the center of the wall due to the deformation process used to form the original plate material into a cylinder.

2.3.1.2 Circumferential Weld

As discussed above, the mock storage container has two different types of welds. The welds described in this section are circumferential welds (i.e., the welds that go around the circumference of the mockup container). Due to their orientation, these welds which were anticipated to have the highest residual stresses, due to the constraint placed upon them by the surrounding structure. The results of the ICHD and iDHD measurements are shown in Figure 7. Note that for this weld, the hoop stresses parallel the weld centerline, and axial stresses are perpendicular to the weld centerline. Both the axial and hoop stresses measured by ICHD in the near-surface region are large and tensile, decreasing in magnitude with depth. iDHD was used to measure the residual stresses through the thickness of the weld. Relative to the base metal, the residual hoop stresses in the weld root are significantly larger in magnitude, and are tensile in nature all of the way through the thickness of the container wall. As a result, if a crack were to initiate at the surface of the container, it would have the driving force necessary to support propagation through the container wall.

While the residual stresses were anticipated to be largest in the weld FZ, the regions surrounding the weld (the HAZ) are the regions where localized corrosion is most likely to initiate due to sensitization resulting from the thermal profile associated with the welding process. Characterization of the stresses in the HAZ was accomplished by performing ICHD and iDHD measurements approximately 4 mm from the weld toe (i.e., edge of the weld FZ). As with the other two locations, ICHD was used to measure the near-surface residual stresses, the results of which are shown in **Figure 8**. In the near-surface region, the hoop stress was large and tensile, increasing in magnitude with depth, while the axial stress was small and compressive, decreasing in magnitude and eventually becoming tensile with depth. iDHD was used to measure the residual stresses through the thickness of the HAZ. As with the center weld location, the residual stresses in the circumferential weld HAZ are tensile through the entire thickness of the shell, potentially capable of supporting through-thickness crack propagation.

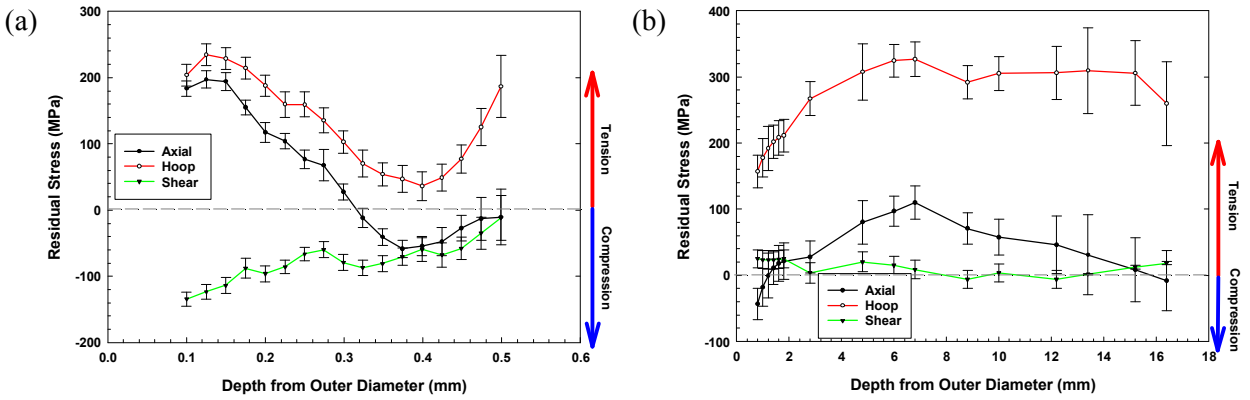

Figure 7: ICHD (a) and iDHD (b) data as a function of distance from the outer diameter of the container for the centerline of a circumferential weld. Note that stresses are tensile through the thickness of the plate, and are largest in magnitude in the hoop direction.

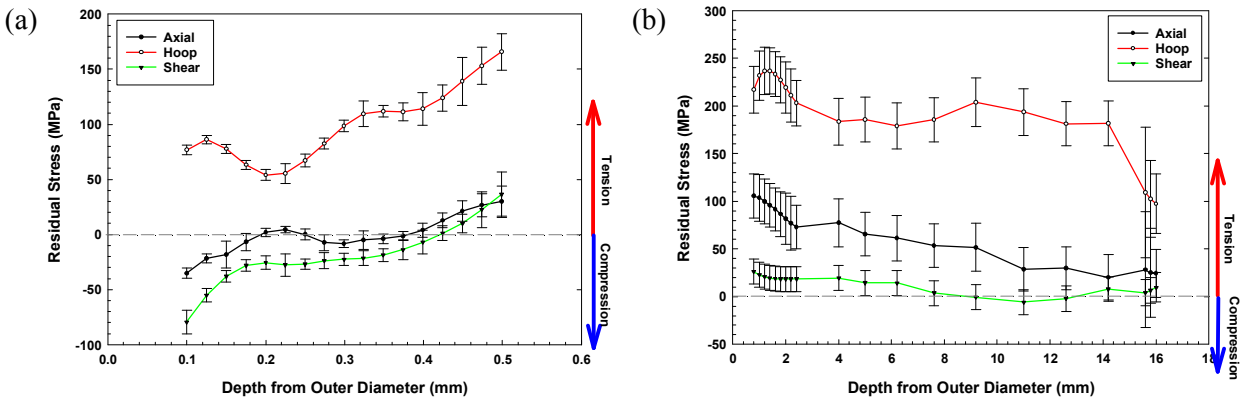

Figure 8: ICHD (a) and iDHD (b) data as a function of distance from the outer diameter of the container for the HAZ associated with a circumferential weld. Measurements were made approximately 4mm from the weld toe. Note that stresses are tensile through the thickness of the plate, and are largest in magnitude in the hoop direction.

2.3.1.3 Longitudinal Weld

The welds described in this section are longitudinal welds (i.e., the welds that are parallel to the long axis of the mockup container). ICHD and iDHD results are shown in **Figure 9**. For this weld, the axial stresses parallel the weld centerline, and hoop stresses are perpendicular to the weld centerline. The axial stress in the near surface region was large and tensile in nature, decreasing in magnitude with depth, while the hoop stress was large and compressive in nature near the surface, decreasing and eventually becoming tensile with depth. iDHD was used to measure the residual stresses through the thickness of the weld. As with the circumferential weld, the stresses both parallel and perpendicular to the weld centerline are strongly tensile in nature, and at no point do they become compressive. As a result, if a crack were to initiate at the surface of the container in the longitudinal weld centerline, it would have a tensile stress available to support propagation through the thickness of the wall.

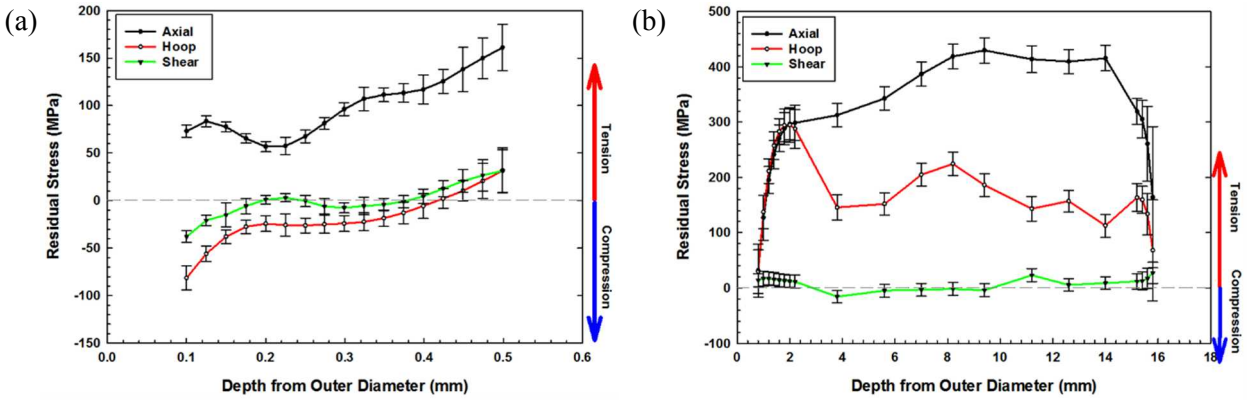

Figure 9: ICHD (a) and iDHD (b) data as a function of distance from the outer diameter of the container for the centerline of a longitudinal weld. Note that because the weld is aligned parallel to the long axis of the container, axial stresses are now parallel to the weld centerline.

As with the circumferential weld, characterization of the stresses in the HAZ was accomplished by performing ICHD and iDHD measurements approximately 4 mm from the weld toe (i.e., edge of the weld fusion zone). As with the other locations, ICHD was used to measure the near-surface residual stresses, the results of which are shown in **Figure 10**. Both the axial and hoop stresses in the near surface region are large and tensile in nature, decreasing in magnitude with depth. iDHD was used to measure the residual stresses through the thickness of the weld. As with the circumferential weld HAZ, through-wall tensile stresses are present, and could support crack propagation through the thickness of the wall.

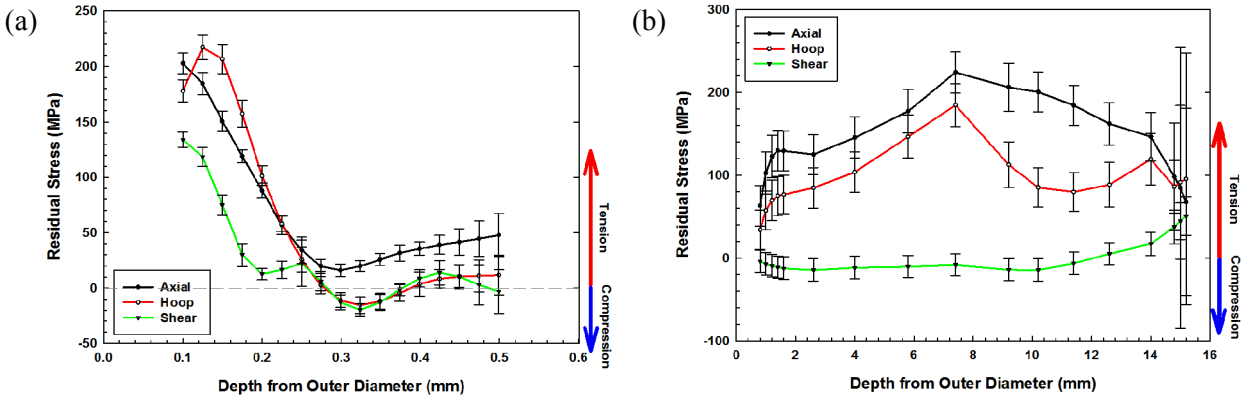

Figure 10: ICHD (a) and iDHD (b) data as a function of distance from the outer diameter of the container for the HAZ of a longitudinal weld. Note that stresses are tensile through the thickness of the plate, and are largest in magnitude in the axial direction.

2.3.1.4 Circumferential Weld Repair

As discussed previously, it is not uncommon for the welds on an interim storage container to have been repaired during the production process (i.e., portions of the weld that are out of compliance with the standards are ground out and the area re-welded). These repair regions have been identified by numerous researchers as having dramatically elevated residual stresses when compared to unrepaired portions of a weld (Dong et al., 2002; Bouchard et al., 2005; Dong et al., 2005; Elcoate et al., 2005; George and Smith, 2005; Hossain et al., 2006; Hossain et al., 2011). No weld defects requiring repair were identified following production. However, because of the impact weld repairs can have on the residual stresses in adjacent material, a repair of a simulated defect was made on each circumferential weld. In these locations, an artificial defect corresponding to a 1/8" diameter hole was drilled partially into the outer

diameter, simulating a small defect such as porosity or an entrained slag particle (illustrated schematically in **Figure 4**). The "defect" was then removed by machining out a larger region via a ¼" drill, after which the edges of the drilled out region were ground to a bevel, such that it could be re-welded.

The repair region was evaluated in the same manner as the unmodified circumferential and longitudinal welds. ICHD and iDHD measurements were made in the center of the repair, as well as in the HAZ. There was an apparent misalignment of the ID and OD welds, so the HAZ was evaluated on both sides of the weld repair, to make sure that possible asymmetries in the stress field were captured. The stress distribution for the center of the weld repair is presented in **Figure 11**. As with the unrepaired regions, the stress is strongly tensile in both the hoop and axial directions. The stress distribution is symmetric – being comparable in magnitude in both of these directions, particularly near the weld surface. This symmetry is consistent with the nature of the weld repair, which was circular in nature. Though the repair was located on the OD, the amplification in the stress state was present completely through the thickness of the weld. This is consistent with what has been observed by other researchers on linear weld repairs in pipes and similar structures.

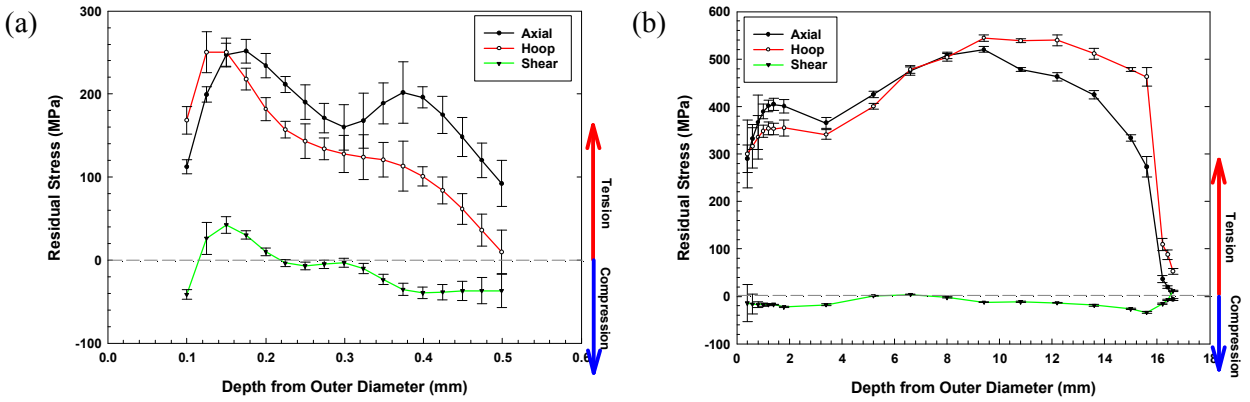

Figure 11: ICHD (a) and iDHD (b) data as a function of distance from the outer diameter of the container for the center of the repaired region in the circumferential weld. Note that stresses are tensile through the thickness of the plate, and are comparable in magnitude in the hoop and axial directions, consistent with the symmetric nature of the repair.

The residual stress data for one of the weld repair HAZ measurements are presented in **Figure 12**; data from the second location was similar, and is provided in Enos and Bryan (2016a). As with the center of the repair, both the axial and hoop stress components were strongly tensile in nature through the thickness of the metal. However, while the axial and hoop stress components were similar in magnitude in the center of the weld, at the two HAZ locations, the axial component (i.e., stresses perpendicular to the centerline of the weld) was substantially larger in magnitude than the hoop stress. The difference was greatest at the surface, with the axial and hoop stresses becoming comparable as the inner diameter surface was approached.

Relative to the unrepaired circumferential weld, the stresses are substantially amplified in the weld repair region, though the shape of the distribution is largely maintained. In the case of the HAZ, however, while the axial stress is substantially increased by the weld repair, the hoop stress remained closer to that observed in an unrepaired region.

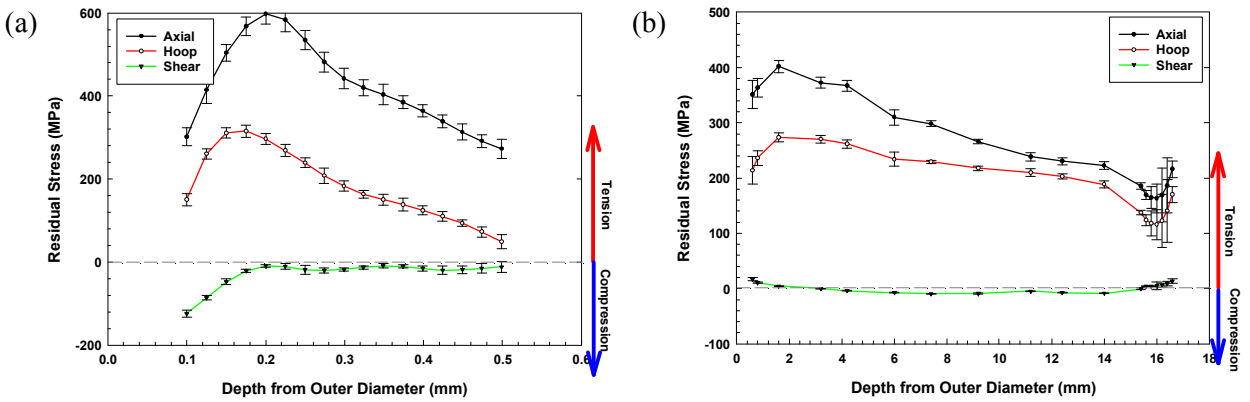

Figure 12: ICHD (a) and iDHD (b) data as a function of distance from the outer diameter of the container for the HAZ associated with the repair of the circumferential weld (location 1). Note that stresses are tensile through the thickness of the plate, and are largest in magnitude in the axial direction.

2.3.2 Contour Method

As discussed previously, the contour method is similar to the DHD and iDHD techniques in that displacements due to stress relaxation are measured at a cut surface, then converted to a pre-existing residual stress. As with DHD, the results can be influenced by plasticity effects due to high levels of residual stress. Unlike the DHD technique, where the stress is measured at a single location through the thickness of the wall, the contour method gives a map of the entire cross section. Contour measurements were made across the longitudinal and circumferential welds, as well as through a weld intersection. Comparisons have been made to the DHD measurements that were made through the same region. While such comparisons can be made, some deviations are to be expected due to heterogeneities which may exist in the weld along its length (e.g., weld pass start/stop locations, etc.).

2.3.2.1 Circumferential Weld Contour Data

A map of the hoop stress as a function of position in the form of both a surface plot and a contour plot for the circumferential weld is presented in **Figure 13**. As can be seen in the figure, the residual stress is strongly tensile through-thickness near the weld centerline, extending approximately 50 mm away from the center of the FZ. Further from the weld centerline, the stress state begins to approach that of the base metal. Note that, on this map and on others presented here, the tensile zones to the far left and right, at the edges of the sample where the raw data and models are less well defined, are exaggerated by the analysis process. Care must be taken when interpreting the contour results in these regions.

The results of the contour mapping and the DHD measurements show reasonable agreement, matching well for the weld centerline, but significant differences do exist, especially in the weld HAZ. The results are compared and discussed in Enos and Bryan (2016a).

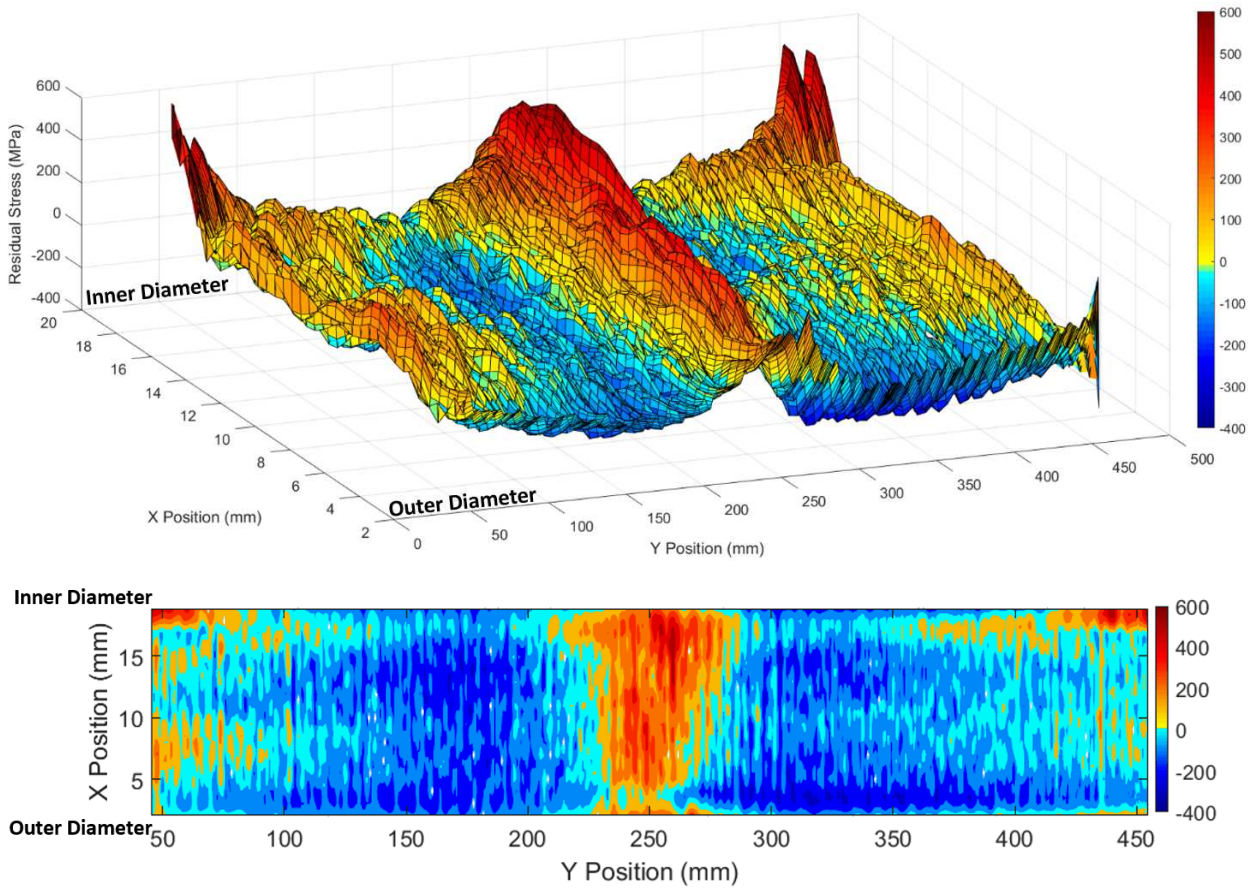

Figure 13: Contour map across a circumferential weld. Primary stress illustrated is the hoop stress (parallel to the weld direction). The cross section is 400 mm in length, and centered around the weld centerline. Red, yellow, and green represent tensile stresses, while blue represents compressive stresses. The through-wall tensile stress field extends approximately 50 mm from the weld centerline.

2.3.2.2 Longitudinal Weld Contour Data

A map of the axial stress as a function of position for the longitudinal weld in the form of both a surface plot and a contour plot is presented in **Figure 14**. As can be seen in the figure, the residual stress is strongly tensile through thickness near the weld centerline, extending approximately 25 mm away from the center of the FZ. Further from the weld centerline, the stress state begins to approach that of the base metal. As was indicated in the discussion of the deep hole drilling data, the stress levels were higher in regions near the weld. This is also apparent in the contour, however, while the peak stresses are higher than those found for the circumferential weld, the width of the stress field is smaller.

As with the circumferential weld, the results of the contour mapping and the DHD measurements matching well for the weld centerline, but significant differences exist in the stresses predicted in the weld HAZ. The results are compared and discussed in Enos and Bryan (2016a).

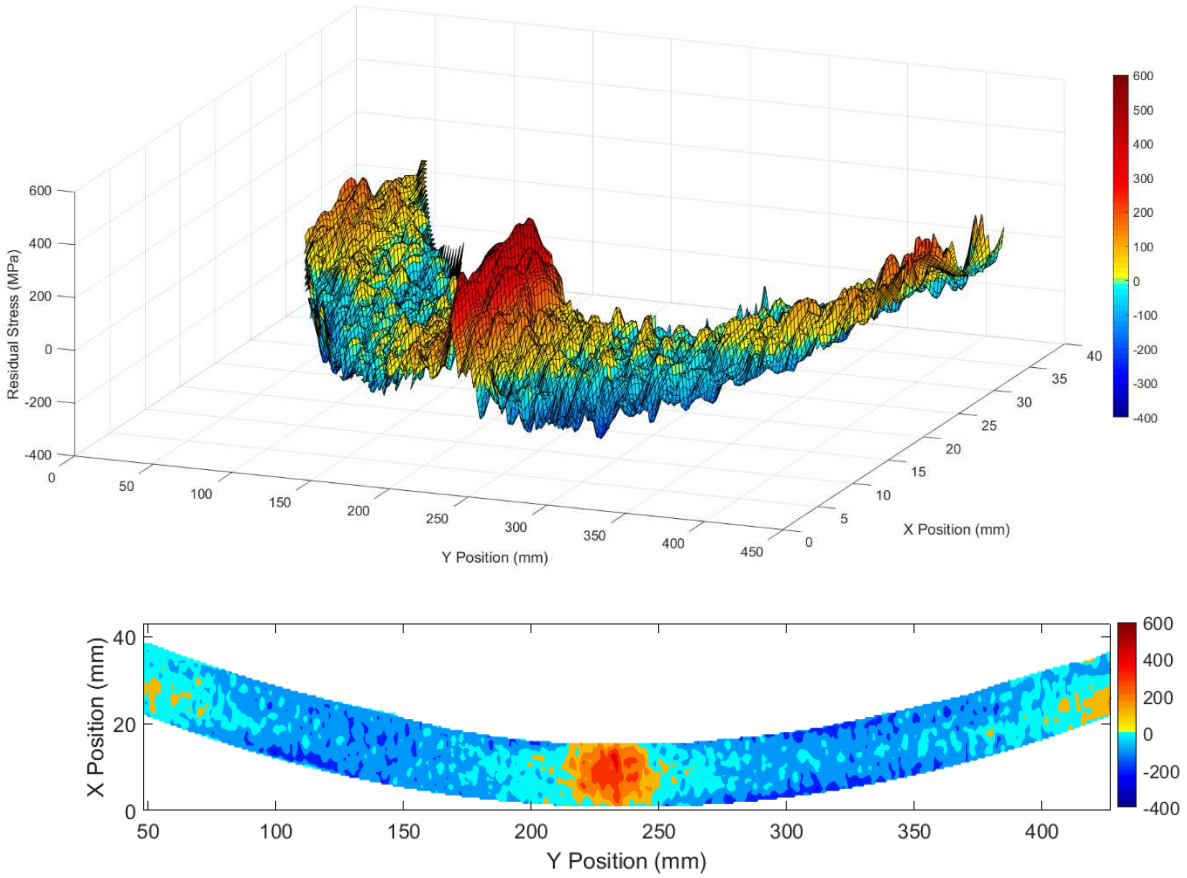

Figure 14: Contour map across a longitudinal weld. Primary stress illustrated is the axial stress (parallel to the weld direction). The cross section is 400 mm in length, and centered around the weld centerline. Red and yellow represent tensile stresses, while green and blue represent compressive stresses. The through-wall tensile stress field extends approximately 25 mm from the weld centerline.

2.3.2.3 Weld Intersection Contour Data

A final contour measurement was made at the intersection of a circumferential weld with a longitudinal weld, shown in the form of both a surface plot and a contour plot in **Figure 15**. As seen in the figure, the distribution is markedly different than the cross section through the circumferential weld presented in **Figure 13**. While the magnitude appears similar, the stress field extends further from the FZ centerline, and appears to be biased towards the inner diameter of the container. In addition, the hoop stress in the longitudinal weld centerline has become compressive, unlike the tensile stress field illustrated for regions far from the weld intersection, and illustrated via iDHD in **Figure 9**.

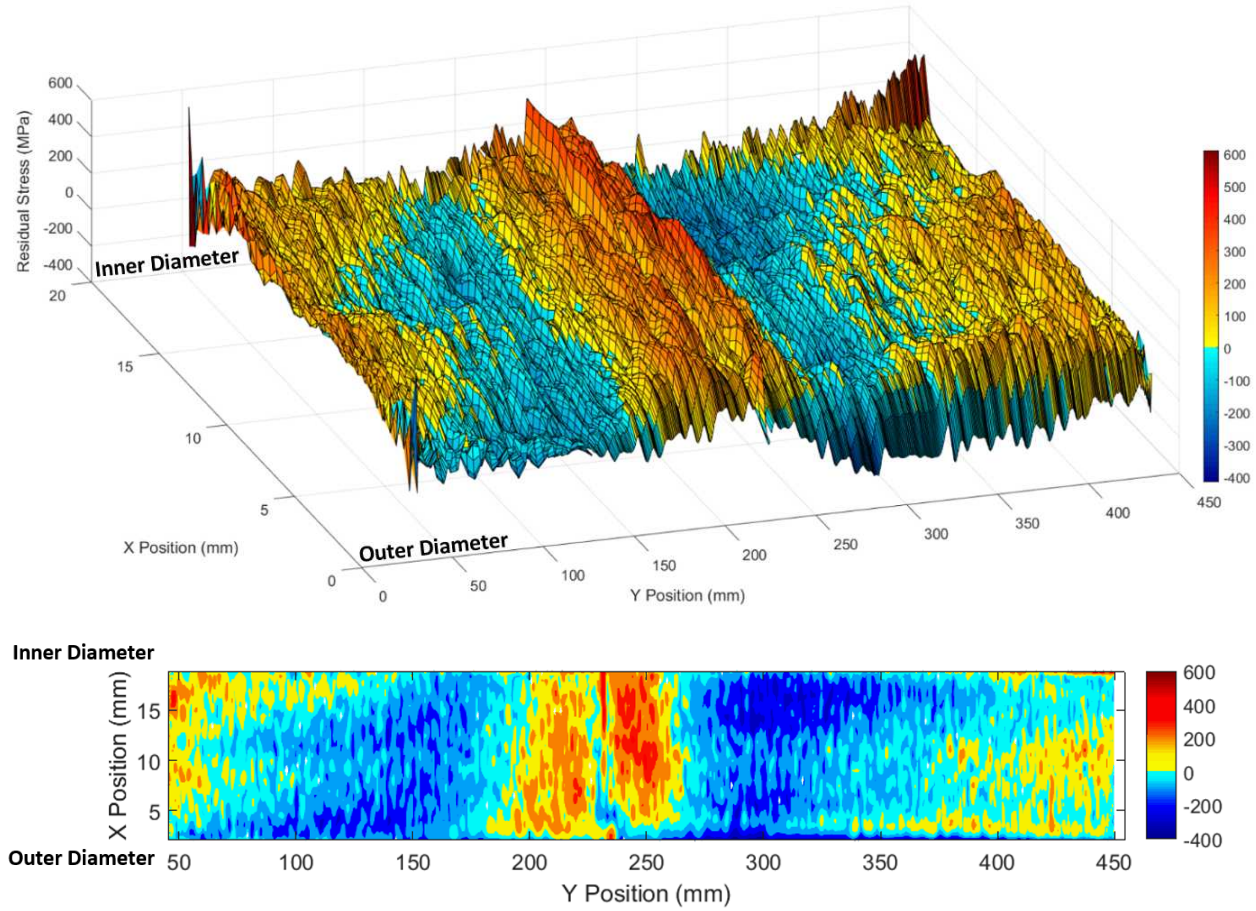

Figure 15: Contour measurement through the intersection of a longitudinal weld with a circumferential weld. The contour is centered on the circumferential weld, with the longitudinal weld being to the right, and the lower container shell to the left.

2.3.3 X-Ray Diffraction

X-ray diffraction was used to assess the residual stress associated with the base metal, the circumferential welds, and the intersection of a circumferential weld with a longitudinal weld. Due to the low penetration depth of x-rays into the metal being evaluated, only the very near surface stresses can be measured (i.e., tens of microns into the sample) – much closer to the surface than any of the other techniques used here are capable of. The technique was unsuccessful at obtaining the residual stress state on the weld itself (i.e., the weld FZ) due to a combination of the microstructure and surface topography in that region, but was able to obtain data in the HAZ moving away from the weld. The measured stresses are strongly compressive in the HAZ adjacent to the weld FZ, but become tensile beyond approximately 100mm from the weld centerline. The magnitudes of the axial and hoop stresses are comparable to one another, though the hoop stress appears to approach the stress associated with the base metal more rapidly than the axial stress. The presence of a strong compressive stress is in contrast to the ICHD data which shows a predominantly tensile stress in the hoop direction, and slightly compressive in the axial direction for the HAZ associated with the circumferential weld, and strongly tensile in both the axial and hoop directions for the HAZ associated with the longitudinal weld or with the weld repair region in the circumferential weld. The reason for this discrepancy is likely due to the very shallow depth that the XRD technique is able to sample, coupled with the surface condition of the mockup container welds. The weld bead and the region surrounding the welds were ground. This mechanical deformation can significantly alter the stress state and plastic strain experienced by the material, as discussed by Ghosh and Kain (2010).

Near-surface residual stresses were also evaluated for the intersection of a longitudinal weld with a circumferential weld. As with the circumferential weld, the XRD technique was not able to discern the stress state in the weld FZ, and the stresses in the HAZ were compressive in nature, with the magnitude decreasing with distance from the weld intersection point. The compressive residual stress is, again, likely the effect of the surface grinding of the weld region. Finally, the surface stress in the base metal, far from a weld, was assessed. In this case, while the axial stresses were compressive, the hoop stress was tensile in nature.

2.3.4 Ultrasonic Measurement

Ultrasonic measurements were conducted in three locations: across a longitudinal weld, across a circumferential weld, and across the intersection of a longitudinal weld with a circumferential weld (passing along the centerline of the longitudinal weld, across the circumferential weld and into the base metal). The resulting data from each ultrasonic measurement location is compared to similar measurements made via the contour and hole drilling techniques discussed above in **Figure 16**. For comparison purposes, the contour and DHD data have been averaged over the same gauge length and depth interval as the ultrasonic measurements. Note that because of the averaging, the ultrasonic technique cannot resolve locally high stresses captured by the contour measurement.

In contrast to the other techniques, values obtained through ultrasonic measurements are indicative of the stress state within a volume of material. As such, they are effectively averaged, and were anticipated to yield a smoother response with significantly reduced point to point irregularities/noise. The accuracy of the measurement is a function of the parameters derived to describe the acousto-elastic property of the material. In this study, while two separate locations (one in the base metal, and one in the weld fusion zone, with replicates of each location used) were used, a single value was determined and assumed to be applicable in all locations. As the parameters used to describe the acousto-elastic properties of a material are also a function of microstructure, it is anticipated that the use of a single value for all locations will result in some inaccuracies. Nevertheless, as a proof of concept experiment, the resulting inaccuracy is acceptable.

In **Figure 16**, it can be seen that the peak stress at the primary weld centerline for each ultrasonic measurement location was comparable. The difference seen both by deep hole drilling and the contour measurement method was not observed. Aside from that, the shape and relative magnitude of the stresses reported from the ultrasonic measurements were comparable to those obtained via other techniques. As such, it appears that the ultrasonic measurement technique offers great promise as a non-destructive stress measurement method, with the potential to offer a precision comparable to other techniques that, while they yield a more complete map (e.g., contour measurement or deep hole drilling), are destructive in nature and as such may not be used in many applications. As an example, an immediate application for this technique would be to evaluate new storage containers for repair regions that result in an unacceptably high residual stress state. This would allow the end user to then either reject the container, or apply a stress mitigation method to the region with a highly elevated stress state.

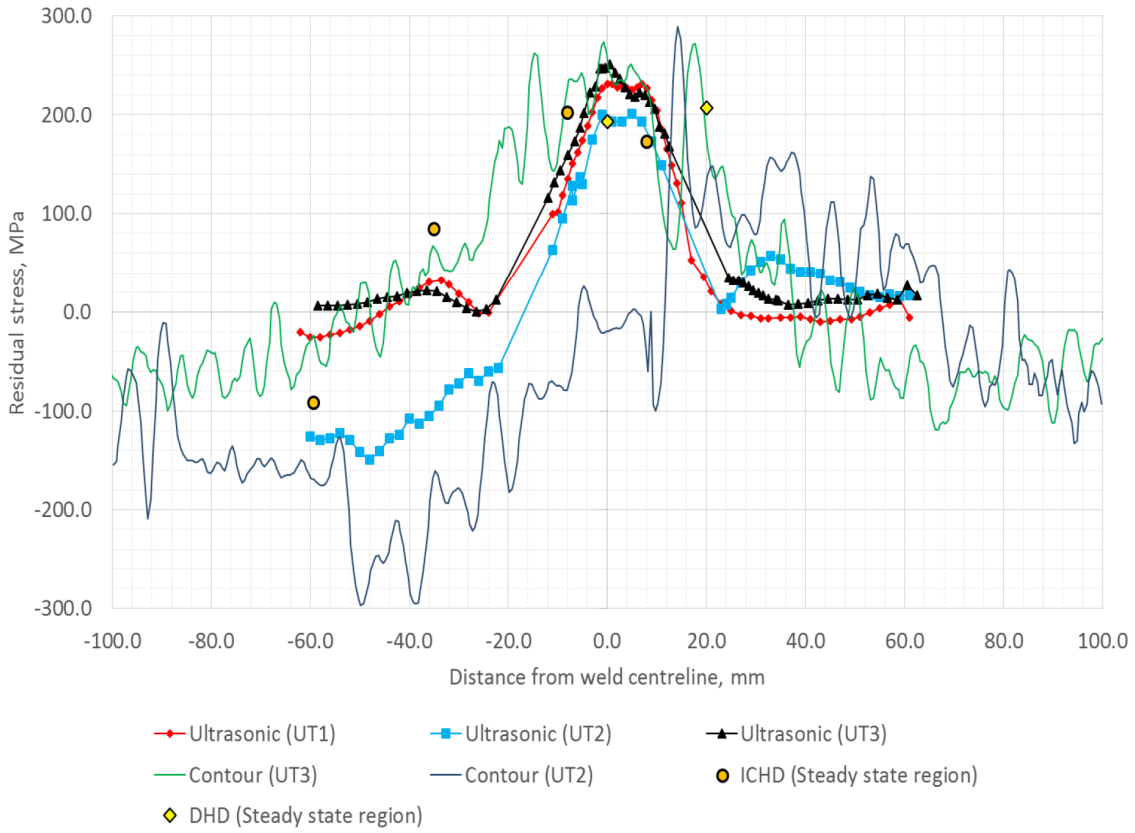

Figure 16: Comparison of ultrasonic measurements to those obtained through contour measurements and hole drilling measurements. UT1 is a transect across a circumferential weld; UT2, a transect across the intersection of the longitudinal and circumferential welds; and UT3, a transect across a longitudinal weld.

2.4 Conclusions: Mockup Weld Residual Stress Measurements

Assessment of residual stresses associated with forming and welding was performed using a combination of four techniques. These include deep-hole drilling, the contour method, x-ray diffraction, and ultrasonic testing. The deep-hole drilling technique allows measurement of residual stresses along a one-dimensional hole drilled through the wall of the cylinder; it allows the residual stresses within the container to be assessed while it is intact and hence, captures the effects of the cylindrical constraint on the stresses. The contour method provides a two-dimensional map of stresses along a cross section through a region of interest; however, the mockup must be cut into pieces to measure the face of the cross section, and stresses due to the constraint of the intact cylinder are lost. X-ray diffraction allows assessment of very shallow near-surface stresses associated with shaping and grinding the mockup. It is also used to map stress components that are in-plane with the cross sectional surface, when using the contour method. Ultrasonic testing evaluates the change in sound velocity due to a change in local stress, and is able to evaluate average stresses for a depth from 0 to 2.8 mm within the stainless steel (as implemented here). The ultrasonic technique is non-destructive, and relatively new as a stress analysis method. It has been included here for comparison to the other techniques.

After fabrication, the mockup was cut in half. One half was reserved for residual stress measurements. The other half was further subdivided, one part being retained for material characterization studies, and a second part provided to EPRI for assessment of SCC evaluation methods. During the cutting process, strain gauges were used to monitor stress relaxation at locations where weld residual stresses were

measured, so that it could be added back in if necessary to obtain the as-manufactured residual stresses. However, cutting the cylinder in half had little effect on residual stresses; measured strains were very small, and can be ignored.

Several methods are available for residual stress measurement, and two, DHD and the contour method, are able to capture the through-thickness stress distribution. While the contour measurement method has been found to found to have issues with steep stress gradients, it provides an overall map of a cross section. The DHD technique can be more accurate, but it only provides the through-thickness stress distribution at a single location. As a result, both techniques were applied to the mockup.

DHD measurements were completed within the FZ and HAZ for the circumferential and longitudinal welds. Similar measurements were made in a portion of a circumferential weld that had undergone a simulated weld repair. A final measurement was performed in the base metal, far from the welds. Results indicate that the base metal, residual stresses are dominated by those introduced during the forming of the plate to make a cylinder. The forming process used to shape the stainless steel plates into a cylinder extended the outer surface of the shell while shortening the inner surface, and the residual stresses reflect this; except for near-surface regions, the outer half of the shell wall is under tension, while the inner half of the wall is under compression. The stresses associated with the weldments were substantially larger in magnitude than the base metal, with peak values in excess of the uniaxial yield strength for annealed 304L stainless steel. The stress within the weldments is the result of shrinkage during solidification of the molten metal in the weld fusion zone upon cooling. These stresses are the result of the constraint placed by the structure of the container (and any additional fixtures used during fabrication) on the weld as it solidifies. For both circumferential and axial welds, the stresses both within the weld FZ and HAZ were found to be strongly tensile in the weld-parallel direction through the entire thickness of the container wall.

Contour measurements were completed across the circumferential weld, the longitudinal weld, and at the intersection of a circumferential weld and longitudinal weld. As with the DHD measurements, the contour measurements indicated that the weld-parallel stress field associated with each of the welds was strongly tensile through the entire wall thickness. The distance over which the stress field remained completely tensile extended approximately 25mm from the weld centerline for longitudinal welds and 40mm from the weld centerline for circumferential (weld beads were approximately 25 mm wide). The strongly tensile region was narrower for the longitudinal weld, but larger in magnitude, again consistent with the DHD measurements. At the intersection of the two welds, the stress field was similar, except that the tensile region became wider, extending further from the circumferential weld centerline at the location of the intersection.

X-ray diffraction measurements were made on the base metal, on and around the circumferential weld, and at the intersection of the longitudinal and circumferential welds. Unlike the DHD or contour measurement techniques, X-ray diffraction analyzes only the stresses very near (tens of microns) to the sample surface. Since the weld beads and nearby surfaces for both the longitudinal and circumferential welds had been mechanically ground, the near-surface stresses were found to be strongly compressive. While compressive stresses would tend to prevent crack initiation, care must be taken in the interpretation of the X-ray diffraction data, as a typical localized corrosion site would be deeper than the stress field that has been measured. As such, the stresses that would be acting on the localized corrosion site, potentially promoting crack initiation, would likely be quite different than the results from x-ray diffraction. While the very near surface stresses may not be important for crack initiation and propagation, they can increase the susceptibility of the material to localized corrosion initiation, and as such should not be dismissed as being irrelevant.

Ultrasonic measurements of the residual stress were made in the same locations as the contour mapping and incremental deep hole drilling measurements. Results obtained, while limited to averaged values for a depth of 0-2.8 mm within the material, were consistent with those reported through the other techniques.

While the tooling for ultrasonic measurement, as implemented here, is bulky and does not yet lend itself to inspection of fielded storage containers, it does represent a powerful non-destructive method to evaluate the stress state associated with weldments. Furthermore, implementation of such a technique may be able to reveal the location of weld repairs, where the local stress state may be elevated relative to the steady state portions of a weldment.

Now that the stress states have been characterized, the mockup will be sectioned into coupons to provide samples for evaluation of the microstructure and electrochemical properties of the welded regions, and for SCC initiation tests. These coupons are critical for the Spent Fuel Waste Science and Technology Program, but also are of great interest to outside parties such as EPRI and the academic groups working on canister SCC as part of a DOE Nuclear Energy University Program. Samples will be disseminated to interested parties on an as-needed basis, with the UFD program getting first priority, followed by the DOE-funded NEUP groups and EPRI.

3. BRINE STABILITY EXPERIMENTS

Charles Bryan and David Enos, Sandia National Laboratories

Once deposited on the canister surface, several processes can affect the composition of deposited salts or of the brines that form when they deliquesce. Some of these can occur prior to deliquescence; others can only occur after a deliquescent brine has formed, or, at least, require that the RH be sufficiently high that a thin adsorbed water film is present on the salt surface. In FY15, experimental began evaluating the stability of common salts found in atmospheric aerosols and the brines that would form upon deliquescence of these salts on the heated surface of SNF storage canisters. This work is documented in the FY15 status report for the S&T experimental work done at SNL (Bryan and Enos, 2015a). That work focused on the stability of inland salt aerosols, which are ammonium-rich. Some ammonium minerals are known to be thermally sensitive, decomposing at even slightly elevated temperatures via the following reactions.

$$NH_4Cl(s) \leftrightarrow NH_3(g) + HCl(g)$$

$$NH_4NO_3(s) \leftrightarrow NH_3(g) + HNO_3(g)$$

$$(NH_4)_2SO_4(s) \leftrightarrow 2NH_3(g) + H_2SO_4\ (g)$$

As ammonia degasses, there is concomitant loss of an acid gas species. Experiments with bulk salts have shown that ammonium chloride and ammonium nitrate reactions are very rapid even at moderately elevated temperatures (SNL, 2008). In those experiments, at 100ºC, the reaction was complete within days or weeks; even at 50ºC, a large fraction of the minerals would be lost over years. Ammonium sulfate decomposition is much slower; it would be complete in less than 1 year at 100ºC, but the salt could persist with little loss at lower temperatures (SNL, 2008). For fine particulates such as atmospheric aerosols, loss is rapid even at ambient temperatures—loss of nitrate due to volatilization of particulate ammonium nitrate from sampling filters is a widely recognized bias in atmospheric dust sampling (Zhang and McMurry, 1992; Chang et al., 2000). It is evident that ammonium salts deposited on a hot dry storage container will decompose rapidly, taking a significant fraction of acid gas anions with them. The ratio of cations removed is a function of the identity of the salt phases—for atmospheric aerosols, most ammonium is associated with sulfate, and to a lesser degree, nitrate (Seinfeld, 1986); however, if the small amount of chloride present in inland aerosols is present as ammonium salts, it will also be lost over time. If the rate of loss is more rapid that the rate of deposition, then there can be no accumulation of ammonium chloride on canister surfaces. It was anticipated that finely dispersed salts such as atmospheric aerosols would degas much more rapidly than was observed in the previous experiments using bulk amounts of salt (SNL, 2008). In FY15, SNL evaluated decomposition rates for ammonium nitrate and chloride as a function of temperature under essentially dry conditions (RH = 11-13%). The degassing rates of the deliquesced single-salt brines were also evaluated.

The experimental method employed for the tests is described in (Bryan and Enos, 2015a) and involved the use of a quartz crystal microbalance (QCM), a device capable of measuring nanogram quantities of deposited salts. An airbush mounted to a computer controlled stage was used to deposit a thin, even coat of each salt onto a QCM wafer (Figure 17), which was then placed into an environmental chamber, and heated to temperatures of 30-50ºC at RH values well below the deliquescence RH for that salt. The samples were held at temperature for 2-24 hours, and the rate of weight loss as the salts decomposed was measured. Following the dry tests, the RH was increased to above the deliquescence point, and held for an additional time period, to evaluate degassing rates from the deliquesced brines. The weight loss due to decomposition of the non-deliquesced salts could be measured in real time. However, once deliquesced, the salts decoupled from the surface of the QCM wafer, and masses could not be measured. Therefore, for the deliquesced condition, weight loss was measured the mass difference between the dry salts prior to deliquescence, and then remaining salt mass after re-drying the salts following the deliquescence interval.

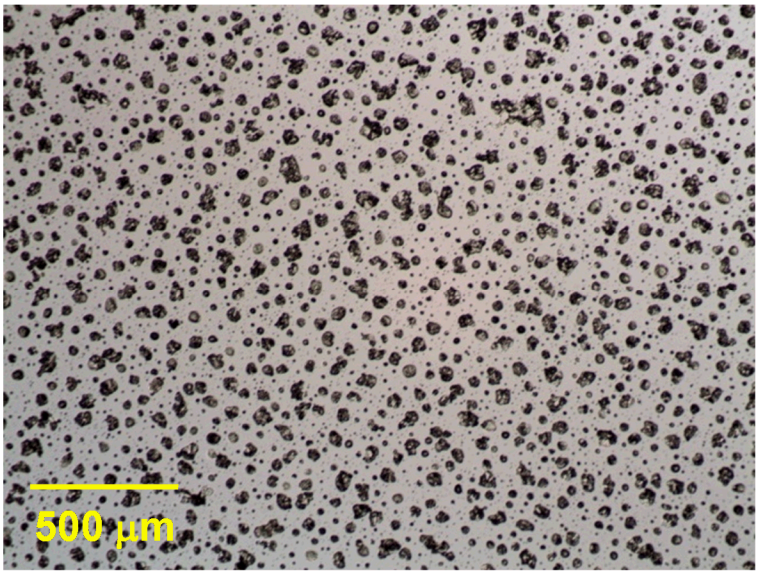

Figure 17. QCM wafer coated with 100 µg/cm^2 (1 g/m^2) of evenly dispersed $NaNO_3$.

The results, documented in Bryan and Enos (2015a) and in Enos and Bryan (2016b), showed that finely-dispersed ammonium nitrate and ammonium chloride decomposed vary rapidly, even at temperatures as low as 30ºC. At 50ºC, even a relatively heavy salt load (1 g/m^2), present as either dry or deliquesced salts, would degas from the canister surface within days. Even at 30ºC, complete degassing would occur within several weeks. This rate of loss is far greater than any conceivable deposition rate for these salts, indicating that they could not accumulate of persist on a canister surface at even slightly elevated temperatures.

However, preliminary results with ammonium sulfate, $(NH_4)_2SO_4$, suggested that it would not decompose at these low temperatures, and could accumulate over time on the canister surface. This is important because ammonium is the most abundant cation at inland sites, and sulfate, the most abundant anion; ammonium sulfate is a major component of many inland salt aerosols. Moreover, chlorides such as NaCl is not thermally sensitive, and if deposited on a canister surface could also accumulate. Chlorides are not generally abundant in inland aerosols, but could be locally present due to salting of nearby roads, or emissions from nearby cooling towers. While these two species could accumulate on a canister surface prior to deliquescence, SNL hypothesized that once they deliquesced to form a mixed salt brine, coupled ammonium/ acid degassing would occur. In the case of a mixed brine, the identity of the cation lost is no longer a function of the original ion association in the deposited mineral. Instead, the brine will degas ammonia and acid gas cations in proportion to their equilibrium vapor pressure above the brine. This means that chloride deposited as any chloride salt will be degassed, if ammonium, deposited as any ammonium salt, is present. For instance, assume that NaCl and $(NH_4)_2SO_4$ are deposited on the canister. Once deliquescence occurs, the following reaction can occur:

$$2NaCl(s) + (NH_4)_2SO_4(s) \leftrightarrow Na_2SO_4(s) + 2HCl(g) + 2NH_3(g)$$

where ammonia and HCl are degassed and lost from the canister surface, and the salts are converted to sodium sulfate. Similar reactions can be written for Mg-Cl_2 or Ca-Cl_2 phases or the equivalent NO_3^- phases, all resulting in loss of the mineral acid and ammonia from the canister surface. These reactions may be very important in limiting chloride accumulation at inland sites, where ammonium salts are the dominant components of atmospheric aerosols.

Two salt/brine stability experiments were carried out in FY16. First, degassing experiments were carried out with $(NH_4)_2SO_4$, to confirm preliminary results from FY15 that this salt did not decompose in the

solid state at moderately elevated temperatures, and did not degas significantly once deliquesced. The second experiment evaluated the stability of a mixed $(NH_4)_2SO_4$-NaCl assemblage, and whether the mixture would degas ammonium and HCl once it deliquesced, as hypothesized above.

3.1 $(NH_4)_2SO_4$ stability

Preliminary experiments with $(NH_4)_2SO_4$ carried out in FY15 indicated that deliquescence occurs between 75% and 80% RH, but there is measurable water adsorption onto the salt surfaces as low at 55% RH. Degassing results at 50ºC seemed to be consistent with those in SNL (2008). Over the course of a several-hour experiment, no measurable decomposition of the solid phase occurred. Degassing under deliquescent conditions was not evaluated. Longer duration experiments (>50 hours) with $(NH_4)_2SO_4$ were carried out in FY16 under both dry and deliquesced conditions. No measurable mass loss was observed at temperatures of 30-50ºC, indicating that ammonium sulfate occurs very slowly or not at all at those temperatures.

3.2 $(NH_4)_2SO_4$-NaCl assemblage stability

This experiment tested the hypothesis that ammonium sulfate and sodium chloride, if accumulated on the surface of a spent nuclear storage canister as dry salts, would react upon deliquescence, forming a brine that would degas NH_4(g) and HCl(g). In order to mimic the conditions on the surface of a spent nuclear canister, it was necessary to deposit the two salts separately, without allowing them to react. To do this, the airbrush setup used for the previous work (Bryan and Enos, 2015a) was used. First, a 0.1 M aqueous solution of $(NH_4)_2SO_4$ was mixed, and sprayed on a QCM wafer and two adjacent stainless steel coupons, using the QCM to monitor deposition density. After allowing the samples to completely dry (the deposited mass stabilized), the NaCl was deposited using a methanol carrier, to prevent dissolution and mixing with the ammonium sulfate. One metal coupon was used in the degassing experiment; the other was stored in a desiccator and used as a control. At the end of the experiment, the salts were leached off of both coupons with deionized water, analyzed, and compared to determine if degassing had occurred, the control sample providing information on the initial salt distributions and ion concentrations.

The distribution and composition of the deposited salts was evaluated by scanning electron microscopy (SEM) imaging and energy-dispersive X-ray spectral (EDS) analysis. A SEM image of the initial deposited salts on the control sample is shown in **Figure 18**. The ammonium sulfate did not deposit evenly, but instead beaded up to form large (200-300 μm) droplets. These apparently dried slowly, crystallizing into coarse crystals (**Figure 19**). The hollow morphology of the droplets suggests that they dried from the outside-in, and that trapped brine may have been present beneath the crystallized shell, perhaps for a significant time. The NaCl formed a finely-dispersed coating over the both metal and the ammonium sulfate.

The results of the chemical analysis of the control sample (discussed later) show that the two step deposition procedure was largely successful in limiting reaction between the two phases, but some reaction did occur. This can be seen in **Figure 20**, which shows EDS element maps for one of the $(NH_4)_2SO_4$ droplets. The droplet is well defined in the maps of oxygen and sulfur, but nitrogen (ammonium) is somewhat depleted along one side. The N-depleted area corresponds to a region that had a somewhat higher coating of NaCl, as indicated by the Na map. Cl is depleted over the entire area of the $(NH_4)_2SO_4$ droplet. It seems likely that the ammonium sulfate was not entirely dry when the NaCl was deposited, and in areas of overlap, some reaction and loss of ammonium and chloride occurred.

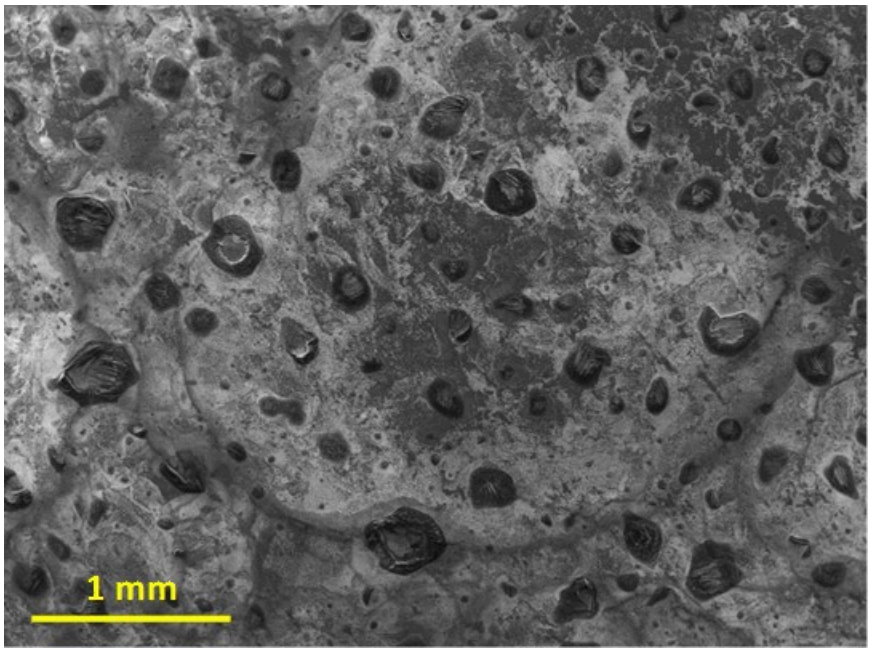

Figure 18. SEM image of the control sample, a stainless steel coupon coated with ~60 µg/cm^2 (0.6 g/m^2) each of $(NH_4)_2SO_4$ (large aggregates), and NaCl (finely dispersed coating on metal and on $(NH_4)_2SO_4$).

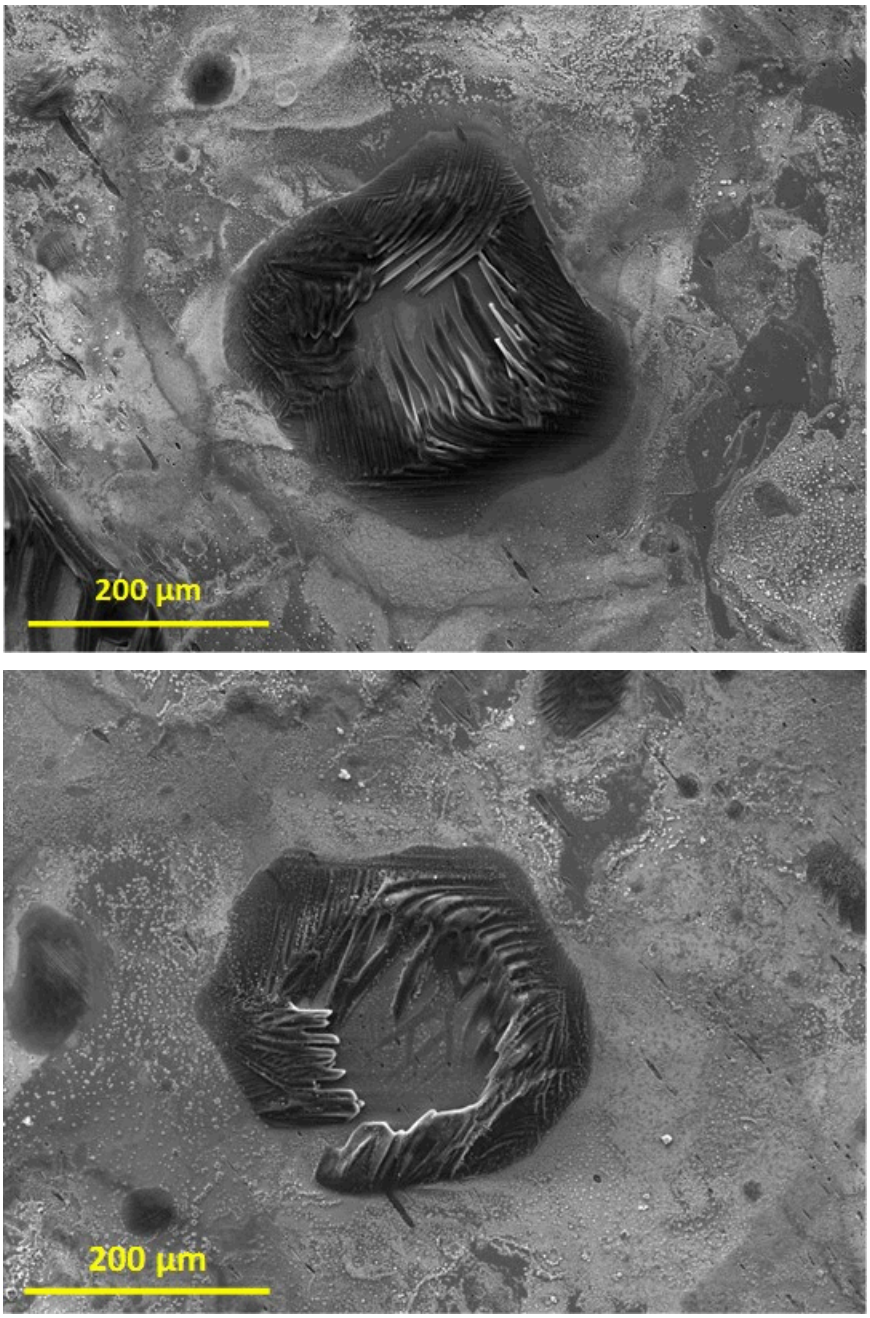

Figure 19. Magnified SEM images of crystallized droplets of ammonium sulfate, illustrating the coarsely crystalline nature and the hollow structure of the droplets. The ammonium sulfate and the surrounding metal are coated with finely crystalline NaCl.

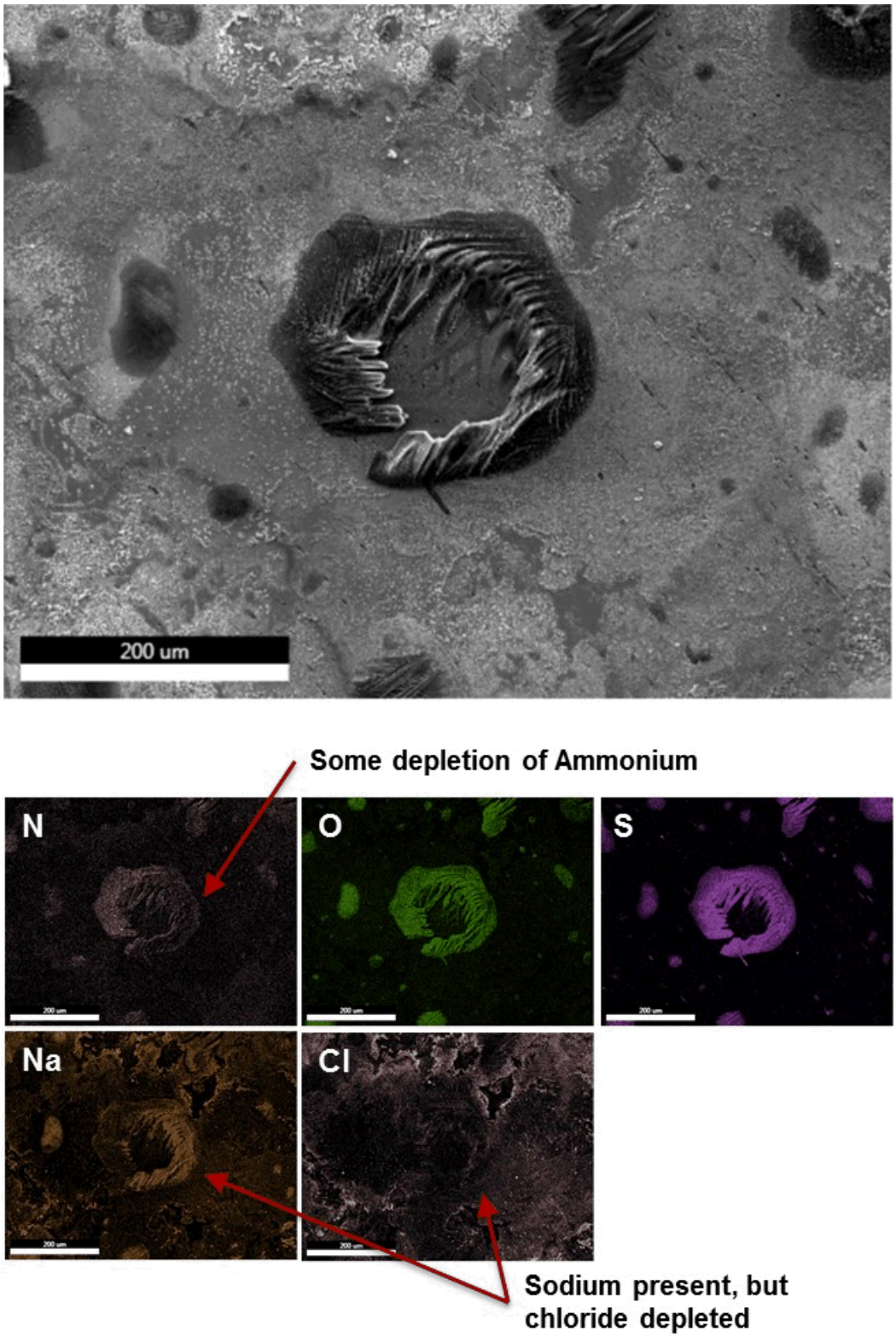

Figure 20. SEM image and element maps of a crystallized droplet of ammonium sulfate, showing depletion of ammonium and chlorine in areas where the two deposited salts (NaCl and $(NH_4)_2SO_4$) overlap.

In the experiment, the test coupon was placed in an environmental chamber at 50ºC at 10%RH, well below the deliquescence RH for the salts, and held there for a few days to ensure dryness. Then, the RH was raised to 75% RH, sufficiently high for the salts to at least partially deliquesce, as indicated by changes in the mass measured by the QCM—when the salts deliquesce, they decouple from the surface of the QCM wafer, resulting in a huge apparent mass loss. After 24 hours at 75% RH, the sample was dried at 10% RH overnight.

After the experiment, the treated sample was examined by SEM (**Figure 21**). The two salts had completely redistributed, forming clumps a coarsely crystalline dendritic NaCl with associated anhedral sulfate, which consisted of mixed $(NH_4)_2SO_4$ and Na_2SO_4. This remobilization and recrystallization indicates that the salts deliquesced and intimately mixed.

After SEM analysis, the treated and control samples were leached with 20 ml deionized water, and the salts analyzed by anion and cation chromatography (IC). Samples were analyzed in duplicate to evaluate analytical uncertainty. Measured total ion concentrations are given in **Table 1** (micrograms). In **Table 2**, the ion concentrations have been divided by the coupon surface areas to get concentrations in $\mu g/cm^2$. The originally-deposited amounts of the two salts were calculated from the Na and SO_4 concentrations for the untreated sample (Na does not degas, and SO4 degases only slightly), and confirm that the two salts were deposited in nearly equal amounts, as intended. Of the species present, only Na cannot be affected by degassing processes; Na concentrations per unit area for the control sample and the treated sample are identical, verifying that the automated airbrush deposited the salts on both samples evenly. Results for the sample duplicates match well, and the sample charge balances were very good (less than 1%), indicating that analytical and experimental uncertainties are small relative to the observed variations in the concentrations measured.

Table 3 presents the data in micro-equivalents, and averaged values for the duplicate analyses are shown in **Figure 22**. The control sample provides the composition of the initially deposited salts, and variations in the initial concentrations of Na and Cl; or NH_4 and SO_4, indicate species loss by degassing. Evidence of minor reaction of the two salts and degassing of NH_3 and HCl during the deposition process was observed when the control sample was examined by SEM (**Figure 20**), and the measured ion concentrations confirm this. The Cl concentration in µEq is 3-4% lower than the Na concentration the control sample, indicating loss of Cl. Similarly, the NH_4 concentration in the control is a few percent lower than the SO_4 concentration, indicating that NH_4 degassed.

Compositional differences between the control sample (as-deposited salts) and the treated sample are much greater. Over 40% of the NH_4 was lost, and over 30% of the Cl. Unexpectedly, a significant fraction (over 10%) of the SO_4 was also lost, by degassing as H_2SO_4. This was surprising, because the single salt $(NH_4)_2SO_4$ did not measurably degas at these temperatures, either in the dry or deliquesced state (Section 3.1). Apparently, the mixed salt solution promotes sulfuric acid degassing. When degassing occurs, the solution will be buffered at a pH at which NH_4 and acid degassing rates are equal, and it may be that the pH is lower for the mixed salt solution than for the deliquesced single salt.

The results indicate that as predicted, it is not possible for a brine containing ammonium and chloride to persist for long periods on the surface of a heated storage canister. At 50ºC, assuming a relatively high initial chloride surface load of 0.66 g/m^2 (equal to 1 g/m^2 NH_4Cl), the rate of chloride loss is sufficient to degas all chloride from a canister surface within 5.2 days. If it is assumed that the activation energy is the same as has been previously determined for degassing of NH_4Cl from a single-salt brine, then at 30ºC, the chloride loss would be complete in about 50 days. This is far higher than any conceivable chloride deposition rate.

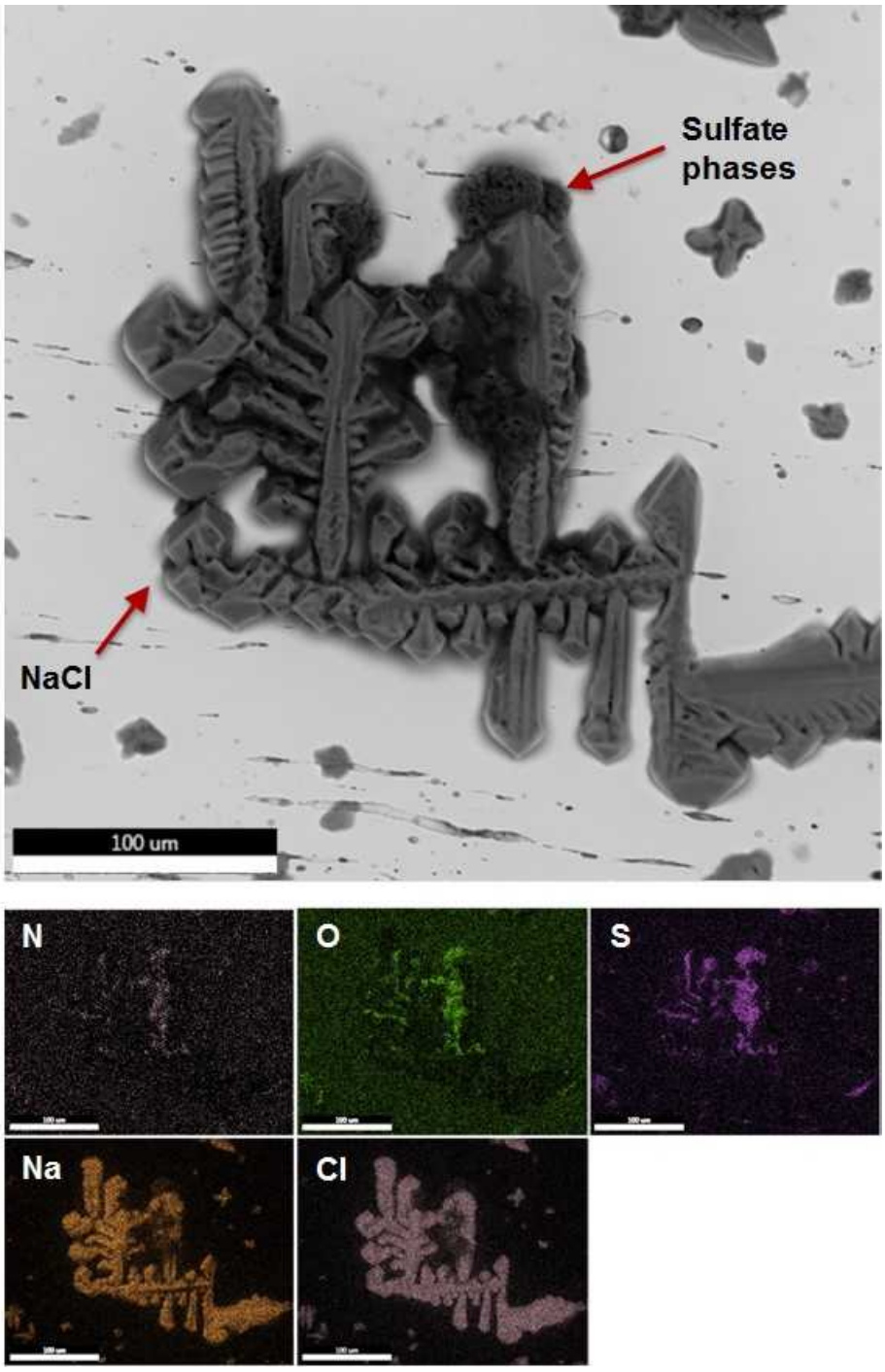

Figure 21. SEM image and element maps the treated sample after testing. The recrystallized and redistributed NaCl and $(NH_4)_2SO_4$ confirm that deliquescence occurred.

Table 1. Total ion concentrations (µg) in sample leachates.

	Total present, µg			
Sample #	**Cl**	**SO_4**	**Na**	**NH_4**
Untr-1	444.9	564.9	298.6	202.5
Untr-2	444.2	563.1	297.2	210.4
Tr-1	310.8	496.3	297.5	108.5
Tr-2	311.1	496.2	297.1	109.2

Table 2. Ion concentrations (µg/cm^2) in in sample leachates.

	Concentration, µg/cm^2				µg/cm^2 deposited	
Sample #	**Cl**	**SO_4**	**Na**	**NH_4**	**$(NH_4)_2SO_4$**	**NaCl**
Untr-1	36.7	46.6	24.6	16.7	64.1	62.6
Untr-2	36.7	46.5	24.5	17.4	63.9	62.4
Tr-1	25.7	41.0	24.6	9.0		
Tr-2	25.7	41.0	24.5	9.0		

Table 3. Total ion concentrations (µEq) in sample leachates.

	Concentration, µEq				Sum anion µEq	Sum cation µEq	Charge imbalance, %
Sample #	**Cl**	**SO_4**	**Na**	**NH_4**			
Untr-1	12.6	11.8	13.0	11.2	24.3	24.2	-0.21%
Untr-2	12.5	11.7	12.9	11.7	24.3	24.6	0.69%
Tr-1	8.8	10.3	12.9	6.0	19.1	19.0	-0.37%
Tr-2	8.8	10.3	12.9	6.1	19.1	19.0	-0.33%

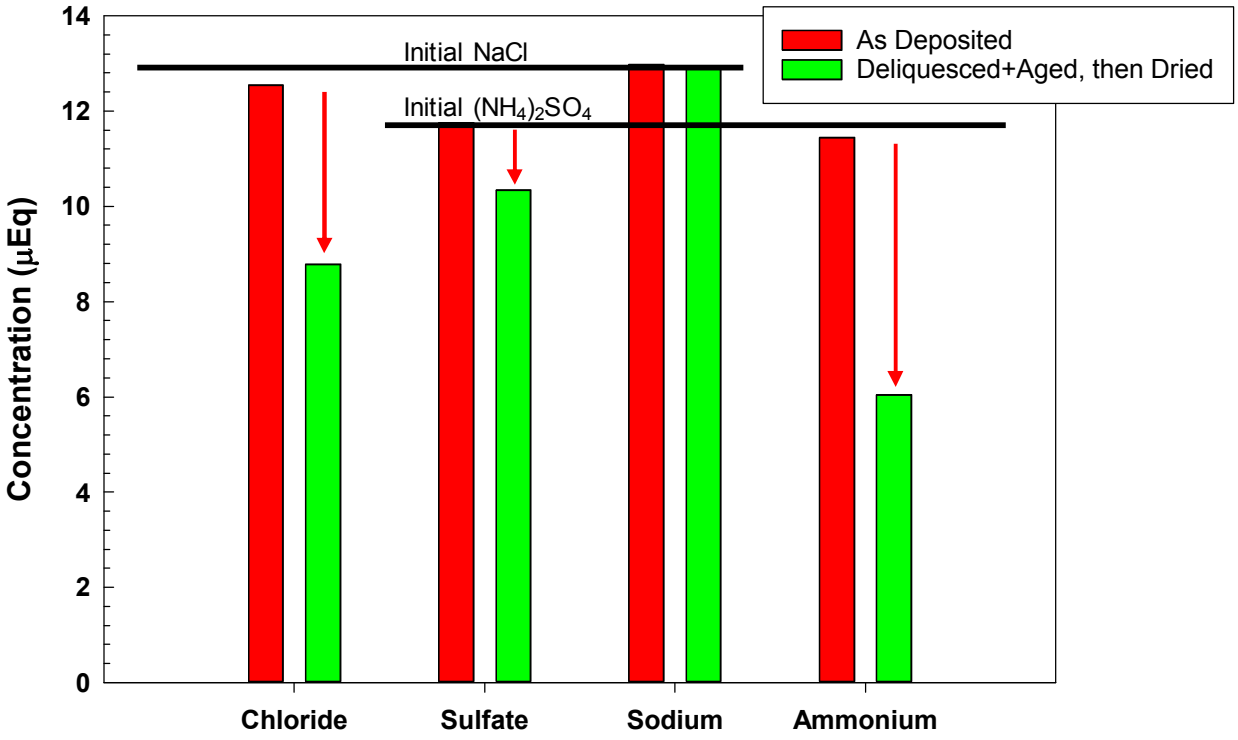

Figure 22. Bar graph showing ion concentrations in the control and treated samples in micro-equivalents. Results indicate that NH_4, HCl, and H_2SO_4 were lost by degassing over the period the salts were deliquesced.

3.3 Conclusions: Salt/Brine Stability Experiments

If FY 15, experiments evaluated the stability of dry and deliquesced ammonium salts, including NH_4Cl and NH_4NO_3, and $(NH_4)_2SO_4$. The experiments showed that solid NH_4Cl and NH_4NO_3 decomposed rapidly at even slightly elevated temperatures (30-50ºC), degassing ammonia (NH_3) and a mineral acid (HCl or HNO_3), and could not possibly accumulate on a heated canister surface. Similarly, once the salts deliquesced, the brines would degas rapidly. However preliminary data showed that $(NH_4)_2SO_4$ would not degas in the solid or deliquesced state. Experiments in FY16 confirmed that $(NH_4)_2SO_4$ would not degas at moderately elevated temperatures. $(NH_4)_2SO_4$ is a major component of many inland aerosols and because it is thermally stable, it could potentially accumulate on canister surfaces during storage.

NaCl is also thermally stable and could potentially accumulate, resulting in an assemblage of $(NH_4)_2SO_4$/NaCl on the canister surface. In FY15, we hypothesized that this salt mixture, even if stable it the dry state, would form a deliquescent brine that would not be stable, but that would instead degas NH_3 and HCl, precipitating Na_2SO_4 until either ammonium or chloride was completely consumed. In FY15, this theory was tested, and it was confirmed that the brine is not stable, and cannot persist on even a slightly heated canister surface. NH_4 is the most abundant cation in inland aerosols, and SO_4 is the most abundant anion; at inland ISFSI sites, it is likely that once the salts deliquesce, chloride, if deposited incidentally from cooling tower emissions or nearby road salting, will be depleted by degassing prior to ammonium. Because chloride is a major risk factor for stress corrosion cracking, these data suggest that the risk at inland sites may be significantly less than previously thought.

4. ANALYSIS OF DUST SAMPLES COLLECTED FROM AN IN-SERVICE CANISTER STORAGE SYSTEM AT THE MAINE YANKEE NUCLEAR STORAGE SITE

Charles Bryan and David Enos, Sandia National Laboratories

In July, 2016, the Electric Power Research Institute (EPRI) and industry partners performed a field test at the Maine Yankee Nuclear Site, located near Wiscasset, Maine. The primary goal of the field test was to evaluate the use of robots in surveying the surface of in-service an interim storage canister within an overpack; however, as part of the demonstration, dust and soluble salt samples were collected from several surfaces within the interim storage system. The storage system is a vertical canister system made by NAC International, consisting of a steel-lined concrete overpack containing a 304 stainless steel (SS) welded storage canister. The surfaces that were sampled for deposits included the top of the shield plug, the side of the canister, and a shelf at the bottom of the overpack, just below the level of the pillar on which the canister sits (**Figure 23**). The robot that sampled the dust entered through the rectangular channels that form the inlet vents, which provide a direct pathway to an open space near the canister pedestal, below the canister. The robot then moved up and outward through rectangular openings in the circular ring that helps support the canister, into the annulus and onto the shelf from which the dust was sampled.

The canister did not contain spent fuel but rather Greater-Than-Class-C (GTCC) waste, which did not generate significant heat, limiting airflow through the storage system. The canister had been in service for over 14 years when the sampling occurred. Dust on the shelf and on the shield plug may have entered through the inlet vents, but also could have been blown into the outlet vents near the top of the overpack, as there was little or no thermally-driven air flow out of the vents. It should be noted that the amounts, and potentially even the composition, of deposited dusts on this unheated canister may not be relevant to canisters containing heat-generating waste at the site.

Because the primary goal of the field test was to evaluate the use of robots in surveying the surface of the canister within the overpack; collection of dust samples was carried out in a qualitative fashion, using paper filters and sponges as the sampling media. Two filters were used to collect dust by hand on the shield plug that rested on top of the canister. Using the robot, one sponge sample was taken from the side of the canister, and five sponges samples were taken from a shelf near the bottom of the overpack. The sampling focused mostly on determining the composition of soluble salts present in the dust. It was anticipated that a wet substrate would more effectively extract soluble salts from the surface that was sampled, so both the sponges and the filter paper were wetted with demineralized water prior to being applied to the surface of the metal. Sampling was accomplished by simply pressing the damp substrate against the metal surface for two minutes, and then removing it. It is unlikely that the sampling method quantitatively collected dust or salts from the metal surface; however, both substrates did extract a significant amount of material. The paper filters collected particles trapped within the cellulose fibers of the filter and salts dissolved in the moisture in the filter, while the sponges collected only the soluble salts, with very few particles.

Upon delivery to Sandia, the samples were photographed, and then the soluble salts were leached from the substrates with deionized water and analyzed for anions and cations via ion chromatography (IC). The insoluble minerals on the filters, and those that were dislodged from the sponges during rinsing, were analyzed by scanning electron microscopy (SEM) and energy dispersive X-ray spectroscopy (EDS).

Sampling and analytical methods, and a list of the samples collected, are provided in Section 3.1 of this report. Section 3.2 summarizes the results of the SEM/EDS and chemical analyses, and Section 3.3 provides conclusions.

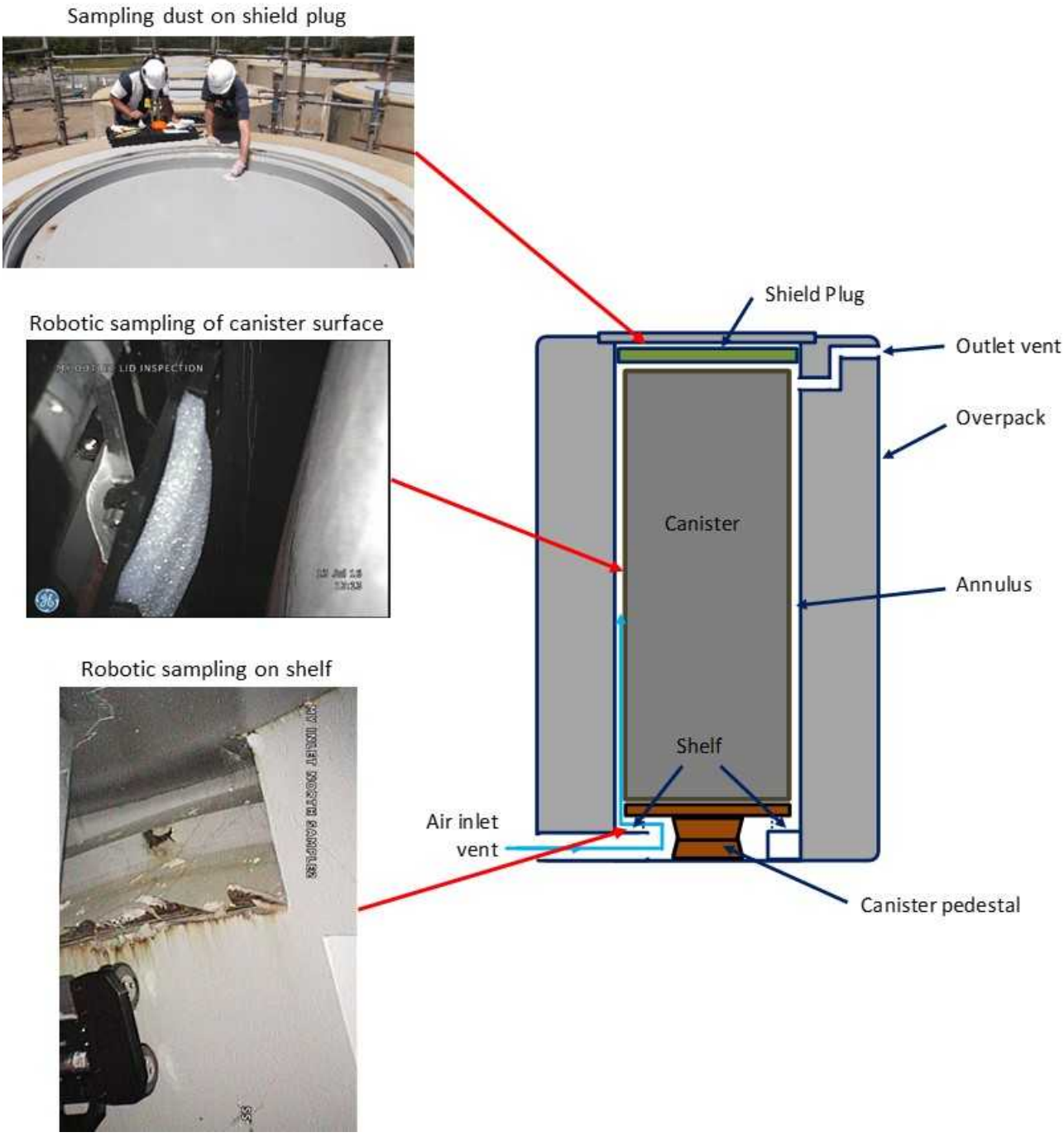

Figure 23. Storage system design (upper), and a close-up of the lower plate of the overpack (lower).

The demonstration at Maine Yankee has shown that the robot and sampling method used for the test can successfully be used to collect soluble salts from metal surfaces within an interim storage system overpack. As discussed below, the results were consistent from sample to sample, suggesting that a representative sample of the soluble salts was being collected. However, it is unlikely that the salt samples collected here represent quantitative sampling of the salts on the surfaces evaluated. It should also be noted that the relevance to storage systems at the site that contain SNF may be limited, because a heat-generating canister will result in greater airflow through the overpack, affecting dust deposition rates and possibly salt compositions.

4.1 Samples and Methods

4.1.1 Samples

Two types of samples were collected from the in-service dry storage system at the Maine Yankee Nuclear Facility. The first type consisted of damp 4.5 cm diameter Whatman #41 filter paper, which is ashless and contains virtually no soluble components. The filter paper was used to collect dust samples by hand from accessible surfaces in the dry storage system. The second type of sample consisted of damp polyurethane sponge material made by Truclean ®, which was pressed against metal surfaces in the storage system to leach off the soluble salts. The sponge samples were taken robotically from areas that were not accessible to hand sampling. The filter samples were collected by hand from the shield plug on top of the canister. The sponge samples were collected from the canister surface and from a shelf in the overpack, just above the inlet vents, using a robot with magnetic wheels.

Following collection, the samples were shipped to SNL for analysis. Eight samples were delivered (Table 4); two moist filter samples that had been collected from the shield plug, one sponge sample from the canister surface, and five sponge samples that had been collected from the overpack itself. The filter samples had a heavy visible dust load; of the sponges, only one sample (#8) had more than a few grains of coarse sand-sized dust on the surface. Solid particles that washed off the sponges during the rinsing process were retained for later examination. These were mostly sand-sized materials; however, in several samples, one or two large white or grey flaky aggregates were also present; these had usually fallen off of the sponges, and remained in the jars. Unlike the sponges, the dust solids on the filter paper samples did not rinse off, but were trapped in the fibers of the paper and were retained on the paper. The filters with the trapped dust particles and the insoluble dust particles from the sponges were kept for later imaging and analysis by SEM/EDS analysis.

Sponge blanks were not delivered with the original samples, but were provided upon request, several weeks after the initial samples were delivered. EPRI and their team shipped 6 sponge samples to Sandia for use as blanks. Three of these had been cut and rinsed in preparation for the sampling on 7/13/2016; the other three had been freshly cut and rinsed following the same procedure as the original sponges. The second set was included in case sponge degradation in the interval (perhaps due to oxidation of the freshly cut surfaces, or possibly biodegradation if the sponges were still damp during storage) increased the leachable salt content.

Table 4. Dust Samples Collected from a Dry Storage System at the Maine Yankee Nuclear Facility.

Sample #	Type	Description
1	Filter paper	Shield Plug #3 7/11/16
2	Filter paper	Shield Plug #4 7/11/16
3	Sponge	VCC2, South Outlet Vent, TSC-CS Contamination 7/13/16 (Sample from the canister surface)
4	Sponge	VCC2, Northwest Inlet Vent, North side shelf 7/13/16
5	Sponge	VCC2, Northwest Inlet Vent, West side shelf 7/13/16
6	Sponge	VCC2, Southeast Inlet Vent, East side shelf close to vent 7/13/16
7	Sponge	VCC2, Southeast Inlet Vent, South side shelf 7/13/16
8	Sponge	VCC2, Southeast Inlet Vent, South side shelf close to vent, attempted ~0.8" movement (one way) 7/13/16
Blanks		
7/13/2016-1	Sponge	Blank sample
7/13/2016-2	Sponge	Blank sample
7/13/2016-3	Sponge	Blank sample
8/2/2016-1	Sponge	Blank sample
8/2/2016-2	Sponge	Blank sample
8/2/2016-3	Sponge	Blank sample
Demin. water	Water	Water used to wet the sampling media prior to dust collection

4.1.2 Methods

The following methods and equipment were used to characterize the samples from Maine Yankee:

- *SEM imaging and EDS element mapping*. SEM/EDS analysis of the insoluble dust residues provided textural and mineralogical information on the insoluble phases, and allowed visual identification of organic matter (floral/faunal fragments).
- *Chemical analyses of the soluble salts in the dust.* Soluble salts were leached from the filters and sponges and analyzed to determine their concentration and composition.

SEM Imaging and EDS Analysis

SEM/EDS analysis of the samples provides textural and mineralogical information of the insoluble dust residues, and allows visual identification of organic matter (floral/faunal fragments). Sample fractions retained for SEM analysis were coated with carbon to reduce sample charging during analysis. Imaging and element mapping was done with a Tescan Vega3 SEM, equipped with an EDAX Element® EDS detector. An accelerating voltage of 15 keV was used, and working distances of 9 to 12 mm, with varying degrees of magnification. Images were obtained using both secondary and backscattered electron imaging, and a beam current of 100-200 pA. A somewhat higher beam current (1 nA) was used to produce a high count rate during EDS analysis and to facilitate rapid element mapping. However, the elevated beam current did enhance sample charging, resulting lower image quality in some cases.

Chemical Analysis

After small fractions of the filters were removed for SEM analysis, the filters and sponges were leached in a known volume of deionized water to extract the soluble salts. Sponge blanks received from EPRI were

similarly leached to determine background salt compositions and concentrations. The solutions were filtered through 0.45 µm syringe filters and 5 ml aliquots were immediately transferred to sample vials for analysis by IC. All sponge samples and blanks were then dried and weighed to determine sample mass, so that blanks could be appropriately subtracted, as the cut sponge pieces used in sample collection varied in size and weight.

Soluble salt compositions were determined by ion IC analysis. Anionic analytes were F^-, Cl^-, Br^-, NO_2^-, NO_3^-, SO_4^{-2}, and PO_4^{-3}; however, Br^- and NO_2^- were never detected, and are not included here. Cationic analytes were Li^+, Na^+, NH_4^+, K^+, Mg^{2+}, and Ca^{2+}. For detailed analytical procedures, see Bryan and Enos (2016).

4.2 Results

4.2.1 SEM/EDS Analysis of Insoluble Mineral Residue

SEM/EDS analysis of the insoluble dust residues was carried out to determine the composition and morphology of the insoluble materials. Analyzed samples include small pieces cut from both of the filter samples, which had abundant large (sand-sized) dust particles trapped in the fibers, and a single SEM mount of particles that had dislodged from the sponges during leaching to extract the soluble salts. Results are summarized here with typical images from samples; a complete suite of analyses is provided in Bryan and Enos (2016), and allows the reader to better assess the representativeness of the results provided here.

4.2.1.1 Filter Samples

The insoluble mineral grains on the two filter samples were not dislodged during the leaching to extract soluble salts, because they were entangled by the fibers of the filter. After leaching, the filters were dried and sections were cut for SEM/EDS analysis. The minerals on the filters were mostly coarse, sand-sized grains, visible to the naked eye. The minerals are identical on both filters. **Figure 24** is a backscattered electron (BSE) SEM image of minerals on Sample #1. In BSE images, the relative brightness of the different phases present indicates the average atomic number (Z). The filter fibers are mostly carbon and oxygen, with a low average Z, and are dark gray; the minerals comprise mostly angular quartz grains (Si, O) (grey) and platy flakes of biotite (Si, Al, Fe, K, Mg, O) (pale grey). A few spherical, bright grains of iron oxide are also present in **Figure 24**. Iron oxide spheres are common in dusts, and here, may represent fly ash. In some storage canister dusts that have been sampled (Bryan and Enos 2014, 2015b), similar spheres represent welding condensate or spatter and contain Ni or Cr, but the lack of Cr and Ni indicate that the spheres here were probably derived from fly ash. Other terrigenous minerals such as potassium feldspar (K-Al-Si-O) are present in much smaller amounts. A single several millimeter fiber of plant matter was also observed. No salt phases were observed, but the samples were leached with deionized water prior to SEM analysis, so the lack of soluble minerals was expected. **Figure 25** shows minerals on Sample #2, which match those observed on Sample #1.

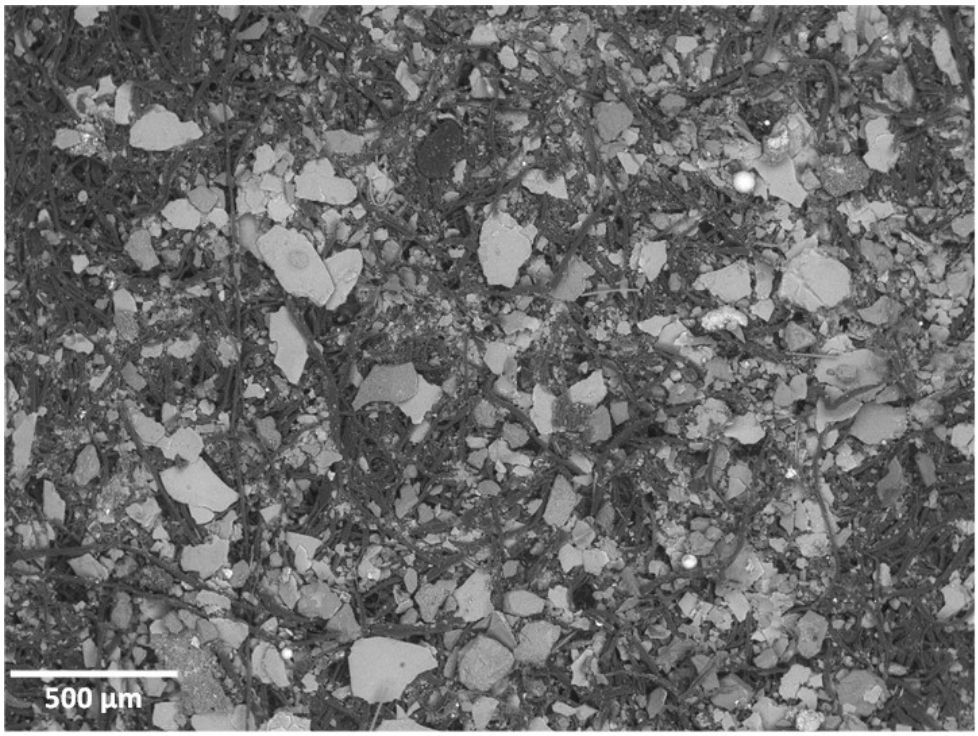

Figure 24. SEM BSE image of mineral grains embedded in the Sample #1 filter from the shield plug. Platy biotite flakes (pale gray); angular quartz grains (darker gray).

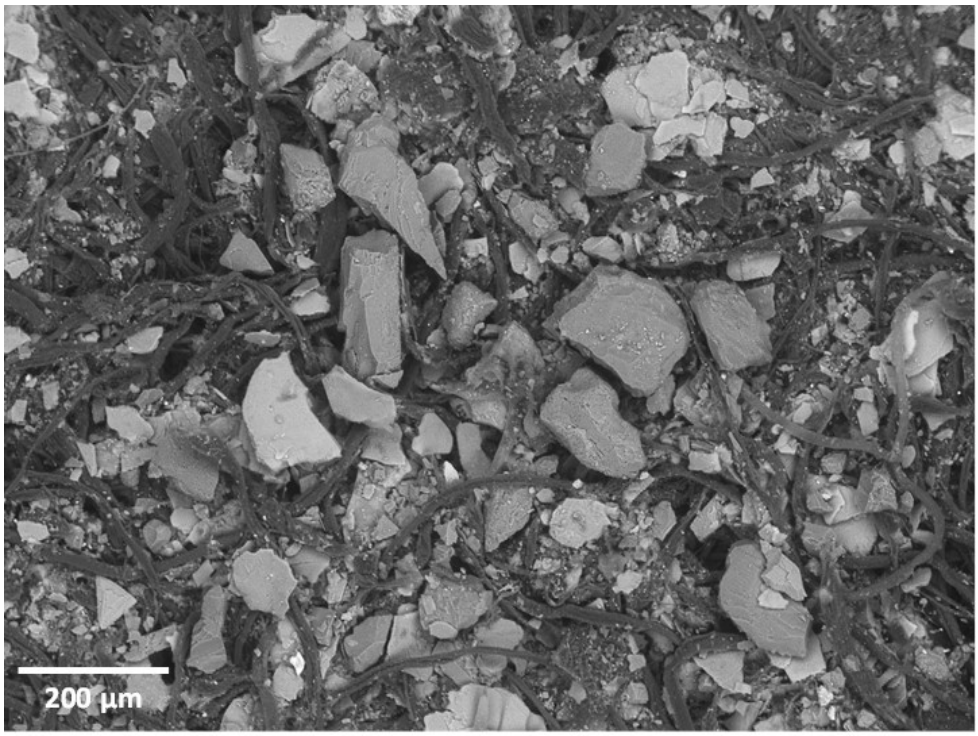

Figure 25. SEM BSE image of mineral grains embedded in the Sample #2 filter from the shield plug. Platy biotite flakes (pale gray); angular quartz grains (darker gray).

4.2.1.2 Insoluble Particles from the Sponges

In most cases, only a few sand-sized mineral grains were present on the sponge samples, and they dislodged during rinsing. The particles were collected and placed on carbon tape for analysis by SEM/EDS; the grains matched those observed on the filter samples, consisting mostly of biotite, with some quartz and iron oxide grains (**Figure 26**). However, a few larger grains were also present, up to a few mm in diameter. These were mostly dislodged during transportation and were recovered from the jars in which the sponges were shipped. These larger grains had a distinctive morphology, consisting of platy sheets of well-developed crystals with a flat bottom (See **Figure 27** and **Figure 28**). The individual crystals display several forms, including dodecahedrons and trigonal prisms. EDS X-ray analysis determined that the plates consist of calcium carbonate, calcium (aluminum) silicate, or a mixture of both. There can be little doubt that these plates represent efflorescence that formed by evaporation of concrete pore fluids. The well-formed crystals indicate that these crystals formed on an open surface, and given the very flat, even bottom, they probably represent efflorescence that formed on the steel inner surfaces of the overpack by concrete fluids seeping through gaps in the steel shell. Such efflorescence was observed in abundance during the canister inspection, as white stains and crusts on the inner surfaces of the overpack (**Figure 29**), which apparently formed by concrete fluids seeping out between joints in the metal shell (Fales, 2016). The particles may have flaked off the metal and accumulated on the shelf in the overpack, or may have brushed off onto the sponges as the robot was retrieved through the overpack vents.

Figure 26. SEM SE image and element maps of mineral grains dislodged from the sponge samples collected from the overpack shelf. Minerals are dominantly biotite, with some quartz and iron oxide.

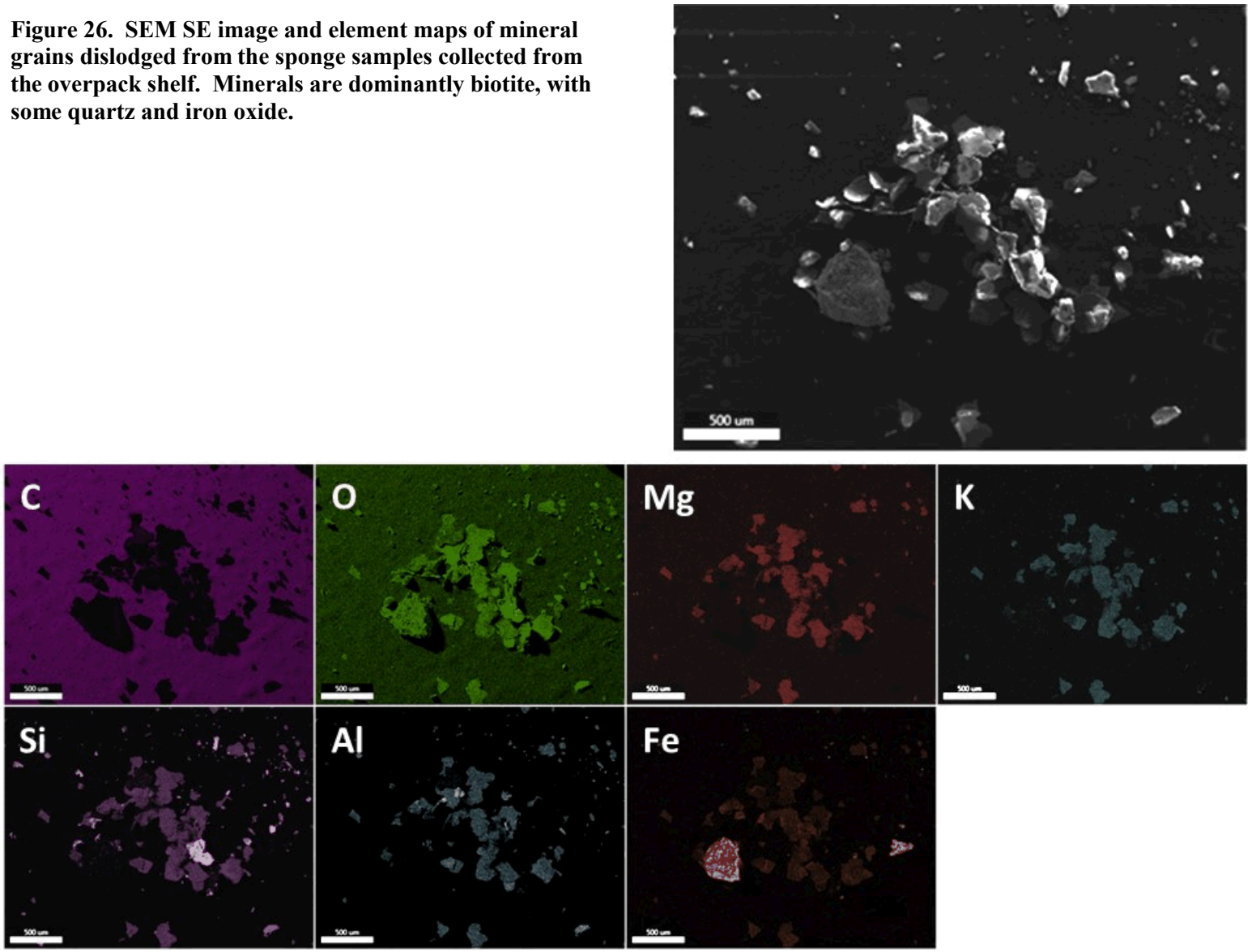

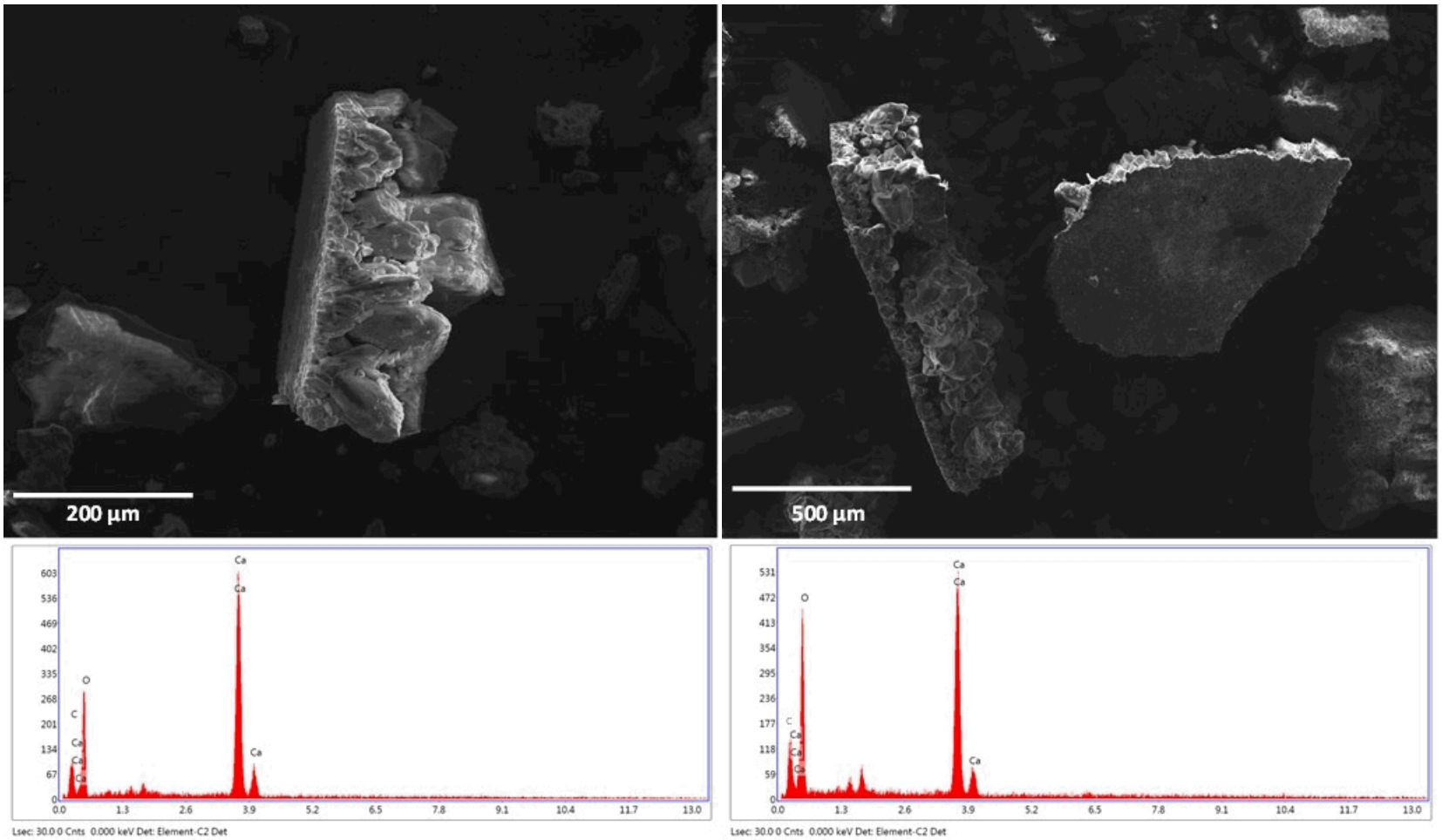

Figure 27. SEM SE images and EDS spectra of calcite plates found in the sponge insoluble residues from the overpack shelf.

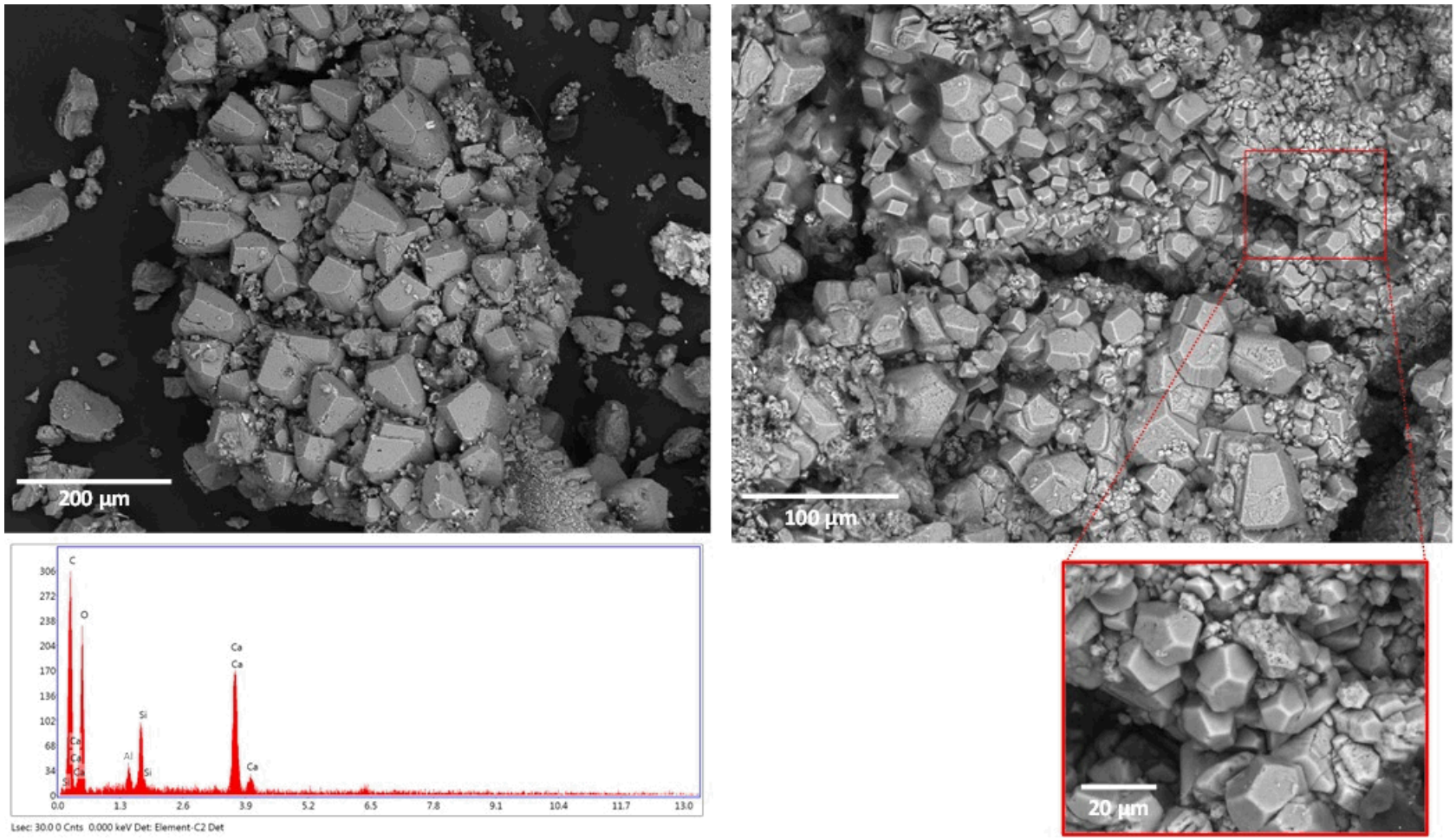

Figure 28. SEM SE images and an EDS X-ray spectrum of well-crystallized calcium aluminum silicate in the sponge insoluble residues samples from the overpack shelf.

Figure 29. Video image of white crusts of cementitious material on the inner surface of the overpack, located near an outlet vent.

4.2.1.3 Summary of SEM/EDS Analyses

To summarize, the insoluble residues retained by the filters and those dislodged from the sponges after rinsing were analyzed by SEM/EDS. In general, the dust particles were quite coarse, in the range of tens to hundreds of microns in diameter, in the sand-sized range. The grains are mostly terrestrial in origin, and are dominated by biotite flakes, perhaps 2/3 of the total, and angular quartz grains, about 1/3. Other detrital terrestrial minerals are also present in small amounts, as well as iron oxide spheres, probably derived from fly ash. A few large plates (up to a few mm) of well crystallized calcite and calcium (aluminum) silicate are present and represent efflorescence formed by concrete or cement pore fluids that crystallized on the inner metallic surface of the overpack. Such efflorescence was observed in abundance during the canister inspection, as white stains and crusts on the inner surfaces of the overpack, which apparently formed by concrete fluids seeping out between joints in the metal shell (Fales, 2016).

4.2.2 Chemical Analysis of Soluble Salts

The actual samples collected from the interim storage system were collected on 7/13/16, and delivered to Sandia on 7/15/16, but blank samples were not included. Sponge blanks were supplied upon request afterwards. Two sets of blanks were sent. The first set consisted of blank sponges that were rinsed and prepared with the actual samples on 7/13/16, but never used. The second set of blanks consisted of sponges that were prepared in an identical manner, but just prior to being sent to Sandia on 8/2/16. Two sets were provided so that it was possible to evaluate whether ageing of the sponges after cutting had any effect on the leachable salt load. No blanks were sent for the Whatman#41 filters; however, the filters are "ashless" meaning that they are nearly pure cellulose and contain virtually no inorganic materials. Previous analyses have shown that they contain no measurable soluble salts.

The soluble ion concentrations in the sponge blanks, in µg/sample, are shown in **Table 5**. Values shown in italicized gray type had clear IC peaks, but fell between the lowest standard and the blank, and are semi-quantitative. Measurement uncertainties are generally 5% or less, but may be as high as 20% for low values, near the quantitation limit. There is a significant difference between the 7/13/16 set of blanks and the 8/2/16 set of blanks; the 7/13/16 blanks had significantly higher leachable salts. This may indicate that the leachable salt content does increase with ageing; alternatively, perhaps the 7/13/16 blank sponges were simply not rinsed as thoroughly as the 8/2/16 blank samples. When compared to the

soluble salt concentrations in the samples, the soluble salt concentrations in all of the blanks were very low, sufficiently low that the potential contribution of soluble salts from the sponges can be ignored. The blanks will not be considered further.

The soluble ion concentrations in the samples are shown in **Table 6** (see **Table 4** for a full description of each sample). The soluble salt concentrations of both the filter samples the shield plug and sponge samples from the overpack shelf were sufficiently high to be easily measured. Although the soluble salt concentrations leached from the filters and sponges were more or less commensurate, the compositions differed significantly. In both sets of samples, the cations are dominantly Ca and Na, with moderate levels of K and minor Mg. However, the shield plug samples are sulfate- and chloride-rich, with minor NO_3; the overpack shelf samples and the canister sample are NO_3-rich, with moderate Cl but very little SO_4. Ammonium was not observed on any of the samples; however, there are several possible explanations for this. The absence of ammonium is consistent with experimental evidence that it does not persist in the presence of nitrate or chloride, because it is lost from the surface via a coupled degassing reaction (Bryan and Enos, 2015a; Bryan and Enos, 2015b; Enos and Bryan, 2016b). Moreover, if unreacted cement phases were present in the dust and in contact with the deliquesced salts, then the resulting high pH would have promoted conversion of NH_4^+ to NH_3, further driving degassing. Finally, ammonium may have been lost by degassing from the moist sampling media during sample storage and transportation.

The salt concentrations in micro-equivalents (µEq) per sample are provided in **Table 7**. The number of µEq is equal to the number of µmoles multiplied by the charge of the ionic species; this eliminates the effect of different masses for the ionic species, providing a clearer understanding of the relative importance of each species with respect to the total ion load.

The charge balance error is calculated from the total cationic and anionic µEq present using:

$$Charge\ balance\ error, \% = \frac{(Sum\ of\ cations - Sum\ of\ anions)}{(Sum\ of\ cations + Sum\ of\ anions)} \times 100$$

As has been previously observed for soluble salt analyses at Calvert Cliffs, Hope Creek, and Diablo Canyon (Enos et al., 2013; Bryan and Enos, 2014; EPRI, 2014; Bryan and Enos, 2015b), the charge balance is poor; measured anion µEq are much less than cation µEq. This has previously been attributed to carbonate species, both because carbonate cannot be measured in the IC analyses, and because carbonates have been commonly observed in SEM analyses of the dusts (Enos et al., 2013; Bryan and Enos, 2014; EPRI, 2014; Bryan and Enos, 2015b). Calcium carbonate in the form of cement efflorescence was observed in the insoluble dust residues, so carbonate is also likely to be responsible for the charge imbalance in the Maine Yankee samples.

The salt compositions from both sampled locations suggest that the soluble salts are a combination of both sea-salts (rich in Na, Cl, and Mg), and salts derived from continental sources, rich in NH_4, K, Ca, NO_3, and SO_4, although NH_4 was not observed here. It is reasonable to assume that most of the chloride was deposited as sea-salts; however, chloride is deficient relative to Na. If the chloride was deposited as sea-salts, then the salt particles partially underwent particle-gas conversion reactions prior to or after deposition. Such reactions have been discussed before (Bryan and Enos, 2015a), and convert chloride-rich sea-salts to nitrate and sulfate minerals. By reducing the chloride load on the canister surface, these reactions reduce the risk of canister SCC.

Table 5. Soluble Ion Concentrations in Sponge Blanks, µg/sample.

Sample #	Na^+	NH_4^+	K^+	Mg^{2+}	Ca^{2+}	F^-	Cl^-	NO_3^-	SO_4^{2-}	Sum, µg
7/13/16-1	2.3	n.d.	1.4	*0.1*	9.8	n.d.	*1.8*	6.2	n.d.	21.5
7/13/16-2	3.6	n.d.	1.8	*0.1*	11.0	n.d.	4.3	9.9	n.d.	30.7
7/13/16-3	2.3	n.d.	1.7	n.d.	8.8	n.d.	*2.0*	10.6	*1.4*	26.7
8/2/16-1	*1.1*	n.d.	*0.5*	n.d.	*3.1*	n.d.	*2.7*	3.7	n.d.	11.0
8/2/16-2	*1.1*	n.d.	*0.3*	n.d.	*1.6*	n.d.	*2.4*	*0.4*	n.d.	5.8
8/2/16-3	*1.6*	n.d.	*0.4*	n.d.	*2.9*	n.d.	3.8	*2.0*	n.d.	10.7

Note: Values shown in italicized gray type had clear IC peaks, but fell between the lowest standard and the blank and are semi-quantitative.

Table 6. Soluble Ion Concentrations in Maine Yankee Dust Samples, µg/sample.

Sample #	Na^+	NH_4^+	K^+	Mg^{2+}	Ca^{2+}	F^-	Cl^-	NO_3^-	SO_4^{2-}	Sum, µg
1 (filter) shield plug	86.6	0.1	34.2	12.2	66.1	0.7	84.0	8.7	179	472
2 (filter) shield plug	60.2	n.d.	13.8	6.4	52.7	0.6	48.6	3.2	102	287
3 (sponge) canister	80.9	0.6	26.6	2.2	50.7	n.d.	42.9	167	6.0	377
4 (sponge) overpack shelf	65.7	*0.1*	24.4	2.7	60.4	*0.2*	19.2	188	10.9	371
5 (sponge) overpack shelf	63.6	*0.1*	24.6	2.5	67.8	*0.3*	18.0	178	15.1	370
6 (sponge) overpack shelf	60.6	0.2	22.3	2.5	57.2	n.d.	14.8	171	11.8	340
7 (sponge) overpack shelf	93.4	0.2	48.0	4.2	97.5	n.d.	42.4	343	15.5	644
8 (sponge) overpack shelf	80.7	0.4	61.4	4.3	111.8	n.d.	28.7	166	15.6	469

Note: Values shown in italicized gray type had clear IC peaks, but fell between the lowest standard and the blank, and are semi-quantitative.

Table 7. Soluble Salt Concentrations in Maine Yankee Dust Samples, µEq/sample.

Sample #	Na^+	NH_4^+	K^+	Mg^{2+}	Ca^{2+}	F^-	Cl^-	NO_3^-	SO_4^{2-}	Sum cat.	Sum an.	CBE, %
1 (filter) shield plug	3.77	0.01	0.87	1.00	3.30	0.03	2.37	0.14	3.73	8.95	6.27	17.6
2 (filter) shield plug	2.62	n.d.	0.35	0.53	2.63	0.03	1.37	0.05	2.12	6.13	3.57	26.3
3 (sponge) canister	3.52	0.03	0.68	0.19	2.53	n.d.	1.21	2.69	0.13	6.95	4.03	26.6
4 (sponge) overpack shelf	2.86	*0.01*	0.62	0.22	3.01	*0.01*	0.54	3.02	0.23	6.73	3.81	27.7
5 (sponge) overpack shelf	2.76	*0.01*	0.63	0.21	3.38	*0.01*	0.51	2.87	0.31	6.99	3.70	30.8
6 (sponge) overpack shelf	2.63	0.01	0.57	0.21	2.86	n.d.	0.42	2.76	0.25	6.28	3.42	29.5
7 (sponge) overpack shelf	4.06	0.01	1.23	0.34	4.86	n.d.	1.20	5.53	0.32	10.51	7.05	19.7
8 (sponge) overpack shelf	3.51	0.02	1.57	0.35	5.58	n.d.	0.81	2.68	0.32	11.03	3.82	48.6

Notes: Values shown in italicized gray type had clear IC peaks, but fell between the lowest standard and the blank, and are semi-quantitative.
CBE = charge balance error, %.

4.3 Conclusions: Maine Yankee Dust Samples

In July, 2016, the Electric Power Research Institute and industry partners performed a field test at the Maine Yankee Nuclear Site. The primary goal of the field test was to evaluate the use of robots in surveying the surface of an in-service interim storage canister within an overpack; however, as part of the demonstration, dust and soluble salt samples were collected from surfaces within the interim storage system. The storage system is a vertical canister system made by NAC International, consisting of a steel-lined concrete overpack containing a 304 SS welded canister. The canister did not contain spent fuel but rather non-heat generating GTCC waste. The surfaces that were sampled for deposits included the top of the shield plug; a shelf at the bottom of the overpack, just below the level of the top of the pillar on which the canister sits; and the vertical side of the canister itself. The samples were sent to Sandia National Laboratories for analysis.

Because the primary goal of the field test was to evaluate the use of robots in surveying the surface of the canister within the overpack; collection of dust samples was carried out in a qualitative fashion, using paper filters and sponges as the sampling media. The sampling focused mostly on determining the composition of soluble salts present in the dust. It was anticipated that a wet substrate would more effectively extract soluble salts from the surface that was sampled, so both the sponges and the filter paper were wetted prior to being applied to the surface of the metal. Sampling was accomplished by simply pressing the damp substrate against the metal surface for two minutes, and then removing it. It is unlikely that the sampling method quantitatively collected dust or salts from the metal surface; however, both substrates did extract a significant amount of material. The paper filters collected both particles, trapped within the cellulose fibers of the filter, and salts, while the sponges collected only the soluble salts, with very few particles.

Upon delivery to Sandia, the soluble salts were leached from the substrates and analyzed via ion chromatography, and insoluble minerals were analyzed by SEM/EDS. The insoluble minerals were found to consist largely of terrestrially-derived mineral fragments, dominantly biotite and quartz. Large aggregates (up to a few mm) calcium carbonate, calcium silicate, and/or calcium aluminum silicate were also present. These had one flat surface and one well crystallized surface, and were interpreted to be efflorescence on the inside of the overpack and in the vent, formed by seepage of cement pore fluids through joints in the steel liner of the overpack. The material may have flaked off and fallen to the point where the dust was collected, or may have brushed off onto the sponges when the robot was retrieved through the inlet vent.

Chemical analysis showed that the soluble salts on the shield plug were Ca- and Na-rich, with lesser K and minor Mg; the anionic component was dominated by SO_4 and Cl, with minor amounts of NO_3. The cation compositions of the soluble salts from the overpack shelf were compositionally similar to the shield plug samples, but the anions differed significantly, being dominantly NO_3 with lesser Cl and only trace SO_4. The sample from the canister surface was similar to those from the overpack shelf, with only minor sulfate. The salts appear to represent a mixture of sea-salts (probably partially converted to nitrates and sulfates by particle-gas conversion reactions) and continental salt aerosols. Ammonium, a common component in continental aerosols, was not observed and may have been lost by degassing from the canister surface, or after collection during sample storage and transportation.

The demonstration at Maine Yankee has shown that the robot and sampling method used for the test can successfully be used to collect soluble salts from metal surfaces within an interim storage system overpack. However, it is unlikely that the salt samples collected represent quantitative sampling of the salts on the surfaces evaluated; for that reason, chloride densities per unit area are not presented here. It should also be noted that the relevance to storage systems at the site that contain SNF may be limited, because a heat-generating canister will result in greater airflow through the overpack, affecting dust deposition rates and possibly salt compositions.

5. ANALYSIS OF CORROSION RESIDUES FROM THE HIGH BURNUP DEM0ONSTRATON CASK

Charles Bryan, Sandia National Laboratories

This report documents the results of analyses of corrosion residues found within the cask that will be used for the high-burnup demonstration (HBU) project when it was opened for inspection after several years in storage. The TN-32B cask was fabricated by Precision Custom Components of York, Pennsylvania in April, 2004 and was stored there until May, 2015, when it was shipped to Columbiana Hi Tech LLC in Greensboro, North Carolina to be modified for the HBU test. On September 29-30, 2015, a team consisting of EPRI personnel, AREVA personnel (AREVA Federal Services, AREVA TN, and AREVA P&T), and personnel from Dominion Engineering Virginia Power performed an inspection of the cask. As part of the inspection, the cask was opened and the interior components surveyed. During this survey, polyethylene-wrapped wooden cribbing that had been placed within the cask over 11 years earlier to prevent shifting of the basket during transport was removed, revealing two small areas of brown-and-white residue on the aluminum basket rails. These areas are shown in **Figure 30** and in **Figure 31**. The residue appeared to be a corrosion residue, and although it was likely that this was somehow caused by contact with the wooden cribbing, there was some concern that it could have been caused by some contaminant on the metal itself, and that it could occur elsewhere within the cask, where it would not be as readily observed. To test this, the decision was made to collect samples of the suspected corrosion residue the next time the cask was opened. In July, 2016 the cask was opened for a fit-up test, and the samples were collected. The samples were sent to SNL for analysis. Also during this test, a boroscope was lowered though the basket to the bottom of the canister, to look for further evidence of corrosion.

The material sent to SNL for analysis consisted of a single bulk sample of the filamentous spongy residue, and several samples collected by swiping the residues at each of the two locations with 5-inch paper filters. At SNL, the samples were removed from their sample tubes and photographed. Then, subsamples were taken for imaging and textural analysis by SEM/EDS. Sub-samples were also analyzed by X-ray diffraction (XRD). Finally, the bulk of each sample was calcined (ashed), digested, and analyzed using inductively-coupled-plasma mass spectrometry (ICP-MS) to determine the elemental composition of the residue. This report documents the results of those analyses. The samples received by SNL and the analytical techniques used to analyze them are described in Section 5.1; Section 5.2 presents the results of the different analyses; and the results are discussed and interpreted in Section 5.3. Conclusions are provided in Section 5.4.

As discussed in the following sections, the residues consist largely of aluminum corrosion products, fungal material, and organic compounds. Insect fragments were also present in the samples collected. Trace element analyses indicate that the elements present in the residues are sourced to both the aluminum alloy and to degradation of the wood. Given evidence for fungal growth after the cask was sealed, it is concluded that the wooden cribbing was infested with fungi and possibly, with living insects as well, when it was placed in the cask. Several possible causes for the observed attack are considered, including crevice corrosion, oxic corrosion due to corrosive wood treatments potentially present in the cribbing, and corrosion due to organic compounds leached from the wood and produced by fungal action. Regardless of the mechanism, it is clear that corrosion of the aluminum metal was due to contact with the wooden cribbing. Once the cask has been thoroughly cleaned, further corrosion over the course of the high-burnup demonstration test is unlikely.

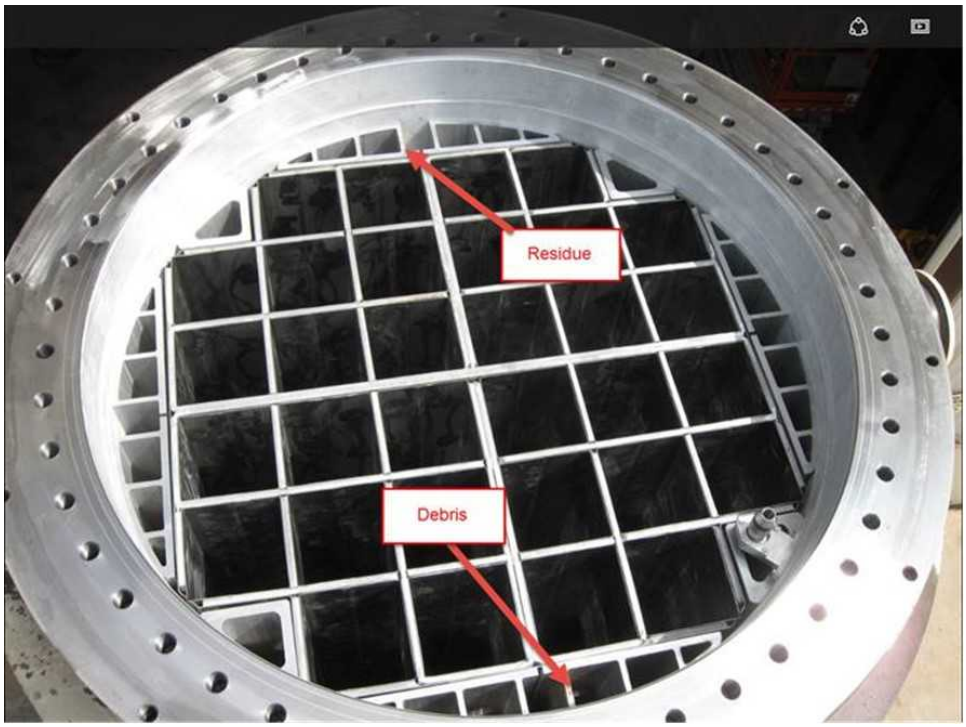

Figure 30. Photograph of the storage cask, with the lid removed. The locations of the two areas with apparent corrosion residue are shown.

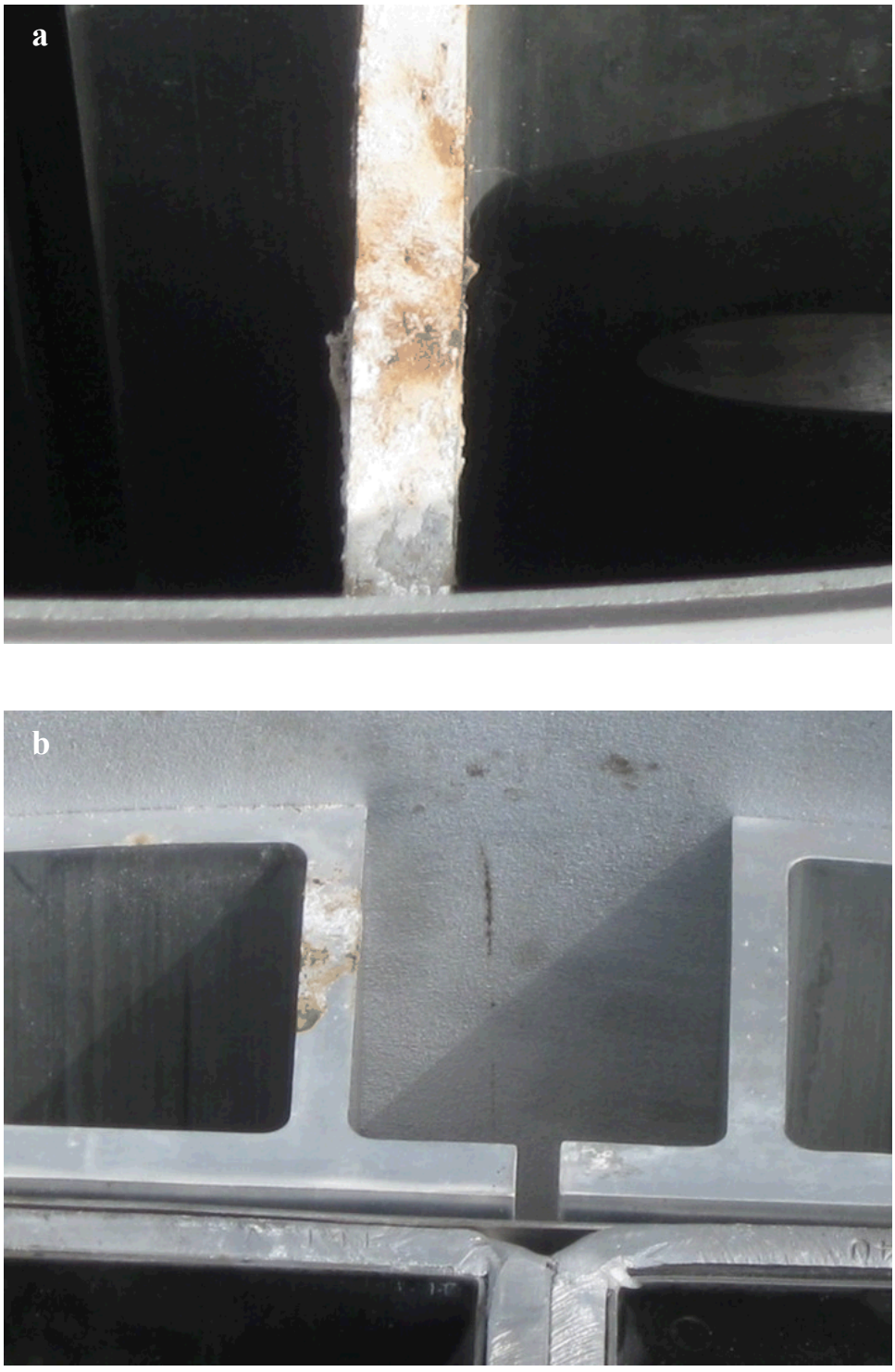

Figure 31. Photographs of a) the "debris" on the basket rail (near side), and b) the "residue" on the basket rail (far side).

5.1 Samples and Methods

5.1.1 Samples

Samples were collected from two locations on the aluminum basket rails, the "Debris" side, and the "Residue" side. The Debris side had finely fibrous mat of material that was partially detached from the surface (**Figure 31**a). The Residue side had a thin coating of material that was more strongly attached to the rail (**Figure 31**b). During sample collection, tweezers were used to collect a fragment of the loose debris from the Debris side. The material consisted of the fibrous base, with sand-sized grains attached and embedded in the fibrous material. The mat was stained brown in some areas, and the grains, although mostly white, were also stained in some areas. The debris sample was slightly over 1 cm in diameter. Following collection of the debris, swipes were taken of both sides, first a dry swipe, and then two wet swipes. The round 5" filters were folded and placed in 50 ml polypropylene sample vials for shipment to Sandia. Upon delivery to Sandia, the samples were photographed, and then a small piece of each was taken for SEM analysis. For chemical analysis, the two wet swipes from each location were combined, as there was no reason to analyze them individually. The samples are listed in **Table 8** below. The residue itself appeared to be a finely fibrous brown material, with white particles scattered across the top, and adhering to the fibers. The residue on the dry filters appeared to be a brown stain, finely granular. The residue on the damp filters was also a brown stain, but was more coarsely granular, with brown or white sand-sized grains.

Table 8. Corrosion Residue Samples from the High-burnup Demonstration Cask

Sample Description	Sample Type
Debris side – Debris	Loose debris
Debris side – Dry (dry swipe)	Filter paper
Debris side – Wet (wet swipe)	Filter paper
Debris side – Wet (2nd wet swipe)	Filter paper (two filters)
Residue side – Dry (dry swipe)	Filter paper
Residue side – Wet (wet swipe)	Filter paper
Residue side – Wet (2nd wet swipe)	Filter paper
Filter paper blank	Filter paper
Demineralized water blank (used to wet filters)	Aqueous solution

5.1.2 Methods

The following methods and equipment were used to characterize the samples from the high-burnup demonstration cask:

- *SEM imaging and EDS element mapping*. SEM/EDS analysis of the samples provides textural and mineralogical information of the corrosion residue, and allows visual identification of organic matter (floral/faunal fragments).
- *X-ray diffraction analysis.* XRD analysis identifies inorganic phases present, if crystalline.
- *Fourier Transform Infrared Spectroscopy (FTIR)/Raman analysis.* These complementary techniques provide information on the molecular bond structure of the materials analyzed, aiding in the identification of specific compounds.

- *Chemical analyses of the filter samples and corrosion residue.* Both the corrosion residue sample and the filter samples were calcined (ashed), digested, and analyzed by ICP-MS to determine bulk elemental composition of the residue.

SEM Imaging and EDS Analysis

SEM/EDS analysis of the samples provides textural and mineralogical information of corrosion residue components, and allows visual identification of organic matter (floral/faunal fragments). The analysis was carried out using the same equipment and techniques as was used for analysis of the Maine Yankee dust samples, described in Section 4.1.2 of this report, except that an accelerating voltage of 20kV was used, to improve detection of transition metal species.

XRD Analysis

XRD analysis was performed using a Bruker D2 Phaser diffractometer with a Cu Kα X-ray source, and a LynxEye solid-state energy discriminating X-ray detector. Analyzed samples consisted of grains extracted from one of the wet pads from the "residue" location, and loose grains associated with the "debris" sample. The grains were crushed in a mortar and pestle and then slurried onto a zero-background silicon wafer prior to analysis.

FTIR/Raman analysis

FTIR analysis was carried out using a Nicolet Nexus 870 FTIR instrument, with an optional Attenuated Total Reflectance "DurasamplIR" accessory. Components in the infrared spectra were identified by functional group analysis combined with comparison to a reference library of infrared spectra. Raman spectroscopy was carried out using a microscope-based Raman spectroscopy with a laser light source. Incorporating a microscope into the Raman system makes possible resolution and detection on the microscopic scale. For this analysis, individual grains of the corrosion product from both the "residue" location and the "debris" location were analyzed. The mineralogy of the grain was evaluated by comparison of the collected spectra to a reference library of Raman spectra.

Chemical Analysis

Following removal of small fragments for analysis by SEM/EDS and XRD, the wet filter samples from each sample location were combined for analysis. The samples were ashed in a furnace and digested using high-purity nitric and hydrofluoric acids. The samples were then then taken up in 15 ml 2% nitric acid for analysis by ICP-MS. After performing a semi-quantitative scan to determine what elements were present, calibration standards for quantitative analysis from were made from high-quality Perkin-Elmer ICP-MS stock solutions. The samples were then analyzed using a Perkin-Elmer NexION 350D ICP-MS, using the Standard, Collision, and Reaction modes for individual isotopes. For detailed analytical procedures, see Bryan and Enos (2016).

5.2 Results

5.2.1 SEM/EDS Analysis

SEM/EDS analysis of the samples was carried out to determine corrosion residue texture, bulk composition, and mineralogy. The samples are listed in **Table 8**, and those that were analyzed include a fragment of the debris; a piece of the dry filter pad with adhering brown material from the "debris" location; a piece of the dry pad from the "residue" location with adhering brown material; and loose grains extracted from the surface of the wet pad from the residue location. SEM images were taken of characteristic features and EDS element mapping was done to assess mineralogy and composition. Results are summarized here with typical images from the samples.

SEM images were taken both in BSE mode and in secondary electron (SE) mode. In BSE images, the relative brightness of the different phases present indicates the average atomic number (Z); materials with a higher average Z scatter more electrons, and appear brighter that materials with a lower average Z. SE

images emphasize texture over composition, and because they must be taken at high vacuum, charging is a greater problem. The SE images presented here were taken mostly because that is the only option available when doing EDS mapping and analysis on the SEM used.

5.2.1.1 Debris sample

A small fragment of the debris was removed from the larger piece, and carbon-coated for analysis by SEM/EDS. **Figure 32** shows a BSE SEM image of the debris. The material consists of a fibrous tangled mat of material, with coarse angular grains over the surface and embedded within the mat. The granular material adheres to the mat, encapsulating the fibers in some places, and in several areas appears to have formed by disaggregation of a larger, more continuous deposit (**Figure 33**). The texture of the granular material suggests that it formed as a gel; it is generally covered with shrinkage cracks, and in areas, shows a botryoidal structure. During mapping and point analysis (when the beam current was increased), heating by the electron beam caused decrepitation of the sample, indicating that it contained water. The material is interpreted to be hydrous amorphous aluminum hydroxide, consistent with the lack of diffraction peaks when analyzed by XRD (Section 3.2). Hydrogen is not detectible by X-ray analysis, and aluminum oxide would show an identical EDS X-ray spectrum; however, aluminum oxide does not generally form an amorphous phase (Lee et al., 2009). To verify the identity of the phase, particles were analyzed by Fourier Transform Infrared Spectroscopy (FTIR), and Raman Spectroscopy. FTIR spectra showed very broad peaks due to the amorphous nature of the material, and were dominated by peaks for water/OH and for Al-O bonds. No carbonyl or carbonate signal was detected, but a single peak was present that did not match any inorganic aluminum phase and apparently represents organic material. Raman spectroscopy proved difficult due to sample fluorescence caused by organic compounds in the samples. The Raman spectra that were collected were of poor quality, but had small, broad peaks that probably represent organic or aluminum-organic complexes, although no unique matching phase was identified in the Raman spectral database. In short, the material appears to be hydrous amorphous aluminum hydroxide, with an undetermined amount of organic material, possibly present as an aluminum organic complex. It is unlikely that the organic component is large, however. The samples were carbon coated for analysis, but despite this, most of the EDS analyses that were collected from the aluminum-rich material had only small carbon peaks (a few did have large peaks). The organic material may be organic acids leached from the wood as it decayed, a process probably enhanced by fungal action, or may be exometabolites produced by the fungi itself.

Point X-ray analyses in **Figure 33** show that the fibrous material is organic, consisting mostly of carbon (C) and oxygen (O) with small amounts of potassium (K) and phosphorous (P); very small iron (Fe) peaks were also observed. X-ray spectra for the granular material showed only aluminum (Al) and O, in some cases with a small peak for K. A high magnification view of the fibrous organic material is shown in **Figure 34**. The fibrous material is a tangled mass of intergrown branching and anastamosing fibers, and appears to be a fungal mycelium, consisting of branching filamentous hyphae.

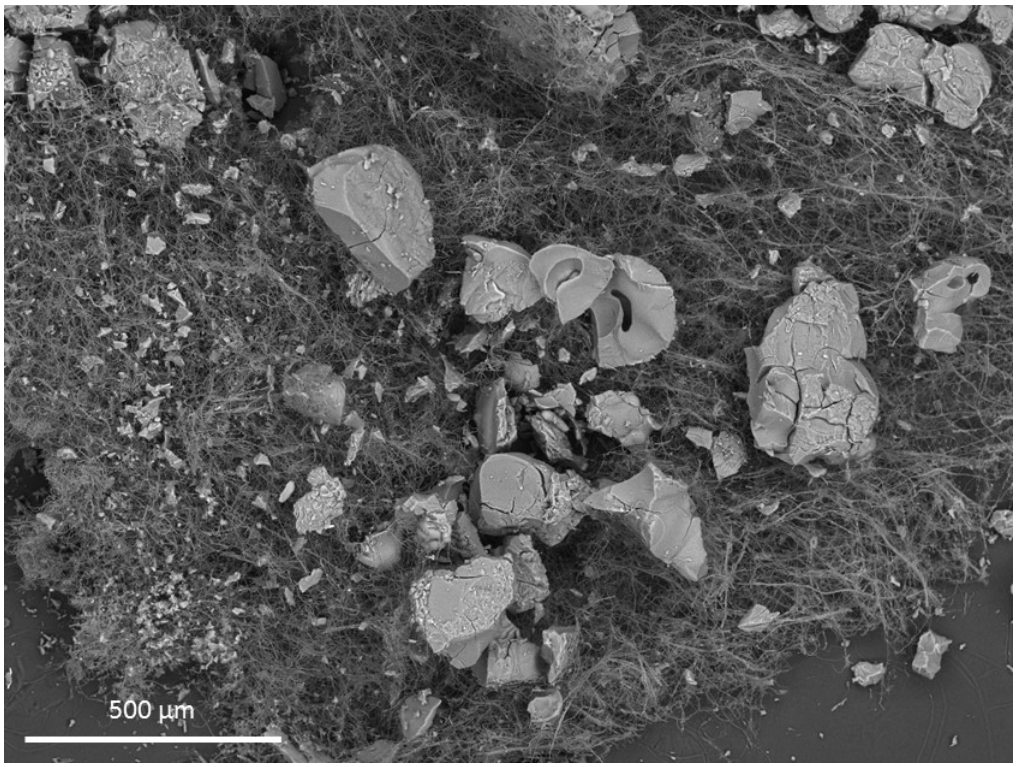

Figure 32. SEM BSE image of the Debris sample, showing the distinctive shrinkage cracks and in some areas, botryoidal morphology of the aluminum hydroxide.

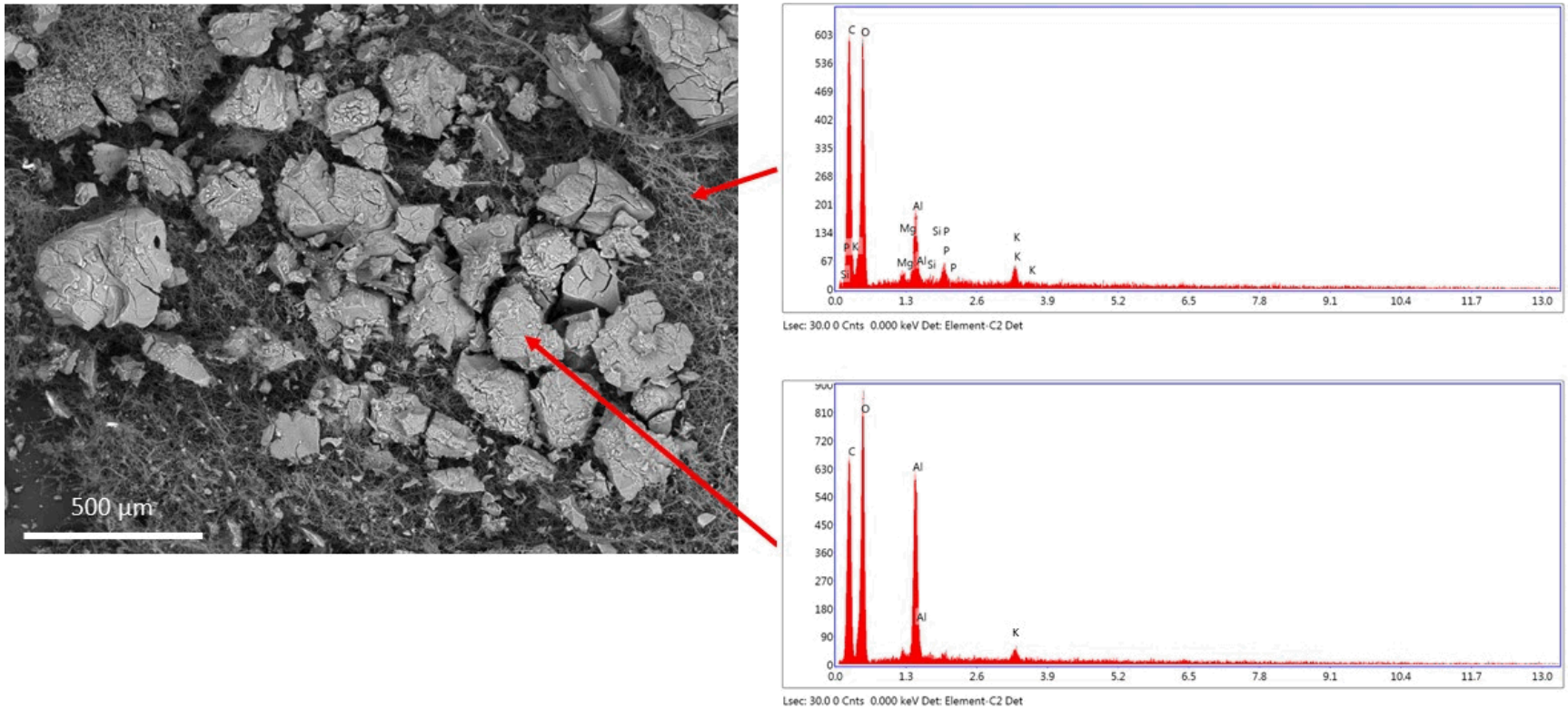

Figure 33. SEM BSE image of the Debris sample, showing the filamentous fungal matrix and the adhering amorphous aluminum hydroxide.

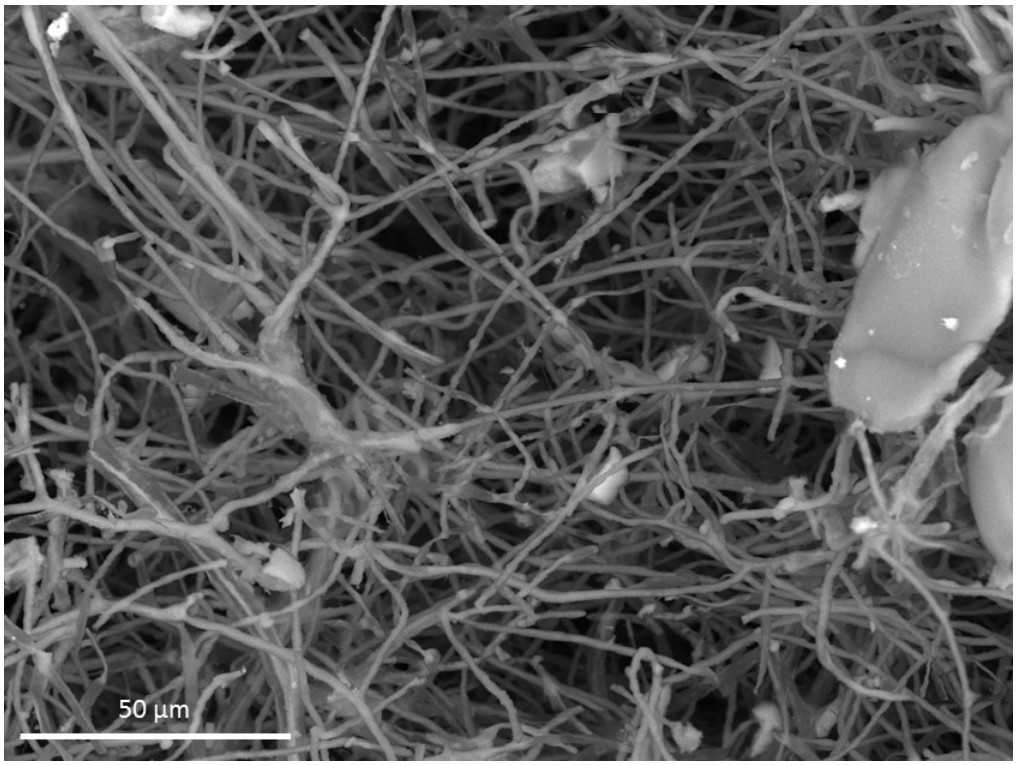

Figure 34. SEM BSE images of the Debris sample, showing close-up images of the fungal mat.

5.2.1.2 Dry swipes from the debris and residue locations

The dry swipes from the debris and the residue locations were virtually identical. Both had a brown discoloration, consisting of fine, dry material, that could be readily dislodged from the filter. For each sample, a fragment of the filter was cut from the stain and analyzed by SEM. **Figure 35** shows BSE images of the two samples, illustrating the fine particles adhering to the fibrous filter. **Figure 36** shows a SE image, element maps, and X-ray spectrum for the sample from the debris location. Spectral analysis of broad areas of the filter coated with many particles, and FTIR/Raman spectrographic analysis of extracted particles, indicates that the material consists largely of hydrous aluminum hydroxide, but high concentrations of potassium are also present. However, point analysis of individual grains of the aluminum hydroxide showed that they were nearly pure aluminum hydroxide, suggesting that the potassium is related to the brown stain on the filters. It was originally considered possible that the brown staining was iron oxides, possibly from corrosion of iron nails in the cribbing. However, no separate iron phase was observed with the SEM. This was true for all locations examined. It seems likely that the brown discoloration is due to organic compounds (e.g., organic acids) derived from the wooden cribbing, rather than to iron oxides.

Also present on the dry swipe from the residue location is fragment of insect matter (**Figure 37**). The fragment consists of a small piece of material, covered with hairs and in some locations, scales. It is insufficient to identify the organism that it represents.

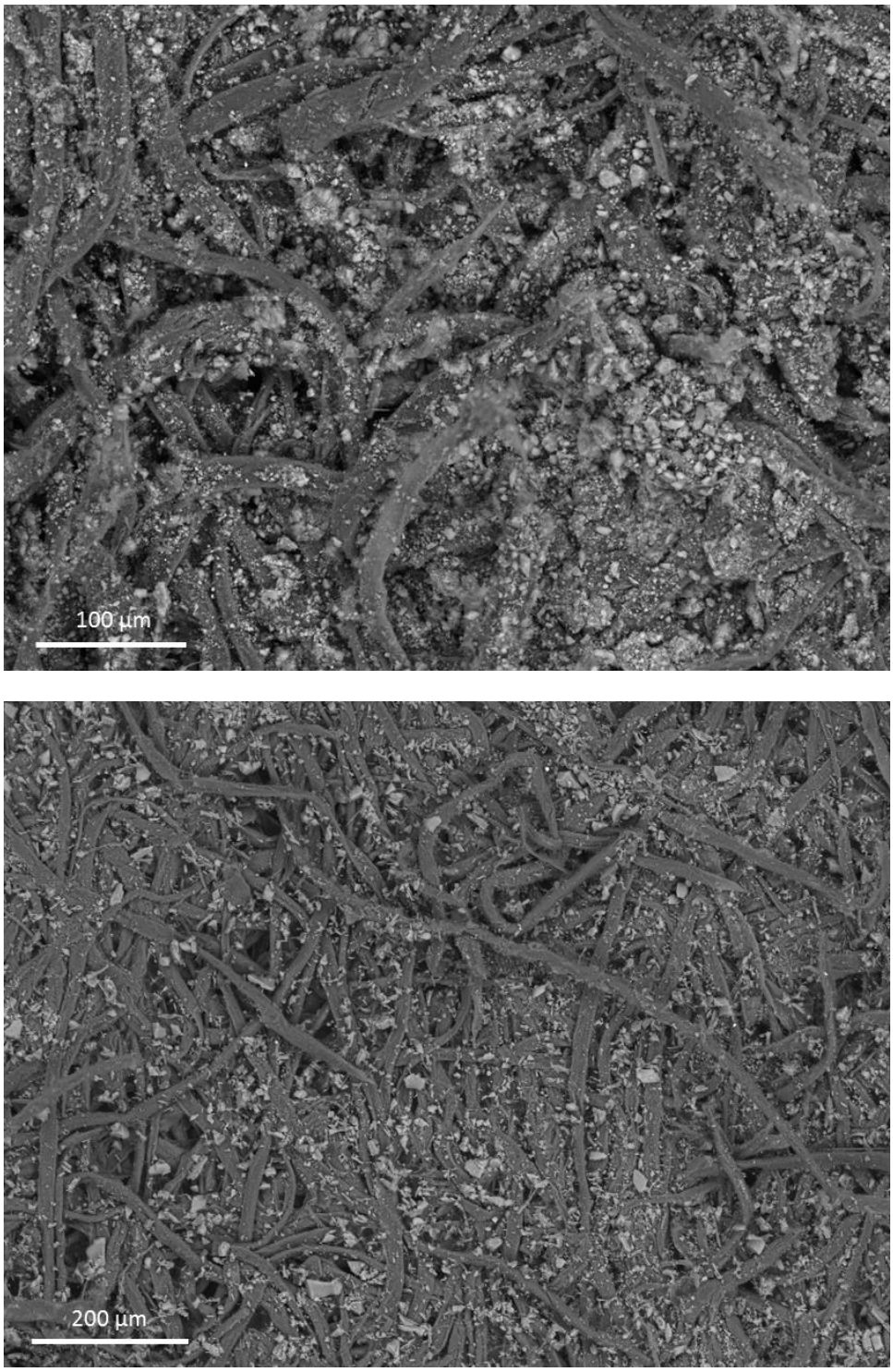

Figure 35. SEM BSE images of the dry swipe from the debris location (upper) and the residue location (lower), showing the aluminum hydroxide particles adhering to the filter.

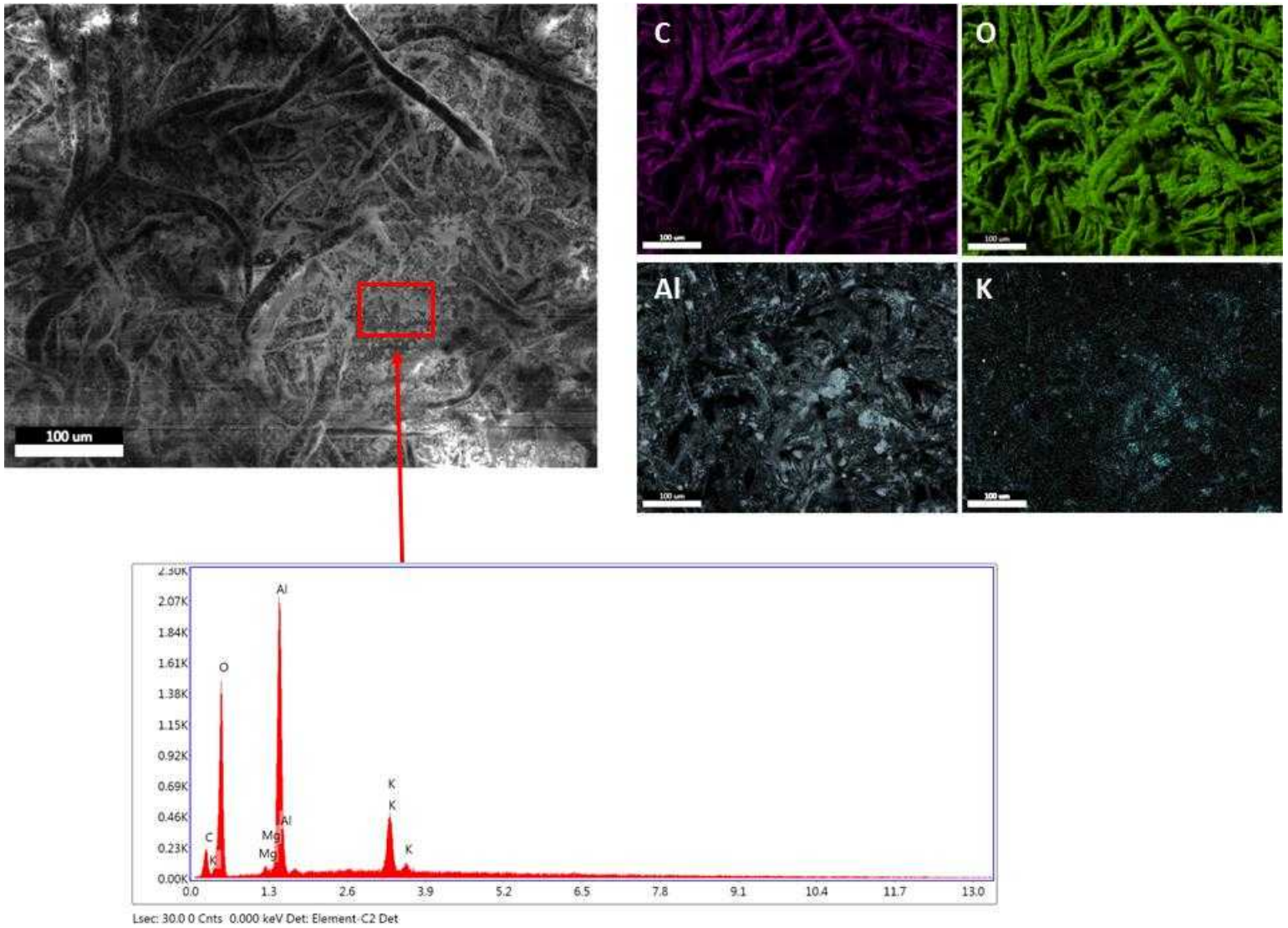

Figure 36. SEM SE image, element mays, and EDS X-ray spectrum of particulates on the surface of the dry swipe from the debris location.

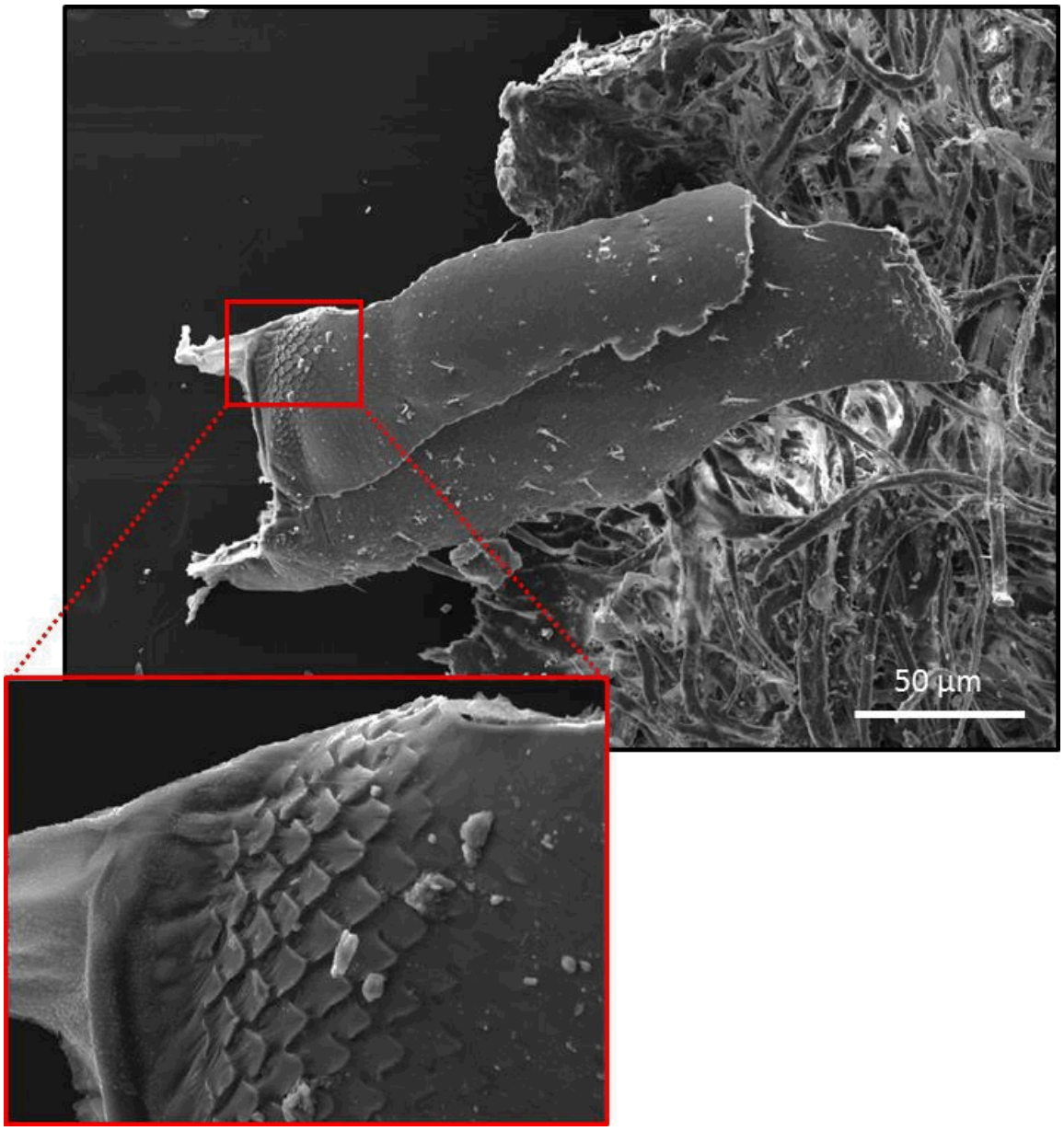

Figure 37. SEM SE images of insect fragment on the dry swipe sample from the residue location.

5.2.1.3 Wet swipe from the residue location

Two sequential wet swipes were taken from the residue location. Both had brown staining; however, the first swipe also had coarse, sand-sized white particles adhering to it. Some of these were brushed off of the filter and mounted on carbon tape for SEM analysis. The particles and an EDS point analysis are shown in **Figure 38**. Based on the EDS data and Raman/FTIR spectroscopic analysis of the particles, they consist of hydrous aluminum hydroxide, with no detectible impurities, and have a similar morphology (shrinkage cracks) to the grains of aluminum hydroxide on the debris sample. Note that in these clean, large grains of the amorphous material, it is clear that any organic component is very small, as the carbon peak is insignificant. An insect fragment was also present on this sample (**Figure 39**). The fragment appears to be part of an insect head; however, it is too incomplete to identify the type of insect.

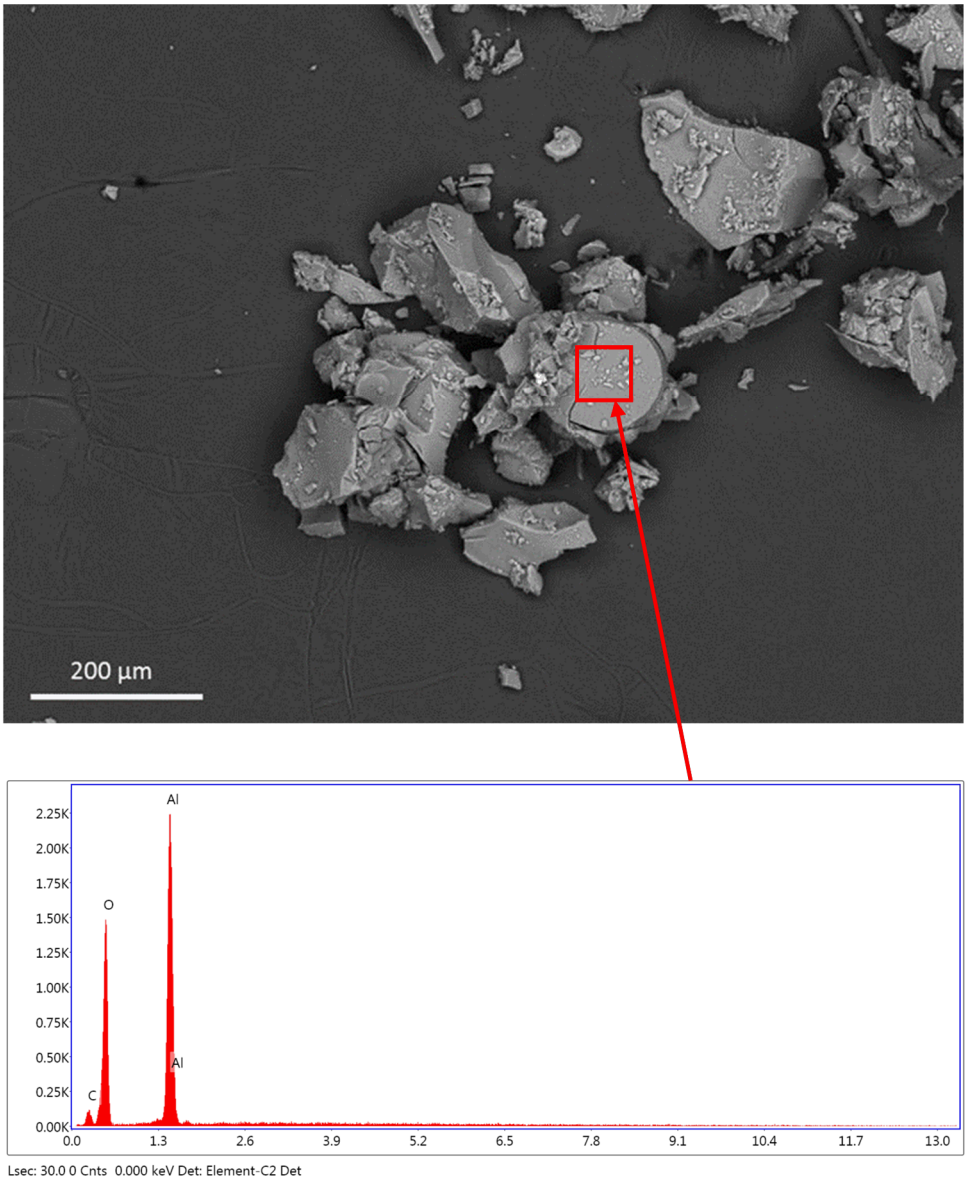

Figure 38. SEM BSE image of the particles from the wet swipe of the residue location, with EDS X-ray point analysis.

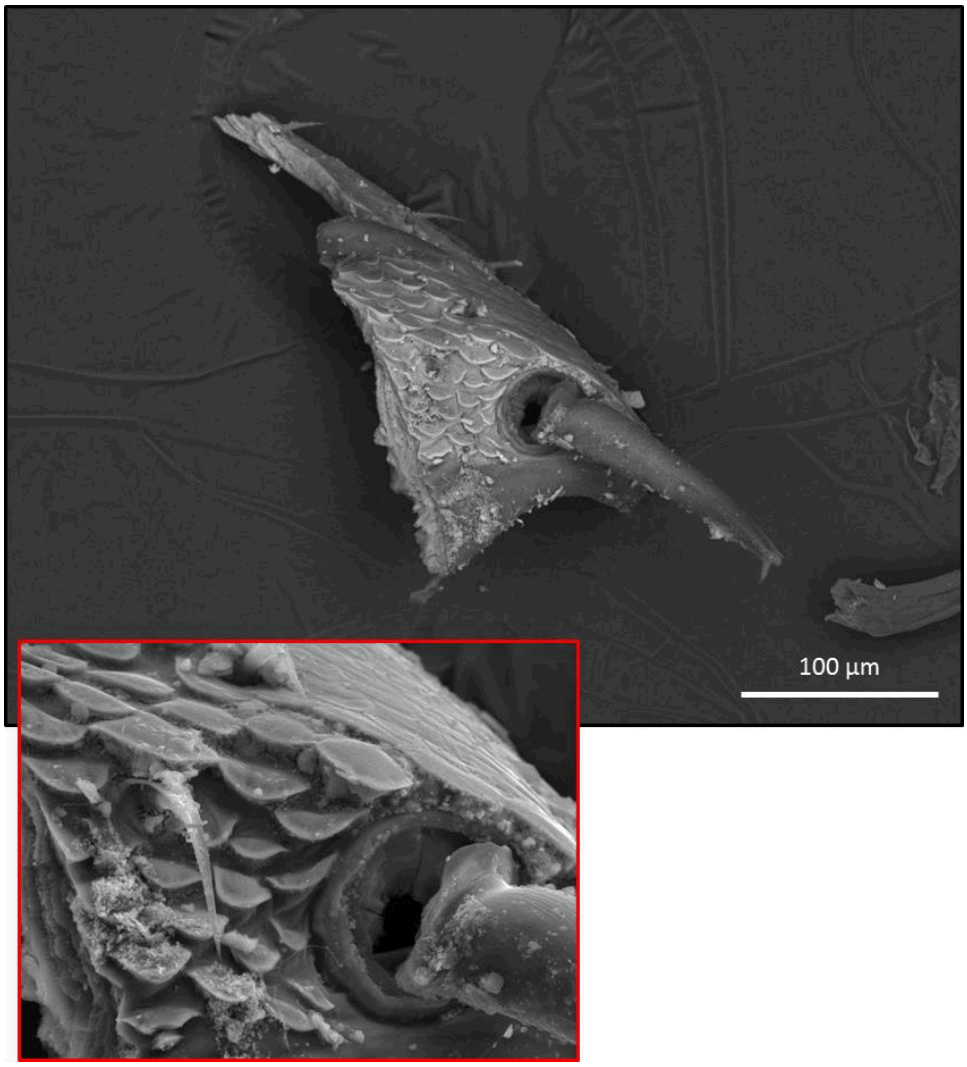

Figure 39. SEM BSE images of the insect fragment on the wet swipe of the residue location.

5.2.1.4 Discussion of the SEM data.

SEM analyses of the debris and the swipe samples indicate that most of the residue on the aluminum basket and rails consists of aluminum hydroxide, and indeed represents corrosion of the aluminum. The aluminum hydroxide corrosion residue is present as an amorphous material, that may have formed as a gel. The locations where corrosion occurred appear to be associated with biological activity. Debris present on the aluminum has been identified as fungal matter, and insect fragments have also been identified. These may be related. Several insects exist in a symbiotic relationship with fungi, including bark and wood-boring (ambrosia) beetles, and some species of tower termites and ants (Vega and Blackwell, 2005). The beetles help disperse the fungi by transporting it to new locations. The beetles disseminate the fungi in their tunnels and brood galleries, where it grows on the exposed wood surface. The beetles and/or their larvae feed on the fungi growing on the wood surface and on fungus-colonized, partially degraded wood (Licht and Biedermann, 2012). Although other explanations are possible, it seems likely that wood or bark beetles were present in the cribbing when it was placed in the cask, and they inoculated the wood with the observed fungus. During the boroscope inspection of the cask, many

small dead insects were observed on the floor of the cask. Photographs are shown in **Figure 40**; the photographs are of insufficient quality to identify the insects, but the identity can be determined when the cask is cleaned, if the dead insects observed at the bottom of the cask can be recovered and identified. Note that in **Figure 40**, the smaller images do *not* represent higher magnification views of the insects in the single larger image; each image is independent.

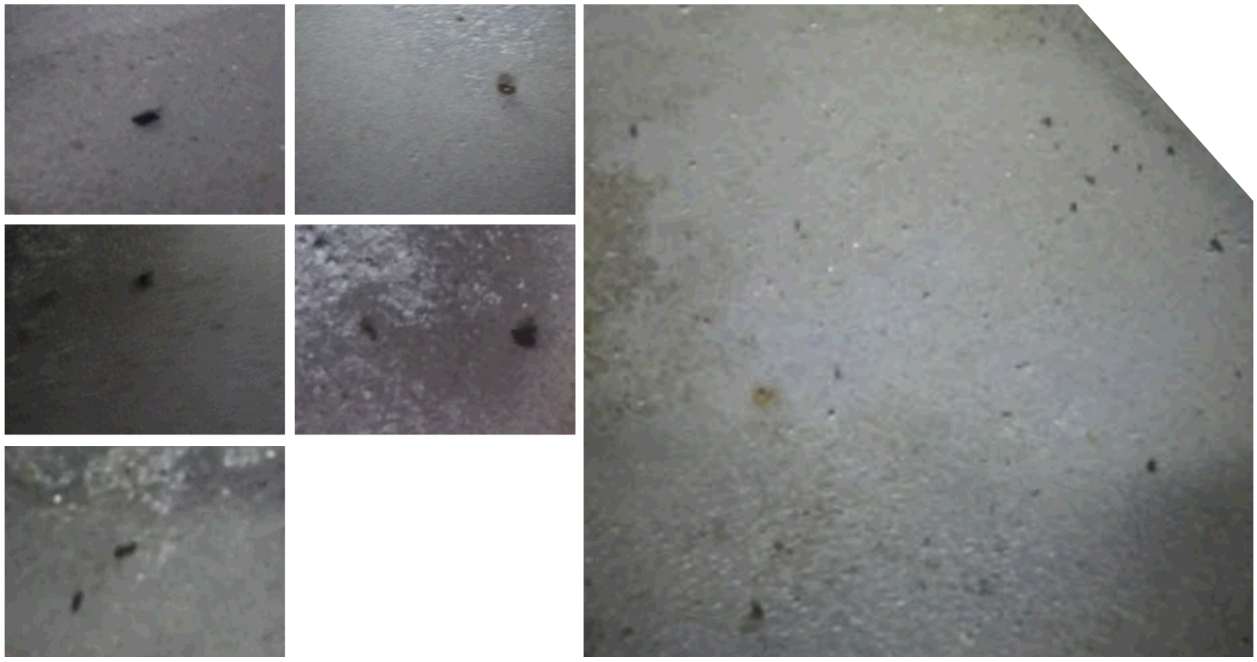

Figure 40. Boroscope camera images of insects on the floor of the HBU storage cask. The scale is not provided in the images, but comparison with structural features in the images (not shown), indicates that the insects are 2-4 mm in size.

It is clear from the SEM photos that the fungi were present before or during the corrosion process, as the corrosion products are deposited on top of the fungal mat, and as small particles scattered throughout the mat. Moreover, it is clear from the morphology of the fungal mycelium that the fungus grew over the surface of the aluminum. Hence, fungus growth occurred after the cribbing was placed in the cask and the cask was sealed. Similarly, the dead insects in the bottom of the cask suggest that living beetles were present when the cask was sealed. If they are indeed wood beetles, as we hypothesize, it seems likely that the insects actually pupated in the wood and bored out during storage, dying in the sealed cask.

5.2.2 XRD Analysis

Samples that were analyzed by XRD consisted of the coarse corrosion product grains extracted from one of the wet pads from the "residue" location, and loose grains associated with the "debris" sample. The grains were crushed in a mortar and pestle and then slurried onto a zero-background silicon wafer prior to analysis. However, when analyzed, no peaks were observed, indicating that the material is amorphous. On the basis of textural and compositional data determined by SEM and the Raman/FTIR analyses, the granular material is inferred to have formed as an amorphous aluminum hydroxide gel.

5.2.3 Chemical Analysis

The methods used for digestion and chemical analysis of the samples are described in Section 5.1. After digestion, the corrosion samples were analyzed using a semi-quantitative ICP-MS survey method to determine what elements were present. This analysis identified a suite of elements that were then

analyzed using quantitative methods. The results of the quantitative analyses, including the analysis of the blank filter provided with the samples, are provided in **Table 9**. In **Table 10**, the blank-subtracted concentrations are given; it is important to note that the number of filters varied from sample to sample, so different blank filter values were subtracted from each sample.

A blank and five calibration standards were used for the quantitative analysis. Standard concentrations were 3, 10, 30, 100, and 1000 ng/ml. Samples were diluted until they fell within the range of the standards. The ICP-MS has extremely high sensitivity, with good signals for even the lowest standard (3 ng/ml). Based on analysis of the standards as unknowns, all values in **Table 9** and **Table 10** are accurate to ±5% or better.

Al is by far the most abundant element, followed by K and Fe, and then by P and Mg. Other metals that are present in significant amounts are Cu, Mn, Cr, Zn, and Ti. Trace quantities of Ba, Pb, Ag, and Zn are also present. Most of these metals are in the aluminum alloy comprising the basket rails, and their concentrations are consistent the source being corrosion of the aluminum. The aluminum is ASTM B-221 6061-T6, which has the following compositional specifications:

- Si, minimum 0.4%, maximum 0.8% by weight
- Fe, no minimum, maximum 0.7%
- Cu, minimum 0.15%, maximum 0.4%
- Mn, no minimum, maximum 0.15%
- Mg, minimum 0.8%, maximum 1.2%
- Cr, minimum 0.04%, maximum 0.35%
- Zn, no minimum, maximum 0.25%
- Ti, no minimum, maximum 0.15%
- Other elements no more than 0.05% each, 0.15% total
- Remainder aluminum 95.85–98.56%

In **Table 11**, the concentrations of these elements are normalized to the measured aluminum concentrations in each sample. The normalized range in AA 6061-T6 is also provided. With the exception of Fe, the values for each element fall within or very close to, the possible range in the aluminum alloy. It is likely that these elements can be sourced to corrosion of the aluminum.

Fe, and also K and P, which are not present in AA 6061-T6 in significant amounts, cannot be sourced solely to the aluminum. These elements are in or on the fungal material itself, but also are present in the dark stain on the dry swipes, which consists of stained particles of aluminum hydroxide. Based on the SEM results, the aluminum hydroxide itself does not display X-ray peaks for these elements, or displays only very small peaks. It is inferred that these elements are concentrated within the fungal matter, but also within the organic material forming the dark stain. The brown coating is probably mostly organic in nature, and might contain compounds such as organic acids that complex the metal species present, including the Fe, K, and P.

Table 9. Elemental Composition of the HBD Cask Corrosion Samples, in µg/sample

Sample ID	K	Mn	Cr	Mg	Zn	Fe	Cu	Ti	P	Al	Ba	Pb	Ag	Zr	# filters
Filter blank	0.2	0.1	0.0	2.6	2.1	5.1	0.7	0.5	0.1	5.5	0.2	0.1	0.2	0.0	1
Debris side dry	97	1.7	2.4	9.0	5.8	44	7.7	3.9	12	1280	0.7	0.2	0.2	0.3	1
Debris side wet	334	4.6	5.9	30	13	149	17	8.6	54	5230	2.6	0.7	0.9	21	3
Debris	39	2.2	0.5	8.7	1.5	10	2.5	0.5	6.6	1100	0.1	1.4	0.4	0.1	0
Residue side dry	38	1.2	1.4	13	4.1	43	5.1	3.3	11	1060	0.4	0.2	0.1	0.2	1
Residue side wet	169	3.7	4.7	24	7.4	100	21	6.5	53	4170	1.1	0.4	0.2	0.4	2

Table 10. Elemental Composition of the HBD Cask Corrosion Samples, in µg/sample (blanks subtracted)

Sample ID	K	Mn	Cr	Mg	Zn	Fe	Cu	Ti	P	Al	Ba	Pb	Ag	Zr
Debris side dry	97	1.6	2.4	6.4	3.7	40	7.0	3.4	12	1270	0.5	0.1	0.1	0.3
Debris side wet	334	4.2	5.8	22	7.1	134	15	7.1	54	5220	2.0	0.3	0.4	21
Debris	39	2.2	0.5	8.7	1.5	10	2.5	0.5	6.6	1100	0.1	1.4	0.4	0.1
Residue side dry	37	1.0	1.4	10	2.0	38	4.4	2.8	11	1060	0.2	0.1	0.0	0.2
Residue side wet	168	3.5	4.6	19	3.1	90	20	5.6	52	4160	0.8	0.1	0.0	0.4

Table 11. Elemental compositions, normalized to the Aluminum Content in Each Sample.

Sample ID	Fe	Cu	Mn	Mg	Cr	Zn	Ti
Debris side dry	0.0312	0.0055	0.0013	0.0051	0.0019	0.0029	0.0027
Debris side wet	0.0256	0.0028	0.0008	0.0042	0.0011	0.0014	0.0014
Debris	0.0092	0.0023	0.0020	0.0079	0.0005	0.0013	0.0004
Residue side dry	0.0357	0.0041	0.0010	0.0099	0.0013	0.0019	0.0026
Residue side wet	0.0216	0.0047	0.0008	0.0045	0.0011	0.0008	0.0013
Al 6061 Max	0.0073	0.0042	0.0016	0.0125	0.0037	0.0026	0.0016
Al 6061 Min	0.0000	0.0015	0.0000	0.0081	0.0004	0.0000	0.0000

5.3 Discussion

To summarize the results of this assessment, aluminum corrosion product was present at both of the sites where residue was observed on the aluminum basket rails. The aluminum-rich material was amorphous, and had a morphology that suggests it formed as a gel. The material decrepitated under the electron beam, indicating that it still contained water. SEM/EDS and FTIR analysis indicate that material is likely to be hydrous aluminum hydroxide. SEM analysis showed that the spongy residue sample from one of the sites consisted largely of filamentous fungal material. At the "residue" site, this fungal mat coated the most or all of the corroded region (**Figure 31**). Embedded within and on the fungal material were grains of the aluminum corrosion product. A brown coating was present on much of the aluminum hydroxide and on parts of the fungal mass. Originally suspected of being iron oxide, the brown coating instead appeared to be organic in nature. The coating was enriched in K, Fe, and P. However, these elements were largely disseminated, occurring as complexed species rather than discrete phases in the coating. Also present at each of the two corrosion sites were insect fragments; moreover, dead insects were observed via borescope at the bottom of the cask.

Chemical analysis of the samples collected from the residues showed that many trace metals were present, most of them in amounts consistent with their source being corrosion of AA6061, the material comprising the basket rails. Elements present in greater amounts than could be explained by corrosion of the aluminum metal are K (the second most abundant metal in the samples), Fe, and P, the species enriched in the organic coating. The brown material is interpreted to consist of fungal exometabolites and breakdown products of the wood (e.g. organic acids); fungal exometabolites specifically scavenge important nutrients such as K, Fe, and P from the wood as it is broken down, making them bioavailable to the fungus. It is clear from the presence of these elements (which must be sourced to the wood), and the presence of the fungus and insect fragments, that the polypropylene wrapping on the cribbing was leaking, allowing fluids from the wood to contact the aluminum metal.

There are a number of potential explanations for the observed attack on the aluminum basket rails:

- Crevice corrosion
- Corrosion due to chemicals used for wood treatment (a number of which are aggressive with respect to aluminum) leaching out of the cribbing.
- Corrosion due to organic acids leaching out of the wood.
- Corrosion due to alteration of the local chemistry by fungi.

Crevice corrosion requires an occluded geometry that sufficiently limits transport of electrolyte species (e.g., O_2, H^+), setting up different environmental conditions between outside and inside the crevice (e.g., acidification in crevice and/or different metal ion concentrations) and/or causes sufficient potential drop (IR) for de-passivation to occur. Crevice corrosion of aluminum is unlikely in the absence of aggressive species, but in this case, possible aggressive species include organic compounds produced by leaching of organic acids from the wood and by fungal attack of the wood which clearly occurred. There is no evidence that anoxic conditions occurred developed in the corroded area. Fungi are aerobes, and the presence of the fungal matter, at the "debris" location, where the fungal mycelium covers most or all of the corroded site, suggests that conditions were oxic. Could the fungi have infiltrated into the crevice and into the aluminum-rich gel after cessation of corrosion and the return of aerobic conditions, but prior to hardening of the gel? This is not consistent the observed texture of the "debris" sample, which clearly shows that gel formed on the surface of the existing fungal material; the fungal material is not embedded in the gel, as it would be if it had infiltrated an existing gel. Moreover, the morphology of the aluminum gel suggests that it formed by evaporation on a free surface, indicating that the top of the fungal mat was exposed to the air in the cask. Finally, aluminum is toxic to fungi, as it is to all living things, and infiltration of fungal mycelium into a concentrated aluminum gel is not rational. It is possible that crevice corrosion occurred elsewhere—in a region where the fungal mat was not present—and the aluminum

diffused out of the crevice and solidified into a gel on the fungal mat; however, at the debris site, the fungal material appears to cover most or all of the corroded area. Given the presence of organic compounds and fungi that are known to support corrosion in oxic conditions, there is little reason to speculate that an anoxic crevice developed. Although the crevice may not have generally been anoxic, other chemical gradients, such as variation in pH, may have developed due to the occluded geometry that promoted crevice corrosion. It is also possible that the major role of the crevice, if present, was to trap water via capillary action, maintaining wet conditions against the aluminum metal.

Standard wood treatments to eliminate insect infestation and fungal rot include chromated copper arsenate (widely used for industrial applications) and several copper compounds, involving both organic copper compounds and sub-micron metallic copper (WWPI, 2011). These copper-bearing compounds are corrosive with respect to aluminum. However, in this case, fungi and possibly living insects were present, suggesting that the wood was not treated. Moreover, the wood treatments are quite concentrated, and in order to be effective, retention of the chemicals in the wood is required to be at levels of 0.1 to 0.4 lb/ft^3 (WWPI, 2011) which, depending on wood density, equates to 0.3 to 1.8% by weight (thousands to tens of thousands of ppm). Other than nutrients extracted from the wood (Fe, K, and P), the metals present in the samples, including Cu, were not significantly elevated relative to what would be released by dissolution of the aluminum alloy (ASTM-B-221-6061-T6) as it corroded, assuming stoichiometric dissolution, again suggesting that none of these wood treatments were used. An additional wood treatment that is commonly used is potassium borate; however, although elevated potassium was observed in the samples by both SEM EDS and ICP-MS, boron (readily measured by ICP-MS) as not detected, indicating that this treatment was also not used. Thus, it is concluded that wood treatments were not responsible for the observed aluminum corrosion.

Organic acids leached from the wood are a possible cause of the observed corrosion, and this can occur in oxic conditions. It is well known that freshly-cut hardwoods and softwoods emit corrosive compounds, including acetic and formic acids and formaldehyde (Arni et al., 1965a; Arni et al., 1965b; Ryhl-Svendsen and Glastrup, 2002; Gibson and Watt, 2010). These compounds are generated both by chemical reactions and microbiological activity in the fresh wood (Arni et al., 1965a). The brown organic film observed at both sites is clearly sourced to degradation of the wood. However, given the presence of fungi that readily decompose wood for nutrients and the observed enrichment of nutrients (iron, phosphorous, and potassium) in the organic material at both the corroded sites, it is likely that fungi played a role in the corrosion. Wood degradation and production of organic acids are greatly increased by fungal activity (all common types of wood rot are fungal processes, Fungiora, 2006); moreover, fungi release exometabolites to aid in wood breakdown and nutrient extraction. These exometabolites include siderophores, which include the strongest known complexants for Fe and other metals. For instance, for enterobactin, a bacterially-produced siderophore, the formation constant K for the Fe complex is $>10^{45}$ (Hider et al., 1981).

As discussed in Section 5.2.1.4, it is clear that fungal activity, and probably insect activity, occurred after the cribbing was placed in the cask and the cask sealed. The insects may have been wood beetles living in the wooden cribbing. Damage to the plastic that was wrapped around the cribbing, or simply gaps in the wrapping, allowed aqueous solutions from the infested regions to contact the aluminum and cause corrosion. In the case of the "debris location", the fungal mycelium itself extended through the plastic and coated the metal. One role of the fungus may have been to produce a wet biofilm and a moist environment on the aluminum surface. Fungal breakdown of wood produces water as a metabolic byproduct, and that water is retained in the moist biofilm surrounding the fungus, eliminating any need for excess moisture or condensation within the plastic wrap surrounding the cribbing. However, it is likely that the fungus played an active role in the aluminum corrosion by (1) decomposing the wood and enhancing organic acid leach rates; and (2) producing corrosive exometabolites. Fungi decompose wood largely by use of enzymes that break down cellulose or lignin, although some also generate hydrogen peroxide. The fungi break down wood to produce organic compounds including a variety of organic

acids that lower the pH in the biofilm (Hammel, 1997; Sánchez, 2009). The organic acids are also strong complexants of metal ions including iron and aluminum, increasing their solubility and potentially destabilizing the oxide layer on the aluminum. The fungus itself releases compounds called siderophores that strongly chelate metal ions and may have damaged the oxide layer on the aluminum. Fungi release siderophores to complex and solubilize iron, a necessary nutrient, making it more bioavailable. While iron is most strongly bound by siderophores, aluminum is also chelated (Roy and Chakrabartty, 2000; Rogers et al., 2001; Illmer and Buttinger, 2006). Increasing Al concentration as the pH drops due to organic acid production will probably stimulate a rise in siderophore production (although this has a complex dependence on the available Fe concentration). The reason for the increase in siderophore production is not well understood, but appears to be either in an effort to (1) chelate and detoxify Al; (2) increase iron availability by reducing the effects of Al-Fe competition for siderophores; or (3) simply in response to oxidative stress (Illmer and Buttinger, 2006). However, if elevated Fe is present, then siderophore production does not increase, as sufficient Fe is present in soluble form to support bioactivity regardless of the aluminum. In the case of the high-burnup cask, Fe concentrations were elevated—about 1-3% of the total Al values in the bulk sample (which is extremely high given the very low solubility of Fe oxides), and the Fe-to-soluble Al ratio was probably even higher, since Fe is preferentially complexed by siderophores. This may have limited fungal sensitivity to Al concentrations and allowed continued growth of the fungus, even after the aluminum began to corrode.

Corrosion of aluminum by fungi has previously been reported. Belov et al. (2008) performed an experimental study with aluminum coupons exposed to water containing fungal spores, both in the presence and absence of a growth medium. The results indicated that the fungi did not utilize aluminum directly as an energy source, but did cause aluminum to corrode in the presence of a growth medium. The cause of corrosion was not clear. Initially, an exudate of neutral to moderately basic pH formed on the surface of the aluminum, containing alkali metal ions that had been extracted from the growth medium by the fungi. The formation of this moderately basic pH solution was attributed to the reaction of oxygen radicals produced by fungi with water to form hydroxyl ions and hydrogen peroxide. Over time, an aluminum-rich jelly-like material was formed; concomitantly, the pH dropped to neutral values. Initially, the corrosion product contained only aluminum species; however, over a few months, a significant fraction of the material was biogenic, consisting of a suite of organic acids. Belov et al. (2008) speculate that the organic acids actually form by cell lysis, after cell death; however, similar acids have been identified as metabolites produced by fungal breakdown of wood (Hammel, 1997; Sánchez, 2009). Acidic fungal metabolites and possibly, cellular lysis products have also been identified as facilitating localized corrosion of aluminum fuel tanks on aircraft (Salvarezza et al., 1983) (antifungal agents are frequently added to aircraft fuel specifically to avoid fungal corrosion of the aluminum tanks). Although chloride played a major role, the organic acids helped destabilized the protective oxide layer on the aluminum by lowing the pH of the medium, but also had an additional effect, possibly related to complexation of aluminum in solution.

Note that in the two studies above, wood was not present, and corrosion was attributed exometabolites produced by the fungi (e.g. oxygen radicals, siderophores), and possibly to products of cell lysis. The function of siderophores is to complex iron and increase its bioavailability, but these compounds are also strong ligands for Al. At the locations where corrosion was observed in the HBU demonstration cask, solutions containing elevated levels of metal chelators probably damaged the protective oxide layer on the aluminum, resulting in corrosion. Later, after fungal death, organic acids produced by cell lysis and by degradation of the wood may have produced an acidic solution that further supported corrosion. This is consistent with the observed textural relationship in the “debris” sample, which indicates that the fungus preceded corrosion, and does not require that fungi have propagated in the aluminum-rich toxic gel that would have been produced by corrosion.

We speculate that the association of the fungi and insects in not coincidental, but rather that wood-boring beetles, which inoculate wood with fungi and then harvest the fungi for food, were present in the wood.

While the presence of wood-boring beetles is speculative, it is noted that small dead insects were observed in the bottom of the cask during the inspection. When the cask is cleaned, the insects should be collected and identified to verify the hypothesis.

To summarize, several different possible corrosion mechanisms were considered. Corrosion due to wood treatments is unlikely, because the distinctive chemical signature of such treatments was not found, and because such treatments are specifically intended to inhibit wood rot through fungal attack, and the presence of fungi shows that the wood was not treated. The presence of organic aggressor species in the seepage could have supported crevice corrosion, but evidence suggests that anoxic conditions did not occur. However, as noted previously, a crevice may have acted to capture water via capillary processes, keeping the contact area wet and allowing corrosion to occur. However,; a crevice was not necessary, because the organic compounds present would have been sufficient to corrode the metal in the absence of a crevice. These organic compounds include both organic acids leached from the wood—which would have been released in higher concentrations because of fungal degradation of the wood—and fungal exometabolites and products of cell lysis that complex Al and damage the passive layer on the metal surface. Given the evidence that the fungi preceded corrosion, and the presence of the fungi or organic matter that clearly indicates fungal activity occurred at both corrosion sites, there is a strong likelihood that the fungi contributed to the corrosion; this is true whether or not the corrosion occurred in an anoxic crevice, or under oxic conditions. However, regardless of the mechanism, it is clear that corrosion of the aluminum metal was due to contact with the wooden cribbing.

5.4 Conclusions: High Burnup Demo Corrosion Residues

On September 29-30, 2015, a team consisting of Electric Power Research Institute personnel, AREVA personnel (AREVA Federal Services, AREVA TN, and AREVA P&T), and personnel from Dominion Virginia Power performed an inspection of the TN-32B cask that will be used for the high-burnup demonstration project. During the survey, polypropylene-wrapped wooden cribbing that had been placed within the cask prior to shipment to prevent shifting of the basket was removed, revealing two small areas of residue on the aluminum basket rails, where they had contacted the cribbing. The nature of the residue was unknown, but it appeared to be a corrosion product and concerns were raised that similar attack could exist at more difficult-to-inspect locations in the canister. The decision was made to collect samples of the residue for evaluation and to allow a technical assessment of the observed attack.

Samples of the suspected corrosion residue were collected the next time the cask was opened (July, 2016) and sent to SNL for analysis. The materials consisted of a single bulk sample of the filamentous, spongy residue, and several samples collected by swiping the residues at each of the locations with 5-inch paper filters. At SNL, the samples were imaged and analyzed using a SEM/EDS. Bulk analysis was then carried out using ICP-MS.

Analysis of the samples showed that aluminum corrosion product was present at both sites. The aluminum-rich material was amorphous aluminum hydroxide, and formed as a gel. Filamentous fungal material was also present, as was brown organic material containing elevated levels of K, Fe, and P. Unidentifiable insect fragments were present at each of the two corrosion sites; moreover, dead insects were observed via borescope at the bottom of the cask. The presence of organic material enriched in these elements (which must be sourced to the wood), the fungus, and the insect fragments, indicates that the polypropylene wrapping on the cribbing was damaged, allowing fluids from the wood, or the wood itself, to contact the aluminum metal. It is clear that contact with the cribbing caused the observed corrosion.

The corrosion could have been due to a combination of crevice effects, organic acids leached from the wood, or fungal growth. Evidence suggests that fungal growth played an important role, possibly through both through direct and indirect processes. Fungal activity produces powerful metal complexants that have been shown to promote aluminum corrosion, but also is the dominant mechanism of wood decay,

increasing organic acid release. Regardless of the mechanism, it is clear that corrosion of the aluminum metal was due to contact with the wooden cribbing. Areas not contacted by the cribbing or fluids generated by it are unlikely to be corroded, and once the corroded sites and the cask interior have been thoroughly cleaned (the fluid may have dripped deeper into the cask), further corrosion over the course of the high-burnup demonstration test is unlikely.

6. REFERENCES

Arni, P., Cochrane, G. and Gray, J. (1965a). The emission of corrosive vapours by wood. I. Survey of the acid-release properties of certain freshly felled hardwoods and softwoods. *Journal of applied chemistry* **15**, 305-313.

Arni, P., Cochrane, G. and Gray, J. (1965b). The emission of corrosive vapours by wood. II. The analysis of the vapours emitted by certain freshly felled hardwoods and softwoods by gas chromato-graphy and spectrophotometry. *Journal of Chemical Technology and Biotechnology* **15**, 463-468.

Belov, D., Sokolova, T., Smirnov, V., Kuzina, O., Kostyukova, L. and Kartashov, V. (2008). Corrosion of aluminum and its alloys under the effect of microscopic fungi. *Protection of Metals* **44**, 737-742.

Bouchard, P., George, D., Santisteban, J., Bruno, G., Dutta, M., Edwards, L., Kingston, E. and Smith, D. (2005). Measurement of the residual stresses in a stainless steel pipe girth weld containing long and short repairs. *International Journal of Pressure Vessels and Piping* **82**, 299-310.

Bryan, C. (2017). *Analysis of Corrosion Residues Collected from the Aluminum Basket Rails of the High-Burnup Demonstration Cask.* SAND2017-2306. Sandia National Laboratories, 27 p.

Bryan, C. and Enos, D. (2015a). *SNF Interim Storage Canister Corrosion and Surface Environment Investigations.* FCRD-UFD-2015-00511. U.S. Department of Energy, 79 p.

Bryan, C. R. and Enos, D. (2014). *Analysis of Dust Samples Collected from Spent Nuclear Fuel Interim Storage Containers at Hope Creek, Delaware, and Diablo Canyon, California.* Sandia National Laboratories, 281 p.

Bryan, C. R. and Enos, D. G. (2015b). *Analysis of Dust Samples Collected from an Unused Spent Nuclear Fuel Interim Storage Container at Hope Creek, Delaware.* Sandia National Laboratories, 131 p.

Bryan, C. R. and Enos, D. G. (2016). *Analysis of Dust Samples Collected from an In-Service Interim Storage System at the Maine Yankee Nuclear Site.* SAND2016-10266. Sandia National Laboratories, 51 p.

Chang, M. C., Sioutas, C., Kim, S., Gong, H. and Linn, W. S. (2000). Reduction of nitrate losses from filter and impactor samplers by means of concentration enrichment. *Atmospheric Environment* **34**, 85-98.

Dong, P., Hong, J. and Bouchard, P. (2005). Analysis of residual stresses at weld repairs. *International Journal of Pressure Vessels and Piping* **82**, 258-269.

Dong, P., Zhang, J. and Bouchard, P. (2002). Effects of repair weld length on residual stress distribution. *Journal of pressure vessel technology* **124**, 74-80.

Elcoate, C., Dennis, R., Bouchard, P. and Smith, M. (2005). Three dimensional multi-pass repair weld simulations. *International Journal of Pressure Vessels and Piping* **82**, 244-257.

Enos, D. and Bryan, C. (2016a). *Final Report: Characterization of Canister Mockup Weld Residual Stresses.* FCRD-UFD-2016-000064. U.S. DOE, 62 p.

Enos, D. and Bryan, C. (2016b). Understanding the Risk of Chloride Induced Stress Corrosion Cracking of Interim Storage Containers for the Dry Storage of Spent Nuclear Fuel: Evolution of Brine Chemistry on the Container Surface. *CORROSION 2016*. Vancouver, B.C.: NACE International.

Enos, D. G., Bryan, C. R. and Norman, K. M. (2013). *Data Report on Corrosion Testing of Stainless Steel SNF Storage Canisters.* U.S. Department of Energy, Office of Used Nuclear Fuel Disposition, 103 p.

EPRI. (2011). *Extended Storage Collaboration Program (ESCP) Progress Report and Review of Gap Analyses.* Technical report no. 1022914. p.

EPRI. (2014). *Calvert Cliffs Stainless Steel Dry Storage Canister Inspection.* Technical Report # 1025209. 460 p.

Fales, N. (2016). *Maine Yankee Inspection, July 11-13, 2016*: Presentation to the ASME BPV XI Task Group on In-service Inspection of Spent Nuclear Fuel Storage and Transportation Containment Systems, August 22, 2016, Washington D.C.

Fungiora, O. O. (2006). Wood and tree fungi: biology, damage, protection, and use. *Springer, BerlinStahli M, Finsinger W, Tinner W, Allgwer B (2006) Wildfire history and re ecology of the Swiss National Park (Central Alps): new evidence from charcoal, pollen and plant macrofossils. Holocene* **16**, 805817.

George, D. and Smith, D. (2005). Through thickness measurement of residual stresses in a stainless steel cylinder containing shallow and deep weld repairs. *International Journal of Pressure Vessels and Piping* **82**, 279-287.

Ghosh, S. and Kain, V. (2010). Effect of surface machining and cold working on the ambient temperature chloride stress corrosion cracking susceptibility of AISI 304L stainless steel. *Materials Science and Engineering: A* **527**, 679-683.

Gibson, L. and Watt, C. (2010). Acetic and formic acids emitted from wood samples and their effect on selected materials in museum environments. *Corrosion Science* **52**, 172-178.

Hammel, K. (1997). Fungal degradation of lignin. *Driven by nature: plant litter quality and decomposition. CAB International, Wallingford*, 33-46.

Hanson, B., Alsaed, H., Stockman, C., Enos, D., Meyer, R. and Sorenson, K. (2012). *Gap analysis to support extended storage of used nuclear fuel.* U.S. Department of Energy, p.

Hider, R. C., Mohd-Nor, A. R., Silver, J., Morrison, I. E. and Rees, L. V. (1981). Model compounds for microbial iron-transport compounds. Part 1. Solution chemistry and Mössbauer study of iron (II) and iron (III) complexes from phenolic and catecholic systems. *Journal of the Chemical Society, Dalton Transactions*, 609-622.

Hossain, M., Goudar, D., Truman, C. E. and Smith, D. J. (2011). Simulation and measurement of residual stresses in a type 316h stainless steel offset repair in a pipe girth weld. *Materials Science Forum*: Trans Tech Publ, 492-497.

Hossain, S., Truman, C., Smith, D. and Bouchard, P. (2006). Measurement of residual stresses in a type 316H stainless steel offset repair in a pipe girth weld. *Journal of pressure vessel technology* **128**, 420-426.

Illmer, P. and Buttinger, R. (2006). Interactions between iron availability, aluminium toxicity and fungal siderophores. *Biometals* **19**, 367-377.

Lee, S. K., Lee, S. B., Park, S. Y., Yi, Y. S. and Ahn, C. W. (2009). Structure of amorphous aluminum oxide. *Physical Review Letters* **103**, 095501.

Licht, H. H. D. F. and Biedermann, P. H. (2012). Patterns of functional enzyme activity in fungus farming ambrosia beetles. *Frontiers in zoology* **9**, 1.

Mahmoudi, A., Hossain, S., Truman, C., Smith, D. and Pavier, M. (2009). A new procedure to measure near yield residual stresses using the deep hole drilling technique. *Experimental Mechanics* **49**, 595-604.

Mahmoudi, A., Truman, C., Smith, D. and Pavier, M. (2011). The effect of plasticity on the ability of the deep hole drilling technique to measure axisymmetric residual stress. *International Journal of Mechanical Sciences* **53**, 978-988.

NRC. (2012a). *Identification and Prioritization of the Technical Information Needs Affecting Potential Regulation of Extended Storage and Transportation of Spent Nuclear Fuel. Draft for comment.* U.S. NRC, 138 p.

NRC. (2012b). *Potential Chloride Induced Stress Corrosion Cracking of Austenitic Stainless Steel and Maintenance of Dry Cask Storage System Canisters.* NRC Information Notice 2012-20, November 14, 2012. U.S. NRC, p.

NWTRB. (2010). *Evaluation of the Technical Basis for Extended Dry Storage and Transportation of Used Nuclear Fuel.* NWTRB, 145 p.

Rogers, N. J., Carson, K. C., Glenn, A. R., Dilworth, M. J., Hughes, M. N. and Poole, R. K. (2001). Alleviation of aluminum toxicity to Rhizobium leguminosarum bv. viciae by the hydroxamate siderophore vicibactin. *Biometals* **14**, 59-66.

Roy, N. and Chakrabartty, P. K. (2000). Effect of aluminum on the production of siderophore by Rhizobium sp.(Cicer arietinum). *Current microbiology* **41**, 5-10.

Ryhl-Svendsen, M. and Glastrup, J. (2002). Acetic acid and formic acid concentrations in the museum environment measured by SPME-GC/MS. *Atmospheric Environment* **36**, 3909-3916.

Salvarezza, R., De Mele, M. and Videla, H. (1983). Mechanisms of the microbial corrosion of aluminum alloys. *Corrosion* **39**, 26-32.

Sánchez, C. (2009). Lignocellulosic residues: biodegradation and bioconversion by fungi. *Biotechnology advances* **27**, 185-194.

Seinfeld, J. H. (1986). *Atmospheric Chemistry and Physics of Air Pollution*. New York, NY: John Wiley & Sons.

SNL. (2008). *Analysis of dust deliquescence for FEP screening.* Sandia National Laboratories, p.

Vega, F. E. and Blackwell, M. (2005). *Insect-fungal associations: ecology and evolution*: Oxford University Press.

WWPI. (2011). *Guide to Pressure Treated Wood.* Western Wood Preservers Institute, 13 p.

Zhang, X. and McMurry, P. H. (1992). Evaporative losses of fine particulate nitrates during sampling. *Atmospheric Environment* **26A**, 3305-3312.